# High Deviatoric Strain Engineering

by

Wenbin Li

Submitted to the Department of Materials Science and Engineering
in partial fulfillment of the requirements for the degree of

Doctor of Philosophy in Materials Science and Engineering

at the

MASSACHUSETTS INSTITUTE OF TECHNOLOGY

June 2015

Signature redacted

Author ..........................................................
Department of Materials Science and Engineering
April 29, 2015

Signature redacted

Certified by ..........................................................
Ju Li
Battelle Energy Alliance Professor of Nuclear Science and
Engineering, and Professor of Materials Science and Engineering
Thesis Supervisor

Signature redacted

Accepted by ..........................................................
Donald R. Sadoway
Chair, Departmental Committee on Graduate Students

# High Deviatoric Strain Engineering

by

Wenbin Li

Submitted to the Department of Materials Science and Engineering
on April 29, 2015, in partial fulfillment of the
requirements for the degree of
Doctor of Philosophy in Materials Science and Engineering

## Abstract

The structure of a material can be tuned reversibly or irreversibly by imposing elastic or inelastic strain, leading to change of properties. This defines the concept of strain engineering, which includes both elastic strain engineering (ESE) and inelastic strain engineering (ISE). In this thesis, we study ESE and ISE by deviatoric (non-hydrostatic) strain.

For ESE, we model how imposition of slowly-varying inhomogeneous elastic strain can induce the electronic structure changes of semiconductor crystals. The strain-dependent shift of valence and conduction band energy levels leads to the formation of electronic and hole bound states in inhomogeneously strained crystals, whose energy levels can be dynamically tuned by the strain field. We developed a new envelope function method with strain-parametrized basis set that can solve the electronic structure of such inhomogeneously strained crystals by incorporating the local electronic structure information obtained from unit-cell level first-principles calculation of homogeneously strained crystals.

For ISE, we study the deviatoric strain induced phase transformation and internal structure evolution in soft matter systems. Using largescale molecular dynamics simulation, we demonstrate that controlled sintering of the nanocrystals in self-assembled superlattices of alkanethiol-passivated gold nanoparticles can happen at room temperature through deviatoric stress-induced displacement of the organic ligands. We find that combining a hydrostatic pressure of order several hundred megapascal and a critical deviatoric stress along the nearest-neighbor direction of gold nanoparticle superlattices leads to ordered sintering of gold nanocrystals and the formation of gold nanowire arrays. Similar phenomena can happen in binary superlattices of gold and silver nanoparticles, and we predict the formation of gold-silver multijunction nanowire arrays through deviatoric-stress driven sintering of nanoparticles. We also simulate the plastic flow of two dimensional amorphous granular pillars subjected to athermal, uniaxial and quasistatic deformation. We find that for the athermal granular pillars under inhomogeneous load, the cumulative local deviatoric strains of particles with respect to their neighbors play the role of time in thermal systems, and drive the crossover of non-affine particle displacements from ballistic motion to diffusion. The result suggests that in disordered solids, deviatoric strain alone can drive particle diffusion even at zero vibrational temperature.

Thesis Supervisor: Ju Li
Title: Battelle Energy Alliance Professor of Nuclear Science and Engineering, and Professor of Materials Science and Engineering

# Acknowledgments

I would like to thank Professor Jeffrey Grossman and Professor Michael Rubner for serving on my thesis committee. Both of them are renowned scientists and educators, and their passion to help students can be genuinely felt throughout the thesis committee meetings we have together. I feel very fortunate to have them on my thesis committee and sincerely thank them for their critical inputs and suggestions.

I would like to express my deepest gratitude to Professor Ju Li, my advisor of nearly seven years. The more I get to know him, the more I am awed by his unfathomable intellectual breadth, depth and creativity. It is remarkable to me that such a brilliant scientist can be such a kind and humble person as well. Ju treats his students extremely well, provides them with ample freedom to explore their own interests while always available for inspiration and help. I feel extremely privileged to have worked with Ju. Without Ju's guidance, encouragements and insights, this thesis would never have come into being.

Thanks are due to my collaborators, Dr. Hongyou Fan, who contributed to the work presented in Chapter 4 of the thesis, and Jennifer Rieser, Professor Douglas Durian and Professor Andrea Liu, who made significant contribution to the work presented in Chapter 5. Jennifer in particular kindly shared many of her data analysis codes with me, and was always available for help whenever I have questions about her experiments. I also want to thank Professor Durian for his meticulous guidance and unwavering standards, and Professor Liu for her penetrating insights, which were critical to the success of the collaboration work.

Many thanks to the current and former members of the Li group for their guidance, help, and friendship. In particularly, I thank Liang and Xiaofeng for their exemplary roles in our group, and for teaching me many nuts and bolts of simulation. Wei, Ji and Erik also helped me a lot when I started my research career. Scores of other members of the Li group, including but not limited to Kejie, Mingda, Sina, Yang, Sangtae, Ziqiang, Soon Ju and Cong, helped me in many different ways and significantly contributed to my graduate education and experience. I could not ask

better colleagues and companions than these extraordinary individuals.

I also want to extend my gratitude to two extraordinary staff members, Vicky Lee at UPenn and Rachel Batista at MIT for being so nice and helpful, and for creating warm, welcoming working environment for everyone.

To my classmates and friends at Penn and MIT, my heartfelt thanks to you for making my life in the U.S. more colorful and enjoyable. Special thanks to Aaron, Jie and Lingyan. I always pleasantly recall our time together at Penn. The many late nights we studied together in the first semester of graduate school at Van Pelt, Sansom and LRSM have become unforgettable memory. More than six years ago, I promised to you that your name will appear in the Acknowledgment of my thesis. I am delivering that promise now.

Last, but most important, I thank my parents and my sister for their unconditional love. They are always there to support me.

# Contents

# List of Figures

# List of Tables

# Chapter 1

# Introduction

## 1.1 Elastic Strain Engineering

A crystal lattice is not infinitely strong even if it is in a defect-free state at zero temperature: it cannot be elastically deformed beyond its ideal strain limit [1, 2, 3, 4, 5, 6, 7, 8, 9, 10] without losing homogeneity of the lattice or undergoing phase transformation. The ideal elastic strain $\boldsymbol{\varepsilon}_{\text{ideal}}$ is an intrinsic property of an ideal atomic structure that contains absolutely no defects, and can be calculated from first principles for a periodic perfect lattice under periodic boundary condition at $T = 0K$. Because strain in three-dimensions (3D) is a $3 \times 3$ symmetrical tensor with six independent components, $\boldsymbol{\varepsilon}_{\text{ideal}}$ is a five-dimensional bounding surface in a six-dimensional strain space. Corresponding to $\boldsymbol{\varepsilon}_{\text{ideal}}$ is the ideal stress (strength) $\boldsymbol{\sigma}_{\text{ideal}}$. For most crystalline materials, the ideal strength for tension and shear is approximately $> \frac{1}{10}$ of the elastic modulus [11]. Since for an elastically strained crystal, the deviation from linear elasticity is not significant even when stress is high, the ideal elastic tensile or shear strain is roughly of order 10% [11]. Most conventional materials, however, cannot sustain tensile or shear strain more than $0.2 - 0.3\%$ before inelastic relaxations such as plasticity or fracture set in. The large discrepancy between ideal and practical elastic strain is because there are usually preexisting defects in conventional materials, such as dislocations or cracks, which activate plastic flow or fracture of the material well below its ideal strain limit. For example [12], steels have a Young's modulus $E \sim 200$ GPa. Imposing 1% of elastic strain means the sample-wide stress in the steel would be around 2 GPa. From experience we know that this exceeds the practical yield strength of most steels, which is usually on the order of a few hundred MPa. Assuming the measured yield strength of a steel is 600 MPa, the preexisting dislocations in the steel would start to move around and multiply around 0.3% of elastic strain, and the elastic strain cannot increase further. For a brittle material such as a bulk ingot of silicon or a silicon wafer ($E \sim 150$ GPa), a preexisting crack would probably start to grow at tensile strain around 0.1%, leading to the fracture of the material.

In recent years, however, a new class of ultra-strength materials [11], defined as being able to sustain sample-wide shear or tensile elastic strain exceeding 1% over a extended period of time at finite temperature, has emerged. At 1% elastic strain, the sample-wide stress in a material reaches a significant fraction ($\sim 10\%$) of their ideal strength. Most ultra-strength materials discovered so far are nanostructured, with one or more characteristic dimensions in the nano-size regime, such as nanoparticles, nanowires, thin films, atomic sheets and bulk nanocomposites. The reason that ultra-strength can be achieved in nanostructured materials is because the population dynamics of dislocation/crack nucleation, propagation and multiplication/annihilation are fundamentally altered in size-confined low dimensional materials [11], driving the "smaller is stronger" trend. The experimentally measured biaxial tensile elastic strain limit of graphene, a representative ultra-strength material, can be as high as 20% [13]. A monolayer of $MoS_2$ can be stretched to 11% of elastic strain experimentally [14]. Nowadays, large elastic strain can be imposed on ultra-strength materials by direct dynamic loading [13, 12], epitaxy [15], phase transformation [16], or thermomechanical processing [16].

The significantly enlarged elastic strain space in ultra-strength materials leads to new possibilities for tuning the physical and chemical properties of materials, by varying the six-dimensional elastic strain $\boldsymbol{\varepsilon}_e$ as continuous variables. This idea of elastic strain engineering (ESE) [12] has existed in various communities for many years and is rather straightforward, because a material's physical and chemical properties are functions of the lattice parameters of the underlying crystal lattice, or the elastic strain $\boldsymbol{\varepsilon}_{\mathrm{e}}$ with respect to the stress-free reference state [11]. Fundamentally, this is because the electronic structure of materials changes with elastic strain [17]. Hence, almost all functional properties of a material can be tuned by elastic strain, for examples electronic [18, 19, 20, 21, 22, 23, 24, 25], magnetic [26, 27, 28, 29], optical [23, 30, 31, 15], thermoelectric [32] and catalytic [33] properties. It is, however, only after human control of materials reaches nanoscale, which gives rise to ultra-strength materials, that the elastic strain space accessible to ESE becomes significantly larger.

The concept of ESE is very powerful because the individual components of the elastic strain tensor $\boldsymbol{\varepsilon}_{\mathrm{e}}$ are continuous variables. Like traditional chemical alloying, where the chemical composition $\mathbf{X} \equiv [X_1, ..., X_n]$ is the continuously tunable variable, in ESE the independent components of the elastic strain tensor $\boldsymbol{\varepsilon}_{\mathrm{e}}$ can be continuously tuned to optimize material properties. Generally speaking, take any physical or chemical property $A$ that one wants to optimize, for example the bandgap of a semiconductor, the gradient $\mathbf{g} = \partial A / \partial \boldsymbol{\varepsilon}_{\mathrm{e}}|_{a_0}$ is non-zero at the equilibrium lattice constant $a_0$ (unless $A$ is the bulk Helmholtz free energy which is by definition minimized at $a_0$) [11, 12]. This means that we can achieve desired changes in $A$ by altering the elastic strain tensor $\boldsymbol{\varepsilon}_{\mathrm{e}}$ along $\pm\mathbf{g}$. Namely, if we want to increase $A$, we can tweak $\boldsymbol{\varepsilon}_{\mathrm{e}}$ along $+\mathbf{g}$. Conversely, if we want to decrease $A$, we can take $\boldsymbol{\varepsilon}_{\mathrm{e}}$ along the direction of $-\mathbf{g}$. This optimization process in strain space can be carried out until we hit the elastic strain limit. Hence, by controlling the elastic strain, we add six continuous new dimensions (six independent components of strain tensor in three-dimensions) that can be tuned to optimize the properties we want. By ESE, we may not only change the values of properties, but also push chemical and physical behavior toward singularities [12] by inducing electronic phase transition, such as electronic band inversion that results in the transition of a normal insulator to a topological insulator [34]. Furthermore, in ultra-strength materials, inhomogeneous elastic strain field $\boldsymbol{\varepsilon}_{\mathrm{e}}(\mathbf{x})$ with large local elastic strain difference can be imposed, where $\mathbf{x}$ is a position vector in the material. Position-dependent properties can therefore be created in a material. This also introduces additional degrees of freedom – strain gradient $\boldsymbol{\nabla}\boldsymbol{\varepsilon}_{\mathrm{e}}(\mathbf{x})$, that can also be tuned to optimize local physical properties. This is because in an inhomogeneously strained crystal, the local properties $A(\mathbf{x})$ would not only depend on the local strain $\boldsymbol{\varepsilon}_{\mathrm{e}}(\mathbf{x})$, but also on the local strain gradient $\boldsymbol{\nabla}\boldsymbol{\varepsilon}_{\mathrm{e}}(\mathbf{x})$, as well as possible non-local, long-range effects due to the applied strain field.

## 1.2 Inelastic Strain Engineering

When a material is deformed beyond its elastic limit, most of the additional applied strain will be carried by inelastic strain $\boldsymbol{\varepsilon}_{\mathrm{i}}$. The total strain $\boldsymbol{\varepsilon}(\mathbf{x})$ at a given point $\mathbf{x}$ in the material can be decomposed into the sum of elastic strain and inelastic strain: $\boldsymbol{\varepsilon}(\mathbf{x}) \equiv \boldsymbol{\varepsilon}_{\mathrm{e}}(\mathbf{x}) + \boldsymbol{\varepsilon}_{\mathrm{i}}(\mathbf{x})$ [11, 12]. The elastic strain $\boldsymbol{\varepsilon}_{\mathrm{e}}(\mathbf{x})$ describes reversible distortion of the Bravais lattice vectors of "good crystals" away from defect cores, while the inelastic strain $\boldsymbol{\varepsilon}_{\mathrm{i}}(\mathbf{x})$ corresponds to irreversible bonding topology or phase transformation changes. The local elastic strain can be directly measured by selected-area electron or x-ray diffractions, but the local inelastic strain will be harder to quantify experimentally. To a good approximation, the local stress $\boldsymbol{\sigma}(\mathbf{x})$ is a function of only the local elastic strain, namely, $\boldsymbol{\sigma}(\mathbf{x}) \approx \boldsymbol{\sigma}(\boldsymbol{\varepsilon}_{\mathrm{e}}(\mathbf{x}))$.

In ESE, one aims to achieve the desired change of property $A(\mathbf{x})$ by imposing an unconventionally large amplitude of elastic strain $\boldsymbol{\varepsilon}_{\mathrm{e}}(\mathbf{x})$. One can however also engineer the inelastic strain $\boldsymbol{\varepsilon}_{\mathrm{i}}(\mathbf{x})$ to control properties, for example, by controlling the the spatial patterns of defects such as dislocations, grain boundaries and and deformation twins, or by inducing phase transformations. The control of microstructure and properties of materials by generating appropriate $\boldsymbol{\varepsilon}_{\mathrm{i}}(\mathbf{x})$ is the domain of inelastic strain engineering (ISE). Compared to ESE, ISE is more concerned with engineering the microstructure of materials at the lengthscale larger than unit cell. In certain circumstances such as phase transformation, ESE and ISE can be used in conjunction to achieve optimum results, and the entire approach is called strain engineering (SE) [12].

## 1.3 Overview of the Thesis

This thesis is a study on the engineering of the microstructure and properties of materials by high deviatoric strain, using the approaches of both ESE and ISE. By high deviatoric strain, we mean the magnitude of the non-hydrostatic components of the imposed strain tensor reaches or surpasses a significant fraction ($\sim$10%) of the ideal elastic strain limit. ESE with large-deviatoric strain is a relatively unexplored field, because, as we have mentioned earlier, materials that can sustain large deviatoric elastic strain become widely available only after the emergence of ultra-strength materials. In this sense, ESE with large deviatoric strain is to be distinguished from the traditional high-pressure physics, which is concerned with the behavior of materials under large isotropic compressive stress. The focus of this thesis on ESE is on how inhomogeneous strain changes the electronic structure of semiconductor crystals. For ISE, our study mainly focuses on the structural transformation of soft matter [35, 36] under large deviatoric strain. Soft matter are defined by the relatively weak interaction between their constituent molecules (units). Typical soft matter include polymers, colloids, granular materials and some biological materials. Due to the relatively weak interaction between the constituents (interaction energy comparable to thermal energy $k_{\mathrm{B}}T$), the structure of soft matter is sensitive to external stimuli, and entropy usually plays an important role in determining the equilibrium phase behavior and non-equilibrium dynamics of soft matter. Once driven out of equilibrium, the timescale of structural relaxation in soft materials can be significantly larger than hard materials (e.g. metals, ceramics, etc), which usually results in viscoelastic mechanical response. The interplay between enthalpy and entropy in soft materials can lead to very rich phase behavior, and many ordered structures can form through the process of self-assembly. We will study in this thesis an example of such self-assembled structure – supercrystals of ligand-passivated metal nanoparticles, and investigate their deviatoric stress (strain) induced mesoscale phase transformation.

The organization of this thesis is as follows. In Chapter 2, we review the fundamental concepts relevant to the studies presented in this thesis, in particular strain, stress and their determination in atomistic simulations. We also review the basic principles of molecular dynamics simulation, which is a key technique used to carry out our research on ISE.

Chapter 3 of the thesis focuses on ESE. In this chapter, we show that, due to the strain-induced shift of valence band and conduction band energy levels in semiconductor crystals, imposition of appropriate slowly-varying inhomogeneous strain can generate semiclassical confining potentials in a pristine semiconductor crystal, much like a continuous version of the confining potential in a semiconductor quantum well. The confining potential in inhomogeneously strained crystal leads to the creation of electron or hole bound states, whose discrete energy levels can be dynamically tuned by the imposed elastic strain field. We develop in Chapter 3 a new envelope function method that has the potential to efficiently solve the electronic structure of such inhomogeneously strained semiconductor crystals.

Chapter 4 and Chapter 5 focus on ISE. In Chapter 4, we study the deviatoric stress-driven sintering and phase transformation of self-assembled superlattices (supercrystals) of alkanethiol-passivated metal nanoparticles. Using largescale molecular dynamics simulation, we show that, due to the important role of soft organic ligands in the mechanical response, superlattices of ligand-passivated gold nanoparticles exhibit entropic viscoelasticity during compressive deformation at ambient pressure. If we apply a hydrostatic pressure of several hundred megapascals on the superlattice, combined with a critical deviatoric stress along the nearest-neighbor direction of the face-centered-cubic supercrystal, the deviatoric stress can lead to the diffusion and selective displacement of ligands on the surface of gold nanocrystals, resulting in the controlled sintering of the gold nanocrystals along the direction of deviatoric stress and the formation of ordered gold nanowire arrays. We also mapped out a non-equilibrium stress-driven processing diagram for the deviatoric-stress driven sintering of gold nanoparticle superlattices, which reveals that such deviatoric stress-driven sintering of nanoparticle superlattices into ordered nanowire arrays can occur in a region in the stress space. Insights into the phenomenon allow us to demonstrate that, for silver-gold (Ag-Au) binary nanoparticle superlattices in sodium chloride-type superstructure, stress-driven sintering along the nearest-neighbor direction leads to the formation of ordered Ag-Au multijunction nanowire arrays.

In Chapter 5, we carry out combined experiment and simulation to demonstrate that deviatoric stress can drive the diffusive motion of particles in disordered solids even at zero temperature. Using two-dimensional amorphous granular pillars as a model system, we study the internal structure evolution of the granular pillars under uniaxial and quasistatic deformation. Because the granular pillars are consisted of macroscopic discrete particles, thermal motion plays a negligible role in the dynamics of the system, meaning that the system is effectively at zero vibrational temperature. This allows us to rigorously study the effects of strain on particle dynamics by excluding the influence of thermal motion. By computing the local best-fit affine transformation strain and non-affine displacement associated with each particle in the granular pillars between two stages of deformation, we demonstrate that the non-affine particle displacements exhibit exponential crossover from ballistic motion to diffusion with respect to the cumulative local deviatoric strain. This indicates that in the athermal granular packings, the cumulative local deviatoric strain plays the role of time in thermal systems and drives effective particle diffusion. The result could have important implications for internal structural evolution of amorphous solids under mechanical deformation.

At the time this thesis was written, the results presented in Chapter 3 and Chapter 4 have been published [37, 38], and the results described in Chapter 5 have been submitted for publication.

# Chapter 2

# Fundamental Concepts and Simulation Methods

## 2.1 Strain and Stress

### 2.1.1 Lagrangian Strain Tensor

Under the action of external forces, solids usually exhibit deformation by changing its shape and/or volume. Treating a solid as a continuous media, its deformation can be described mathematically using the concept of displacement field and strain [39]. Denote by $\mathbf{x}$ the position vector of a material element in the solid in certain coordinate system, after deformation the position of the material element becomes $\mathbf{x}'$. A displacement vector $\mathbf{u}$ connects the material element before and after deformation, $\mathbf{u} = \mathbf{x}' - \mathbf{x}$. In Cartesian coordinates, the displacement vector has several components, each will denoted by $u_i$, $u_j$, etc. The displacement gradients can then be defined as

$$u_{ij} = \partial u_i / \partial x_j. \tag{2.1}$$

Deformation changes the distance between the points in the solids. For two points $\mathbf{x}$ and $\mathbf{x} + d\mathbf{x}$ very close together in the undeformed body, their original distance squared is $dl^2 = \sum_i (dx_i)^2$. It can be shown [39] that after deformation, the squared distance between the two points becomes

$$dl'^2 = dl^2 + (u_{ij} + u_{ji} + u_{ki}u_{kj})dx_i dx_j, \tag{2.2}$$

where Einstein summation applies for repeated indexes. The Lagrangian strain tensor $\eta_{ij}$ is defined by

$$\eta_{ij} = \frac{1}{2}(u_{ij} + u_{ji} + u_{ki}u_{kj}). \tag{2.3}$$

$dl'^2$ is then related to $dl^2$ as

$$dl'^2 = dl^2 + 2\eta_{ij}dx_i dx_j. \tag{2.4}$$

Hence, the distances between material elements in the deformed body is completely specified if their original distances and the Lagrangian strain tensor $\eta_{ij}$ is determined for every point in the undeformed body. Because the free energy of a solid is determined by the distances between the material elements inside, Lagrangian strain plays an important role in the theory of strained solids.

By definition, Lagrangian strain tensor is symmetric, namely $\eta_{ij} = \eta_{ji}$. For small deformation, the higher order terms in Lagrangian strain can be neglected, giving

$$\eta_{ij} = \frac{1}{2}(u_{ij} + u_{ji}). \tag{2.5}$$

If a solid is deformed homogeneously, the deformation gradients $u_{ij}$ are constant throughout the solid. Removing rigid translation, a material element at position $\mathbf{x}'$ in the deformed body is related to the corresponding position in the undeformed solid $\mathbf{x}$ via the following relationship

$$x'_i = (u_{ij} + \delta_{ij})x_j, \tag{2.6}$$

where $\delta_{ij}$ is the Kronecker delta. Hence, we can define an affine transformation matrix $J_{ij} = u_{ij} + \delta_{ij}$ that relates the coordinates of homogeneously deformed and undeformed solids as

$$x'_i = J_{ij} x_j. \tag{2.7}$$

It is straightforward to show that $J$ is related to the Lagrangian strain matrix defined in Eq. 2.3 as

$$\eta_{ij} = \frac{1}{2}(J_{ki} J_{kj} - \delta_{ij}). \tag{2.8}$$

In the language of matrix operation, this is equivalent to

$$\eta = \frac{1}{2}\left(J^{\mathrm{T}} J - I\right), \tag{2.9}$$

where $I$ is an identity matrix whose dimensions are same as $J$. Therefore, for a homogeneously deformed solid, the Lagrangian strain $\eta$, which is uniform throughout the solid, can be calculated from the affine transformation matrix $J$ using Eq. 2.9.

The transformation matrix $J$ is not necessarily symmetric as it may include the effect of rigid rotation. The Polar Decomposition Theorem [40] of mathematics states that a non-singular square matrix can be uniquely expressed as the left or right product of a symmetric matrix matrix and a rotational matrix,

$$J = RM = ML, \tag{2.10}$$

where $M$ is a symmetric matrix satisfying $M^{\mathrm{T}} = M$. $R$ and $L$ are rotational matrices, with the property $R^{\mathrm{T}} R = L^{\mathrm{T}} L = 1$. Therefore,

$$\eta = \frac{1}{2}\left(J^{\mathrm{T}} J - I\right) = \frac{1}{2}\left(M^2 - I\right) \tag{2.11}$$

The symmetric transformation matrix $M$ has one-to-one correspondence with $\eta$ via

$$M = \sqrt{1 + 2\eta} = 1 + \eta - \frac{1}{2}\eta^2 + \ldots \tag{2.12}$$

### 2.1.2 External and Thermodynamic Stress Tensor

Like strain, stress is also a tensor. There are two definitions of stress. The first definition is the external stress $\sigma_{ij}$, which relates the traction force on a surface in the deformed solid with the surface normal unit vector,

$$dT_i = \sigma_{ij} n_j dS, \tag{2.13}$$

where $dT_i$ are the components of the external traction force, $n_j$ are the components of the outward surface normal unit vector and $dS$ is the surface area. The tensorial nature of stress reflects the fact that in general, the traction force on a surface is not parallel to the surface normal. To prevent rotation, stress tensor must be symmetric, namely, $\sigma_{ij} = \sigma_{ij}$.

In three-dimensional Cartesian coordinates, stress tensor can be represented as a $3 \times 3$ matrix,

$$\sigma = \begin{bmatrix} \sigma_{xx} & \sigma_{xy} & \sigma_{xz} \\ \sigma_{xy} & \sigma_{yy} & \sigma_{yz} \\ \sigma_{xz} & \sigma_{yz} & \sigma_{zz} \end{bmatrix}. \tag{2.14}$$

$\sigma$ can be decomposed into hydrostatic and deviatoric stress components,

$$\sigma = \sigma_{\mathrm{hyd}} I + \sigma_{\mathrm{dev}}, \tag{2.15}$$

where the hydrostatic stress invariant $\sigma_{\mathrm{hyd}} = \frac{1}{3}(\sigma_{xx} + \sigma_{yy} + \sigma_{zz}) = \frac{1}{3}\mathrm{Tr}(\sigma)$.

A scalar quantity frequently used in engineering to measure the magnitude of deviatoric stress is the von Mises deviatoric stress $\sigma_{\mathrm{vM}}$, which is defined as

$$\begin{aligned} \sigma_{\mathrm{vM}} &= \sqrt{\frac{3}{2}\mathrm{Tr}(\sigma_{\mathrm{dev}} \cdot \sigma_{\mathrm{dev}})} \\ &= \left[\frac{1}{2}(\sigma_{xx} - \sigma_{yy})^2 + \frac{1}{2}(\sigma_{yy} - \sigma_{zz})^2 + \frac{1}{2}(\sigma_{zz} - \sigma_{xx})^2 + 3\sigma_{xy}^2 + 3\sigma_{yz}^2 + 3\sigma_{xz}^2\right]^{\frac{1}{2}} \end{aligned} \tag{2.16}$$

The second definition of stress is the internal (thermodynamic) stress $t_{ij}$, which relates the free energy change of a system to strain tensor. Equilibrium condition requires that internal stress is equal to the external stress, namely $t_{ij} = \sigma_{ij}$. It can be proved that [41], for a homogeneously deformed solid, the differential work done by external stress $\sigma_{ij}$ on the system is

$$dW = V\sigma_{ij} d\eta_{ij}, \tag{2.17}$$

where $V$ is the volume of the system. It is important to emphasize that the reference configuration for the calculation of Lagrangian strain tensor in the above equation is the *current* configuration, for which the system can either be deformed already or still in undeformed state. Consider the deformation process is quasistatic, the external stress $\sigma_{ij}$ in the above equation can replaced by internal stress $t_{ij}$ and written as $dW = Vt_{ij}d\eta_{ij}$. The combined first and second law of thermodynamics for a deformed solid can then be written down as

$$dU = TdS + Vt_{ij}d\eta_{ij}. \tag{2.18}$$

The full differential of the Helmholtz free energy, $F = U - TS$, can be written as

$$dF = -SdT + Vt_{ij}d\eta_{ij}. \tag{2.19}$$

Therefore, $t_{ij}$ are related to thermodynamic potentials $U$ and $F$ through

$$t_{ij} = \frac{1}{V} \left. \frac{\partial U}{\partial \eta_{ij}} \right|_S, \tag{2.20}$$

$$t_{ij} = \frac{1}{V} \left. \frac{\partial F}{\partial \eta_{ij}} \right|_T. \tag{2.21}$$

In Eq. 2.20, the entropy $S$ of the system is fixed, which is suitable for the case of adiabatic deformation. Eq. 2.21 is suitable for isothermal deformation. The two equations shall be regarded as the *definition* of thermodynamics stress.

## 2.2 Strain and Stress in Atomistic Simulation

### 2.2.1 Strain from Simulation Supercell Variation

In atomistic simulations, the system is usually enclosed within a parallelepiped-shape supercell, with periodic boundary conditions imposed. The shape of the supercell is determined by three independent supercell vectors $\mathbf{a}_0$, $\mathbf{b}_0$ and $\mathbf{c}_0$. If the shape of the supercell is allowed to change, a strain tensor can be defined between an initial and a final configuration. Let the supercell basis vectors after deformation be $\mathbf{a}$, $\mathbf{b}$ and $\mathbf{c}$ respectively. We can define an affine transformation matrix $\mathbf{J}$ that maps $(\mathbf{a}_0, \mathbf{b}_0, \mathbf{c}_0)$ to $(\mathbf{a}, \mathbf{b}, \mathbf{c})$, namely, $\mathbf{a} = \mathbf{J}\mathbf{a}_0$, $\mathbf{b} = \mathbf{J}\mathbf{b}_0$, and $\mathbf{c} = \mathbf{J}\mathbf{c}_0$. Here the basis vectors are considered to be column vectors, and they form two matrices $\mathbf{h}_0$ and $\mathbf{h}$ given by $\mathbf{h}_0 = (\mathbf{a}_0, \mathbf{b}_0, \mathbf{c}_0)$ and $\mathbf{h} = (\mathbf{a}, \mathbf{b}, \mathbf{c})$. The mapping relationship between the original and deformed supercell can be written as

$$\mathbf{h} = \mathbf{J}\mathbf{h}_0, \tag{2.22}$$

which gives $\mathbf{J} = \mathbf{h}\mathbf{h}_0^{-1}$. Based on Eq. 2.9, the Lagrangian strain matrix can be calculated as

$$\begin{aligned} \boldsymbol{\eta} &= \frac{1}{2}\left(\mathbf{J}^T\mathbf{J} - \mathbf{I}\right) \\ &= \frac{1}{2}\left[(\mathbf{h}_0^{-1})^T\mathbf{h}^T\mathbf{h}(\mathbf{h}_0^{-1}) - \mathbf{I}\right]. \end{aligned} \tag{2.23}$$

Using index notation, $\eta_{ij} = \frac{1}{2}\left[(h_0^{-1})^T_{im}h^T_{mn}h_{np}(h_0^{-1})_{pj} - \delta_{ij}\right]$.

### 2.2.2 Least Square Atomic Local Strain

Atomic local strain [42, 43, 44] is a useful measure of atomic-level deformation in a solid when the solid is deformed inhomogeneously, and especially if the reference configuration for strain calculation has no apparent symmetry, which is the case for disordered solids.

Since strain is always relative, to calculate the full strain tensor, one needs two atomistic configuration, the reference and the current configuration respectively. For atoms in the reference configuration, one defines a sampling radius $R_c$. If the distance of an atom to atom $i$ falls within $R_c$, it is considered to be a neighbor of the atom $i$. The total number of neighbors for atom $i$ is denoted by $N_i$. For each neighbor $j$ of atom $i$, the distance vector from $i$ to $j$ in the reference configuration is denoted as

$$\mathbf{d}_{ij}^0 \equiv \mathbf{r}_j^0 - \mathbf{r}_i^0 \tag{2.24}$$

After deformation, this distance vector becomes

$$\mathbf{d}_{ij} \equiv \mathbf{r}_j - \mathbf{r}_i \tag{2.25}$$

for the current configuration. Here the vectors $\mathbf{d}_{ij}^0$ and $\mathbf{d}_{ij}$ are considered to be column vectors. One seeks to find the best affine transformation matrix $\mathbf{J}_i$ that maps all the neighbor distance vectors centering on $i$ in the reference configuration, namely $\mathbf{d}_{ij}^0$, to the distance vectors $\mathbf{d}_{ij}$ after deformation. The error of mapping from $\mathbf{d}_{ij}^0$ to $\mathbf{d}_{ij}$, denoted by $\mathbf{s}_{ij}$, is defined as following:

$$\mathbf{d}_{ij} = \mathbf{J}_i \mathbf{d}_{ij}^0 + \mathbf{s}_{ij}. \tag{2.26}$$

One seeks to find the best affine transformation matrix $\mathbf{J}_i$ that minimizes the sum of mapping errors for all the distance vectors $\mathbf{d}_{ij}^0$, which is denoted by $D_i^2$,

$$D_i^2 = \sum_{j \in N_i} \left|\mathbf{s}_{ij}\right|^2 = \sum_{j \in N_i} \left|\mathbf{d}_{ij} - \mathbf{J}_i \mathbf{d}_{ij}^0\right|^2. \tag{2.27}$$

The expression of $D_i^2$ can be further written as

$$\begin{aligned}D_i^2 &= \sum_{j\in N_i}(\mathbf{d}_{ij} - \mathbf{J}_i\mathbf{d}_{ij}^0)^T(\mathbf{d}_{ij} - \mathbf{J}_i\mathbf{d}_{ij}^0) \\ &= \sum_{j\in N_i}\mathrm{Tr}\,(\mathbf{d}_{ij} - \mathbf{J}_i\mathbf{d}_{ij}^0)(\mathbf{d}_{ij} - \mathbf{J}_i\mathbf{d}_{ij}^0)^T \\ &= \mathrm{Tr}\sum_{j\in N_i}(\mathbf{d}_{ij} - \mathbf{J}_i\mathbf{d}_{ij}^0)(\mathbf{d}_{ij}^T - \mathbf{d}_{ij}^{0T}\mathbf{J}_i^T). \qquad (2.28)\end{aligned}$$

Infinitesimal variation of $\mathbf{J}_i$ leads to change of $D_i^2$ given by

$$\begin{aligned}&D_i^2(\mathbf{J}_i + \delta\mathbf{J}_i) - D_i^2(\mathbf{J}_i) \\ =&\mathrm{Tr}\left[\delta\mathbf{J}_i\sum_{j\in N_i}(\mathbf{d}_{ij}^0\mathbf{d}_{ij}^{0T}\mathbf{J}_i^T - \mathbf{d}_{ij}^0\mathbf{d}_{ij}^T)\right] + \mathrm{Tr}\left[\sum_{j\in N_i}(\mathbf{J}_i\mathbf{d}_{ij}^0\mathbf{d}_{ij}^{0T} - \mathbf{d}_{ij}\mathbf{d}_{ij}^{0T})(\delta\mathbf{J}_i)^T\right] + \mathcal{O}((\delta\mathbf{J}_i)^2).\end{aligned} \qquad (2.29)$$

Let

$$\begin{aligned}A &= \delta\mathbf{J}_i\sum_{j\in N_i}(\mathbf{d}_{ij}^0\mathbf{d}_{ij}^{0T}\mathbf{J}_i^T - \mathbf{d}_{ij}^0\mathbf{d}_{ij}^T), \qquad (2.30)\\ A^T &= \sum_{j\in N_i}(\mathbf{J}_i\mathbf{d}_{ij}^0\mathbf{d}_{ij}^{0T} - \mathbf{d}_{ij}\mathbf{d}_{ij}^{0T})(\delta\mathbf{J}_i)^T. \qquad (2.31)\end{aligned}$$

since $\mathrm{Tr}(A) = \mathrm{Tr}(A^T)$, we have

$$D_i^2(\mathbf{J}_i + \delta\mathbf{J}_i) - D_i^2(\mathbf{J}_i) = 2\mathrm{Tr}\ \delta\mathbf{J}_i\sum_{j\in N_i}(\mathbf{d}_{ij}^0\mathbf{d}_{ij}^{0T}\mathbf{J}_i^T - \mathbf{d}_{ij}^0\mathbf{d}_{ij}^T) + \mathcal{O}((\delta\mathbf{J}_i)^2). \qquad (2.32)$$

For the $\mathbf{J}_i$ that minimize $D_i^2$, the first order term in $\delta\mathbf{J}_i$ must vanish, namely,

$$\mathrm{Tr}\ \delta\mathbf{J}_i\sum_{j\in N_i}(\mathbf{d}_{ij}^0\mathbf{d}_{ij}^{0T}\mathbf{J}_i^T - \mathbf{d}_{ij}^0\mathbf{d}_{ij}^T) = 0. \qquad (2.33)$$

In order for the above to be true for any $\delta\mathbf{J}_i$, the matrix $\sum_{j\in N_i}(\mathbf{d}_{ij}^0\mathbf{d}_{ij}^{0T}\mathbf{J}_i^T - \mathbf{d}_{ij}^0\mathbf{d}_{ij}^T)$

has to be zero, which leads to

$$\left(\sum_{j\in N_i} \mathbf{d}_{ij}^0 \mathbf{d}_{ij}^{0T}\right) \mathbf{J}_i^T = \sum_{j\in N_i} \mathbf{d}_{ij}^0 \mathbf{d}_{ij}^T. \tag{2.34}$$

Perform matrix transposition on the both sides of the above equation, we have

$$\mathbf{J}_i \sum_{j\in N_i} \mathbf{d}_{ij}^0 \mathbf{d}_{ij}^{0T} = \sum_{j\in N_i} \mathbf{d}_{ij} \mathbf{d}_{ij}^{0T}. \tag{2.35}$$

If we define

$$\mathbf{V}_i = \sum_{j\in N_i} \mathbf{d}_{ij}^0 \mathbf{d}_{ij}^{0T}, \quad \mathbf{W}_i = \sum_{j\in N_i} \mathbf{d}_{ij} \mathbf{d}_{ij}^{0T}, \tag{2.36}$$

then

$$\mathbf{J}_i = \mathbf{W}_i \mathbf{V}_i^{-1}. \tag{2.37}$$

The Lagrangian strain matrix can then be calculated from $\mathbf{J}_i$ as

$$\boldsymbol{\eta}_i = \frac{1}{2}(\mathbf{J}_i^T \mathbf{J}_i - \mathbf{I}). \tag{2.38}$$

Hydrostatic and shear invariants can be computed from the Lagrangian strain matrix. The hydrostatic invariant is defined as

$$\eta_i^m = \frac{1}{D} \mathrm{Tr} \boldsymbol{\eta}_i, \tag{2.39}$$

where $D$ is the dimension of the system. The local shear invariant is computed as

$$\eta_i^s = \sqrt{\frac{1}{2} \mathrm{Tr}(\boldsymbol{\eta}_i - \eta_i^m \mathbf{I})^2}, \tag{2.40}$$

which is calibrated to the case of pure shear, namely when $\eta_{xy} = \eta_{yx} = a$, and all other components of $\boldsymbol{\eta}$ is zero, $\eta_i^s = a$.

### 2.2.3 Microscopic Expression of Stress Tensor

We have discussed previously that for an isothermally and homogeneously deformed system, the thermodynamic stress $t_{ij}$ is related to the Helmholtz free energy of the system as

$$t_{ij} = \frac{1}{V} \frac{\partial F}{\partial \eta_{ij}}\bigg|_T , \tag{2.41}$$

where the reference for the calculation of infinitesimally small strain tensor $\eta$ is the current configuration and $V$ is the volume of current configuration. From statistical mechanics, $F = -k_{\mathrm{B}} T \ln Z$, where $Z$ is the canonical partition function of the system. We use $X$ and $Y$ to denote the current and deformed configurations of the system respectively. $X$ and $Y$ are related by the transformation matrix $J$, namely, $Y = JX$. The Lagrangian strain tensor is given by $\eta = \frac{1}{2}(J^{\mathrm{T}} J - 1)$. Since the Hamiltonian of the system is usually rotationally invariant, we can choose $J$ to be a symmetric matrix $M$ corresponding to $\eta$. The partition function of the deformed system, ignoring constants such as $N! h^{3N}$, can be expressed as

$$Z(X, \eta) = Z(X, M) = \int_Y d\tilde{q}^N d\tilde{p}^N \exp\left(-\beta \mathcal{H}(\tilde{q}^N, \tilde{p}^N)\right), \tag{2.42}$$

where we assume the Hamiltonian of the system $\mathcal{H}(\tilde{q}^N, \tilde{p}^N)$ has the following form

$$\mathcal{H}(\tilde{q}^N, \tilde{p}^N) = \sum_{n=1}^{N} \frac{\tilde{\mathbf{p}}_n^T \cdot \tilde{\mathbf{p}}_n}{2m_n} + \mathcal{U}(\tilde{\mathbf{q}}_1, \tilde{\mathbf{q}}_2, ..., \tilde{\mathbf{q}}_N). \tag{2.43}$$

The deformed coordinates $\tilde{q}_n$ can be related to the the undeformed coordinates $q_n$ as

$$\tilde{q}_n = M q_n. \tag{2.44}$$

The generalized momenta $p_n$ corresponding to $q_n$ are [45]

$$\tilde{p}_n = (M^T)^{-1} p_n = M^{-1} p_n \tag{2.45}$$

Eq. 2.44 and Eq. 2.45 define change of variable

$$\tilde{q}_n \equiv M q_n, \quad \tilde{p}_n \equiv M^{-1} p_n, \quad n = 1, 2, ..., N \tag{2.46}$$

The Jacobian of the transformation between $\{\tilde{q}_n, \tilde{p}_n\}$ and $\{q_n, p_n\}$ is one, which preserves the phase space volume. Applying the coordinate transformation, the Hamiltonian can be written as

$$\mathcal{H}(q^N, p^N) = \sum_{n=1}^{N} \frac{\mathbf{p}_n^T M^{-2} \mathbf{p}_n}{2m_n} + \mathcal{U}(M\mathbf{q}_1, M\mathbf{q}_2, ..., M\mathbf{q}_N). \tag{2.47}$$

From Eq. 2.12, we have

$$M = \sqrt{1 + 2\eta} = 1 + \eta - \frac{1}{2}\eta^2 + ... \tag{2.48}$$

Hence,

$$M^{-2} = \frac{1}{1 + 2\eta} = 1 - 2\eta + 4\eta^2 + ... \tag{2.49}$$

The Hamiltonian of the system can then be approximated as

$$\mathcal{H}(q^N, p^N) \approx \sum_{n=1}^{N} \frac{\mathbf{p}_n^T (1 - 2\eta + 4\eta^2) \mathbf{p}_n}{2m_n} + \mathcal{U}((1 + \eta - \frac{1}{2}\eta^2)\mathbf{q}_n) \tag{2.50}$$

The partition function can be written as

$$\begin{aligned} Z(X, \eta) &= \int_Y d\tilde{q}^N d\tilde{q}^N \exp\left[-\beta \mathcal{H}(\tilde{q}^N, \tilde{p}^N)\right] \\ &= \int_X dq^N dp^N \exp\left[-\beta \mathcal{H}(q^N, p^N)\right] \end{aligned} \tag{2.51}$$

The thermodynamic stress $t_{ij}$ can be calculated as

$$t_{ij} = \frac{1}{V(X)} \frac{\partial F}{\partial \eta_{ij}} = \frac{1}{V(X)} \cdot \frac{1}{-\beta Z} \frac{\partial Z}{\partial \eta_{ij}} = \frac{1}{V(X)} \cdot \frac{1}{Z} \int_X dq^N dp^N T_{ij} \exp\left[-\beta \mathcal{H}(q^N, p^N)\right], \tag{2.52}$$

where

$$T_{ij} = \frac{\partial \mathcal{H}(q^N, p^N)}{\partial \eta_{ij}}, \tag{2.53}$$

$V(X)$ is the volume of the system for the current configuration. The index notation for $\mathbf{p}_n^T \eta \mathbf{p}_n$ and $\mathbf{p}_n^T \eta^2 \mathbf{p}_n$ are given by

$$\mathbf{p}_n^T \eta \mathbf{p}_n = p_r^n \eta_{rk} p_k^n, \tag{2.54}$$

$$\mathbf{p}_n^T \eta^2 \mathbf{p}_n = p_r^n \eta_{rs} \eta_{sk} p_k^n, \tag{2.55}$$

where we use $p_r^n$ to denote the $r$ component of the vector $\mathbf{p}_n$. It is then straightforward to show that

$$\begin{aligned}\frac{\partial \mathcal{H}(q^N, p^N)}{\partial \eta_{ij}} = \sum_{n=1}^{N} & \frac{-p_i^n p_j^n + 2p_i^n \eta_{jk} p_k^n + 2p_k^n \eta_{ki} p_j^n}{m_n} + q_j^n \nabla_i^n \mathcal{U}((1 + \eta - \frac{1}{2}\eta^2) q^N) \\ & - \frac{1}{2}(\eta_{jk} q_k^n + \eta_{ki} q_j^n) \nabla_k^n \mathcal{U}((1 + \eta - \frac{1}{2}\eta^2) q^N).\end{aligned} \tag{2.56}$$

Because the above derivative is evaluated at $\eta = 0$, we have

$$T_{ij} = \sum_{n=1}^{N} \frac{-p_i^n p_j^n}{m_n} + q_j^n \nabla_i^n \mathcal{U}(q^N). \tag{2.57}$$

Since $f_i^n = -\nabla_i^n \mathcal{U}(q^N)$ is the $i$ component of the force acting on the atom $n$, we arrive at the following microscopic formula for the thermodynamic stress

$$t_{ij} = \left\langle -\frac{1}{V} \left( \sum_{n=1}^{N} \frac{p_i^n p_j^n}{m_n} + f_i^n q_j^n \right) \right\rangle \tag{2.58}$$

The notation $\langle\rangle$ means canonical ensemble average in the original configuration. While the above formula is derived for canonical ensemble, it can be applied to any ensemble in the thermodynamic limit, where all ensembles are equivalent for the average of intensive quantities [46, 44]. The symbol $\langle\rangle$ then takes the meaning of ensemble average in a particular ensemble.

## 2.3 Fundamentals of Molecular Dynamics Simulation

In this thesis, molecular dynamics (MD) simulation is one of the main methods employed to study the behavior of materials under stressed environment. In MD, the trajectories of a system of $N$ particles are generated by numerically integrating the classical Newtonian equations of motion, with appropriately specified interparticle interaction potentials, as well as suitable initial and boundary conditions. The system of particles can either interact with each other in a closed system, or evolve under a constant external driving force, which for example can be mechanical deformation or temperature gradient. Physical properties of the system can be determined from the microscopic information of the systems using the methods of equilibrium and non-equilibrium statistical mechanics. In some sense, MD simulations are computer experiments coupled with a "microscope" with atomic-level spatial resolution and femtosecond-level temporal resolution, as well as "force gauges" on every individual particles. Because of its capability to simulate the microscopic dynamic processes, MD has become an important tool in a wide range of fields such as materials science, physics, chemistry and biology. Nowadays, the number of particles in a typical classical MD simulation can be several hundreds up to several millions. With the rapid development of parallel computing technologies, the size of systems that can be studied by MD is ever-expanding, as the trajectories of particles on different regions of a system can be calculated in parallel on different processors. On the other hand, due to the small discretized time step necessary to numerically integrate the equations of motion of particles and the sequential nature of this process, the time span of system evolution that can be covered by a typical MD simulation is limited, usually well below a micro-second. The latter hampers the study of long-term processes and rare events that occurs on much larger timescale by normal MD simulation. The development of atomistic simulation methods that can overcome the timescale barrier of MD is an active field of research, and many different accelerated MD methods have been developed [47, 48, 49, 50, 51, 52].

### 2.3.1 Classical Equations of Motion

Consider a classical system of $N$ particles that evolve under the influence of the internal forces between them. Denote by $\mathbf{r}_1(t)$, $\mathbf{r}_2(t)$, ..., $\mathbf{r}_N(t)$ the spatial positions of the particles and $\mathbf{v}_1(t)$, $\mathbf{v}_2(t)$, ..., $\mathbf{v}_N(t)$ the velocities, the motion of the particles is determined by Newton's second law,

$$m_i \frac{d^2\mathbf{r}_i}{dt^2} = \mathbf{F}_i, \tag{2.59}$$

where $m_i$ is the mass of particle $i$ and $\mathbf{F}_i$ is the force on $i$. $\mathbf{F}_i$ is in principle a function of the positions of all particles, namely $\mathbf{F}_i = \mathbf{F}_i(\mathbf{r}_1, ..., \mathbf{r}_N)$. If the form of $\mathbf{F}_i(\mathbf{r}_1, ..., \mathbf{r}_N)$ is known, then the particles in the system will evolve deterministically according to the coupled second-order differential equation in Eq. 2.59. There are in total $dN$ independent equations, where $d$ is the number of spatial dimensions. In MD, $\mathbf{F}_i(\mathbf{r}_1, ..., \mathbf{r}_N)$ are usually calculated from the empirical potential energy function $U(\mathbf{r}_1, ..., \mathbf{r}_N)$ of the system based on the relationship $\mathbf{F}_i = -\boldsymbol{\nabla}_i U$. Clearly, the quality of potential energy function in representing the actual interaction between the particles has a major influence on the MD simulation results. Eq. 2.59 is solved numerically in MD via time discretization, and the time step is denoted by $\Delta t$. The maximum allowed value of $\Delta t$ is determined by the frequency of the fastest relevant physical processes in the system. For example, in solids, in order to resolve the vibrational motion of the atoms, $1/\Delta t$ needs to be larger than the highest phonon frequency of the solid, which is on the order of $10^{12} \sim 10^{13}$ Hz. $\Delta t$ is hence often chosen from 0.5 to a few femtoseconds, depending on the specific problem.

Note that when we describe the evolution of a system in terms of Newtonian equations of motion, we assume that, first, the motion of electrons and nuclei are decoupled. This so-called Born-Oppenheimer approximation assumes that, due to the orders of magnitude difference in the masses of electrons and ions, the motion of electrons is much faster than ions, such that when the ions move, the electrons are at instantaneous ground state. While this is usually a very good approximation, it breaks down for certain ultrafast dynamics involving coupled electron-ion motion.

Second, we ignore the quantum effects in dynamics. Below Debye temperature, the equipartition theorem of classical statistical mechanics, which states that every degree of freedom possess $k_{\mathrm{B}}T/2$ kinetic energy, breaks down. The occupation number of the phonons, the vibrational modes of the systems, cannot be described correctly by classical Boltzmann distribution. In additions, the intrinsic quantum fluctuations in the positions of the ions are not described, which is particularly an issue for light-mass elements such as hydrogen.

Many algorithms have been developed to numerically integrate the Newtonian equations of motion [45]. Some of the algorithms aim to generate the short or long term trajectories of the particles more accurately, while others emphasize the preservation of conserved quantities such as the total energy of the system. The most commonly used algorithm is the velocity Verlet integrator:

$$\mathbf{r}_i(t+\Delta t) = \mathbf{r}_i(t) + \mathbf{v}_i(t)\Delta t + \frac{\mathbf{F}_i(t)}{2m_i}\Delta t^2, \tag{2.60}$$

$$\mathbf{v}_i(t+\Delta t) = \mathbf{v}_i(t) + \frac{\mathbf{F}_i(t+\Delta t) + \mathbf{F}_i(t)}{2m_i}\Delta t. \tag{2.61}$$

The velocity Verlet algorithm has the feature that the velocities of the particles are computed only after the new positions and therefore the new forces of the particles are determined. The algorithm is fast and maintains good long-term energy conservation. The latter is closely related to the fact that velocity Verlet is a symplectic integrator [53], which preserves the phase space volume conservation property of Hamiltonian dynamics and therefore the energy conservation error is bounded [54].

It is important to realize that no matter what numerical integrator one uses, given a choice of initial condition, after certain amount of time that is typically much shorter than the duration of a MD simulation, the trajectories of the particles will bear little resemblance to the "true" trajectory rigorously given by Eq. 2.59. Fortunately, the numerical trajectories generated in MD are statistically equivalent to the true solution within bounded error [45]. This ensures the physical properties we calculate are on average the same as those obtained from the true trajectories. In this sense, we shall focus more on the statistical interpretation of the atomistic trajectories generated by

MD simulation.

In MD simulation, a system of particles are typically placed in a parallelpiped supercell specified by three edge vectors ($\mathbf{a}$, $\mathbf{b}$, $\mathbf{c}$), which determine the shape and volume of the supercell. As the number of particles in the supercell is finite, in order to simulate bulk properties one usually applies periodic boundary conditions. This means that the supercell is surrounded by identical image cells. The total number of such image cells are 26 in three dimensions. If a particle moves out from one side of the simulation box, it will appear in an image cell and hence mapped back to the supercell by entering from the opposite side of the simulation box. The total number of particles is therefore constant. If the equations of motion of the particles are those given by Eq. 2.59, the total energy of the system $E$ will be a constant of motion as well. The simulation is then said to sample the microcanonical or $(NVE)$ ensemble. The microcanonical ensemble is the most fundamental ensemble in MD. Many dynamic properties, such as velocity autocorrelation function which gives the diffusion coefficient of particles, are best calculated in the microcanonical ensemble. On the other hand, many real experiments are carried out under constant temperature, constant volume conditions, which corresponds to the canonical $(NVT)$ ensemble, or under constant temperature, constant pressure conditions, which correspond to isothermal-isobaric $(NPT)$ ensemble. In order to simulate systems under these conditions, extended MD methods capable of generating trajectories of particles corresponding to $NVT$, $NPT$ and other ensembles have been developed. We will describe in some details the algorithms behind these extended MD methods. Because these methods are typically formulated in the language of Lagrangian or Hamiltonian mechanics, in stead of Newtonian mechanics, below we shall first review the basic principles of Lagrangian or Hamiltonian mechanics.

The Lagrangian formulation of classical mechanics is based on the Hamilton's principle [55], which states that, for a classical system whose configuration described by a set of independent generalized coordinates $q_1, ..., q_n$, the motion of the system corresponds to a path in the multi-dimensional configuration space $\{q_1, ..., q_n\}$ for which the classical action $I$ is stationary. The action $I$ from time $t_1$ to $t_2$ is given by

$$I = \int_{t_1}^{t_2} \mathcal{L}(q_1, ..., q_n, \dot{q}_1, ..., \dot{q}_n, t)dt, \tag{2.62}$$

where the quantity $\mathcal{L}$ is called the Lagrangian, which is defined as the kinetic energy $K$ minus the potential energy $U$, namely,

$$\mathcal{L}(q_i, \dot{q}_i, t) = K(q_i, \dot{q}_i, t) - U(q_i, \dot{q}_i, t). \tag{2.63}$$

The Hamilton's principle says that the variation of action $I$ to small perturbation in the path $\{q_i, \dot{q}_i, t\}$ is zero:

$$\delta I = \int_{t_1}^{t_2} \mathcal{L}(q_i, \dot{q}_i, t)dt = 0. \tag{2.64}$$

This leads to the Lagrange equations of motion

$$\frac{d}{dt}\frac{\partial \mathcal{L}}{\partial \dot{q}_i} - \frac{\partial \mathcal{L}}{\partial q_i} = 0, \qquad i = 1, 2, ..., n. \tag{2.65}$$

There are $n$ independent equations above, $n$ being the total number of independent generalized coordinates. The Lagrange equations of motion are second order in nature. To completely determine the motion of the system one needs to specify $2n$ initial values, which for example can be $n$ values of $q_i$ and $n$ values of $\dot{q}_i$ at a particular time $t$. The connection of Lagrange equations of motion to Newtonian equations of motion can be seen in the following. Consider the case that the generalized coordinates are chosen to be the Cartesian coordinates $\mathbf{r}_i$, and the kinetic energy $K$ and potential energy $U$ of the system given by $K = \frac{1}{2}\sum_i m_i \dot{\mathbf{r}}_i^2$, $U = U(\mathbf{r}_1, ..., \mathbf{r}_n)$ respectively, the Lagrangian of the system is then simply $\mathcal{L} = \frac{1}{2}\sum_i m_i \dot{\mathbf{r}}_i^2 - U(\mathbf{r}_1, ..., \mathbf{r}_n)$. In this case

$$\frac{\partial \mathcal{L}}{\partial \dot{\mathbf{r}}_i} = m_i \dot{\mathbf{r}}_i, \quad \frac{\partial \mathcal{L}}{\partial \mathbf{r}_i} = -\boldsymbol{\nabla}_i U(\mathbf{r}_1, ..., \mathbf{r}_n). \tag{2.66}$$

The Lagrange equations of motion, the Eq. 2.64 then turns into

$$m_i \frac{d^2\mathbf{r}_i}{dt^2} + \boldsymbol{\nabla}_i U(\mathbf{r}_1, ..., \mathbf{r}_n) = 0 \tag{2.67}$$

which is nothing but Newtonian equations of motion.

The Hamiltonian formulation of classical mechanics [55] seeks to describe the motion of system in terms of first-order equations of motion by introducing the notion of conjugate momentum $p_i$, which is defined as

$$p_i = \frac{\partial \mathcal{L}(q_i, \dot{q}_i, t)}{\partial \dot{q}_i}. \tag{2.68}$$

The full differential of Lagrangian $\mathcal{L}(q_i, \dot{q}_i, t)$ can be written as

$$\begin{aligned} d\mathcal{L} &= \frac{\partial \mathcal{L}}{\partial q_i} dq_i + \frac{\partial \mathcal{L}}{\partial \dot{q}_i} d\dot{q}_i + \frac{\partial \mathcal{L}}{\partial t} dt \\ &= \dot{p}_i dq_i + p_i d\dot{q}_i + \frac{\partial \mathcal{L}}{\partial t} dt, \end{aligned} \tag{2.69}$$

where Einstein summation convention is applied for the repeated index $i$. The Hamiltonian of the system $\mathcal{H}$ is defined through the following Legendre transformation of the Lagrangian,

$$\mathcal{H}(q, p, t) = \dot{q}_i p_i - \mathcal{L}(q, \dot{q}, t). \tag{2.70}$$

This gives the full differential of $\mathcal{H}$ as

$$d\mathcal{H} = \dot{q}_i dp_i - \dot{p}_i dq_i - \frac{\partial \mathcal{L}}{\partial t} dt. \tag{2.71}$$

We then arrive at the Hamilton's equations of motion

$$\dot{q}_i = \frac{\partial \mathcal{H}}{\partial p_i}, \tag{2.72}$$

$$-\dot{p}_i = \frac{\partial \mathcal{H}}{\partial q_i}. \tag{2.73}$$

Compared to the Lagrange equations, the Hamilton equations of motion are first-order differential equations. However is is done at the expense of introducing new variables the conjugate momentum $p_i$. The evolution of the system is now described in $2n$ dimensional phase space whose coordinates are $\{q_i, p_i\}$.

For most of the cases considered in MD simulation, the Lagrangian of the system does not depend on time explicitly, namely $\frac{\partial \mathcal{L}}{\partial t} = 0$. From Eq. 2.71 we then have

$$\begin{aligned}\frac{d\mathcal{H}}{dt} &= \dot{q}_i \frac{dp_i}{dt} - \dot{p}_i \frac{dq_i}{dt} \\ &= \frac{\partial \mathcal{H}}{\partial p_i}\left(-\frac{\partial \mathcal{H}}{\partial q_i}\right) + \frac{\partial \mathcal{H}}{\partial q_i}\frac{\partial \mathcal{H}}{\partial p_i} \\ &= 0 \end{aligned} \tag{2.74}$$

Therefore, the Hamiltonian of the system is a constant of motion if the Lagrangian has no explicit dependence on time.

### 2.3.2 Constant Temperature Molecular Dynamics

Strictly speaking, temperature is only defined for a system at thermodynamic equilibrium, although separation of time and length scales usually makes the concepts of local thermodynamic equilibrium and local temperature useful. The thermodynamic definition of temperature is

$$\frac{1}{T} = \left(\frac{\partial S}{\partial E}\right)_{N,V}, \tag{2.75}$$

where $S$ is the entropy of the system. The microscopic expression for entropy is given by the Gibbs formula:

$$S = -k_\mathrm{B} \sum_i p_i \ln p_i, \tag{2.76}$$

where $k_\mathrm{B}$ is the Boltzmann constant and $p_i$ is the probability of the system at a microstate $i$. The summation is over all possible microstates of the system.

In MD simulation, it is impractical to calculate temperature using Eq. 2.75. Instead, the calculation of temperature in MD makes use of the equipartition theorem of classical statistical mechanics, which states that each individual degree of freedom that enters quadratically in the Hamiltonian is associated with average energy

$k_\mathrm{B}T/2$. Particularly, for the kinetic energy a particle, we have $\langle \frac{1}{2}m_i(v_i^\alpha)^2\rangle = \frac{1}{2}k_\mathrm{B}T$, where $v_i^\alpha$ is the $\alpha$ component of the particle velocity $\mathbf{v}_i$. For a system of $N$ particles in $d$ dimensions, the total number of freedom associated with kinetic energy will be $N_f = dN - N_c$, where $N_c$ is the number of internal constraints. Hence, the total kinetic energy of the system will be $\frac{1}{2}N_f k_\mathrm{B}T$, namely,

$$\langle K\rangle = \sum_{i=1}^{N}\left\langle \frac{1}{2}m_i\mathbf{v}_i^2\right\rangle = \frac{1}{2}N_f k_\mathrm{B}T. \tag{2.77}$$

This gives a formula for calculating the temperature of the system $T = \langle T(t)\rangle = \frac{2\langle K\rangle}{N_f k_\mathrm{B}}$, where the instantaneous temperature $T(t)$ is given by

$$T(t) = \sum_{i=1}^{N}\frac{m_i\mathbf{v}_i^2}{k_\mathrm{B}N_f}. \tag{2.78}$$

In a microcanonical ensemble, the total energy $E$ of the system is conserved. As the system explores different regions of the potential energy surface, the average kinetic energy of the system will change, meaning that the temperature of the system will evolve with time as well. To simulate a system under constant temperature, the most straightforward way would be using certain algorithms to keep the average kinetic energy of the system constant. The simplest example to achieve constant average kinetic energy by rescaling the velocity of the particles. However, such algorithms do not necessarily generate a canonical ensemble. A canonical ensemble is defined by the distribution function in phase space. If the Hamiltonian of a system is $\mathcal{H}(\{p,q\})$, the canonical distribution function is given by

$$f_{NVT}(\{p,q\}) = \frac{1}{Z_{NVT}}\exp\left[-\frac{\mathcal{H}(\{p,q\})}{k_\mathrm{B}T}\right], \tag{2.79}$$

where

$$Z(N,V,T) = \frac{1}{N!h^{3N}}\int dq^N dp^N \exp\left[-\frac{\mathcal{H}(\{p,q\})}{k_\mathrm{B}T}\right], \tag{2.80}$$

is the canonical partition function. The normalization condition for the distribution function is

$$\frac{1}{N!h^{3N}}\int dq^N dp^N f_{NVT}(\{p,q\}) = 1. \tag{2.81}$$

The canonical distribution is also called Boltzmann distribution.

The most widely used constant temperature MD method that generates canonical distribution, commonly referred to as the Nosé-Hoover thermostat, was originally due to Nosé [56] and refined by Hoover [57]. Nosé's constant temperature MD algorithm is based on the extended-Lagrangian formalism. The basic idea is to introduce a new coordinate $s$ that can exchange heat with the system by scaling the velocities of particles. The extended Lagrangian is

$$\mathcal{L} = \sum_i \frac{m_i}{2} s^2 \dot{\mathbf{r}}_i{}^2 - U(\{\mathbf{r}_i\}) + \frac{Q}{2}\dot{s}^2 - g k_\mathrm{B} T_\mathrm{obj} \ln s, \tag{2.82}$$

where $Q$ is the "effective mass" associated with $s$, $g = dN + 1$ is the total number of degrees of freedom in the system ($d$ is the number of dimensions), and $T_\mathrm{obj}$ is the externally set temperature of the system.

The conjugate momenta corresponding to $\mathbf{r}_i$ and $s$ are calculated from the Lagrangian using Eq. 2.68:

$$\mathbf{p}_i \equiv \frac{\partial \mathcal{L}}{\partial \dot{\mathbf{r}}_i} = m_i s^2 \dot{\mathbf{r}}_i \tag{2.83}$$

$$p_s \equiv \frac{\partial \mathcal{L}}{\partial \dot{s}} = Q\dot{s}. \tag{2.84}$$

The Hamiltonian for the extended system of the $N$ particles and the thermostat coordinates $s$ is then given by

$$\begin{aligned}\mathcal{H} &= \sum_i \mathbf{p}_i \cdot \dot{\mathbf{r}}_i + p_s \dot{s} - \mathcal{L} \\ &= \sum_i \frac{\mathbf{p}_i^2}{2m_i s^2} + U(\{\mathbf{r}_i\}) + \frac{p_s^2}{2Q} + \frac{g}{\beta}\ln s,\end{aligned} \tag{2.85}$$

where $\beta = 1/(k_\mathrm{B} T_\mathrm{obj})$. The Hamiltonian $\mathcal{H}$ is a conserved quantity for the extended system. The Hamilton's equations of motion are

$$\dot{\mathbf{r}}_i \equiv \frac{\partial \mathcal{H}}{\partial \mathbf{p}_i} = \frac{\mathbf{p}_i}{m_i s^2} \tag{2.86}$$

$$\dot{\mathbf{p}}_i \equiv -\frac{\partial \mathcal{H}}{\partial \mathbf{r}_i} = -\frac{\partial U(\{\mathbf{r}_i\})}{\partial \mathbf{r}_i} \tag{2.87}$$

$$\dot{s} \equiv -\frac{\partial \mathcal{H}}{\partial p_s} = \frac{p_s}{Q} \tag{2.88}$$

$$\dot{p}_s \equiv -\frac{\partial \mathcal{H}}{\partial s} = \sum_i \frac{\mathbf{p}_i^2}{m_i s^3} - \frac{g}{\beta s} \tag{2.89}$$

Nosé showed that [56], if the Hamiltonian $\mathcal{H}$ is the only conserved quantity, then the coordinates $\mathbf{r}_i$ and scaled momenta $\mathbf{p}'_i = \mathbf{p}_i/s$ generated by the equations of motion sample the canonical ensemble. This means that, if we define a Hamiltonian $H$ in the phase space spanned by $\{\mathbf{r}_i, \mathbf{p}'_i\}$,

$$H = \sum_i \frac{\mathbf{p}_i'^2}{2m_i} + U(\{\mathbf{r}_i\}), \tag{2.90}$$

then the phase space distribution function $f(\{\mathbf{r}_i, \mathbf{p}'_i\})$ is proportional to the Boltzmann weight $\exp[-\beta H(\{\mathbf{r}_i, \mathbf{p}'_i\})]$. Hence, the ensemble average for a quantity $\mathcal{A}$ expressed in terms of $\{\mathbf{r}_i, \mathbf{p}'_i\}$ reduces to the canonical average

$$\langle \mathcal{A}(\mathbf{r}, \mathbf{p}/s) \rangle_{\text{Nose}} = \langle \mathcal{A}(\mathbf{r}, \mathbf{p}') \rangle_{\text{NVT}} \,. \tag{2.91}$$

The left hand side of the above equation is calculated in simulation based on the equivalence between time average and ensemble average (assuming the dynamics is ergodic)

$$\langle \mathcal{A}(\mathbf{r}, \mathbf{p}/s) \rangle_{\text{Nose}} \equiv \lim_{\tau \to \infty} \frac{1}{\tau} \int_0^{\tau} dt \mathcal{A}[\mathbf{r}(t), \mathbf{p}(t)/s(t)]. \tag{2.92}$$

Nosé stated that the variable $s$ can be interpreted as a scaling factor for the time step $\Delta t$ in the simulation. The real time step $\Delta t'$ is related to the simulation time unit as $\Delta t' = \Delta t/s$. We can define two sets of variables, virtual variables in simulation (coordinates $\mathbf{r}_i$, momenta $\mathbf{p}_i$ and time $t$) and real variables ($\mathbf{r}'_i$, $\mathbf{p}'_i$, $t'$) for the corresponding physical systems. The two sets of variables are related as follows

$$\mathbf{r}'_i = \mathbf{r}_i \tag{2.93}$$

$$\mathbf{p}'_i = \mathbf{p}_i/s \tag{2.94}$$

$$\Delta t' = \Delta t/s \tag{2.95}$$

The real velocity $d\mathbf{r}'_i/dt'$ can then be expressed in terms of virtual velocity $d\mathbf{r}_i/dt$ as

$$\frac{d\mathbf{r}'_i}{dt'} = \frac{d\mathbf{r}_i}{dt/s} = s\frac{d\mathbf{r}_i}{dt}. \tag{2.96}$$

Hence, the scaling of velocity in the Nosé algorithm is self-consistent with scaling of time.

The difference between simulation time $t$ and real time $t'$, related to each other via $t' = \int^t dt/s$, can be inconvenient when computing time-dependent quantities, which are usually sampled using equal real time intervals. Nosé showed that [58], we can express the equations of motion (2.86)-(2.89) in terms of real variables, based on $\mathbf{r}'_i = \mathbf{r}_i$, $\mathbf{p}'_i = \mathbf{p}_i/s$, $t' = \int^t dt/s$, $s' = s$, and $p'_s = p_s/s$:

$$\frac{d\mathbf{r}'_i}{dt'} = \frac{\mathbf{p}'_i}{m_i}, \tag{2.97}$$

$$\frac{d\mathbf{p}'_i}{dt'} = -\frac{\partial U(\{\mathbf{r}'_i\})}{\partial \mathbf{r}'_i} - \frac{s'p'_s}{Q}\mathbf{p}'_i, \tag{2.98}$$

$$\frac{ds'}{dt'} = \frac{s'^2 p'_s}{Q}, \tag{2.99}$$

$$\frac{dp'_s}{dt'} = \left(\sum_i \frac{\mathbf{p}'^2_i}{m_i} - \frac{g}{\beta}\right)\frac{1}{s} - \frac{s'p'^2_s}{Q}. \tag{2.100}$$

The Hamiltonian $\mathcal{H}$ of Eq. 2.85 written in terms of the real variables,

$$\mathcal{H}' = \sum_i \frac{\mathbf{p}'^2_i}{2m_i} + U(\{\mathbf{r}'_i\}) + \frac{s'^2 p'^2_s}{2Q} + \frac{g}{\beta}\ln s', \tag{2.101}$$

is still a conserved quantity. Nosé proved that for the equations of motion in real variables, if we choose the number of degrees of freedom $g$ to be $dN$ instead of $dN+1$, then the real time average of quantities $\mathcal{A}(\mathbf{r}'_i, \mathbf{p}'_i)$ still converge to canonical average:

$$\lim_{\tau'\to\infty} \frac{1}{\tau'} \int_0^{\tau'} dt' \mathcal{A}[\mathbf{r}'(t'), \mathbf{p}'(t')] = \langle \mathcal{A}(\mathbf{r}', \mathbf{p}') \rangle_{\mathrm{NVT}} . \tag{2.102}$$

Hoover [57] showed that Eqs. (2.97)-(2.100) derived by Nosé can be further simplified by introducing a new variable $\xi \equiv s'p'_s/Q$. The real time equations of motion can then be written as

$$\frac{d\mathbf{r}'_i}{dt'} = \frac{\mathbf{p}'_i}{m_i}, \tag{2.103}$$

$$\frac{d\mathbf{p}'_i}{dt'} = -\frac{\partial U(\{\mathbf{r}'_i\})}{\partial \mathbf{r}'_i} - \xi \mathbf{p}'_i, \tag{2.104}$$

$$\frac{d\xi}{dt'} = \frac{1}{Q}\left(\sum_i \frac{\mathbf{p}'^2_i}{m_i} - \frac{g}{\beta}\right), \tag{2.105}$$

$$\frac{d \ln s'}{dt'} = \xi. \tag{2.106}$$

From Eq. 2.104, we can see that $\xi$ can be interpreted as a thermodynamic friction coefficient which couples to the velocities of particles. Eqs. (2.103)-(2.105) form a closed set, therefore are sufficient to generate the trajectories of the particles. However, Eq. 2.106 is still useful because the value of $\ln s$ is needed to check the conservation of $\mathcal{H}'$ in Eq. 2.101, which serves as an important self-consistency check for the numerical program. In terms of the new variable $\xi$, $\mathcal{H}'$ can be written as

$$\mathcal{H}' = \sum_i \frac{\mathbf{p}'^2_i}{2m_i} + U(\{\mathbf{r}'_i\}) + \frac{1}{2}Q\xi^2 + \frac{g}{\beta}\ln s' \tag{2.107}$$

Eq. 2.105 can be interpreted as follows. From Eq. 2.78, the instantaneous temperature of the system can be written as

$$T_{\mathrm{inst}} = \sum_i \frac{\mathbf{p}^2_i}{g k_{\mathrm{B}} m_i}. \tag{2.108}$$

Since $\beta = 1/(k_B T_{\text{obj}})$, Eq. 2.104 can be rewritten as

$$\frac{d\xi}{dt'} = \frac{g k_B T_{\text{obj}}}{Q} \left( \frac{T_{\text{inst}} - T_{\text{obj}}}{T_{\text{obj}}} \right). \tag{2.109}$$

This means that if the instantaneous temperature of the system $T_{\text{inst}}$ is higher than the target temperature $T_{\text{obj}}$, the value of $\xi$ will increase. When $\xi$ becomes positive, viscous drag forces opposite to the direction of velocity will act on the particles, gradually bringing back the temperature of the system. Similar argument can be said when $T_{\text{inst}}$ is lower than $T_{\text{obj}}$. This feedback mechanism ensures that $T_{\text{inst}}$ fluctuates around the target temperature $T_{\text{obj}}$. The time scale of temperature fluctuation is set by the effective thermal mass $Q$, which has the dimensions of energy $\cdot$ (time)$^2$. The characteristic time for temperature fluctuation can be estimated as $t_c = \sqrt{Q/(g k_B T_{\text{obj}})}$.

### 2.3.3 Constant Stress Molecular Dynamics

The basic idea of constant stress MD is allowing the size and shape of simulation box to change in response to the difference between the internal stress of the system and external applied stress tensor, such that the internal and external stress reach balance. The size and shape of the simulation box are fully determined by the basis vectors that span the edges of the supercell, which can be represented by the matrix $\mathbf{h} = (\mathbf{h}_1, \mathbf{h}_2, \mathbf{h}_3)$, where $\mathbf{h}_1$, $\mathbf{h}_2$ and $\mathbf{h}_3$ are the basis vectors. In constant stress MD, the individual elements of the matrix $\mathbf{h}$ will become dynamic variables. These additional degrees of freedom are considered to be new generalized coordinates and have their own equations of motion based on the method of extended Lagrangian pioneered by Anderson [59].

As the size and shape of the simulation box are constantly changing in constant stress MD, in Cartesian coordinates the positions of the particles needed to be constantly mapped to new ones via affine transformation. It then becomes more convenient to express the atomic coordinates $\mathbf{r}_i$ in terms of scaled coordinates $\mathbf{s}_i$, which are related to each other via

$$\begin{aligned} \mathbf{r}_i &= \mathbf{h} \cdot \mathbf{s}_i, & (2.110) \\ \mathbf{s}_i &= \mathbf{h}^{-1} \cdot \mathbf{r}_i. & (2.111) \end{aligned}$$

The squared distance between two particle $i$ and $j$ can then be expressed as

$$\begin{aligned} \mathbf{r}_{ij}^2 &= (\mathbf{r}_i - \mathbf{r}_j)^2 \\ &= (\mathbf{s}_i - \mathbf{s}_j)^T \mathbf{h}^T \mathbf{h} (\mathbf{s}_i - \mathbf{s}_j) \\ &\equiv (\mathbf{s}_i - \mathbf{s}_j)^T \mathbf{G} (\mathbf{s}_i - \mathbf{s}_j), \end{aligned} \tag{2.112}$$

where $\mathbf{G} = \mathbf{h}^T\mathbf{h}$ is the metric tensor.

The generalized coordinates for a system of $N$ particles now include the $3N$ components of scaled particle coordinates $\mathbf{s}_i$ and the nine components of the supercell matrix $\mathbf{h}$. To construct the Lagrangian of the extended system, one needs to specify the potential and kinetic energy associated with the new degrees of freedom. In the case that the externally applied stress tensor $\boldsymbol{\sigma}$ is hydrostatic, namely $\sigma_{ij} = -P\delta_{ij}$, Parrinello and Rahman proposed the following extended Lagrangian [60, 61]

$$\begin{aligned} \mathcal{L}_{\mathrm{PR}}(\mathbf{s}_i, \mathbf{h}, \dot{\mathbf{s}}_i, \dot{\mathbf{h}}) &= \frac{1}{2} \sum_{i=1}^{N} m_i \left|\mathbf{h}\dot{\mathbf{s}}_i\right|^2 - U(\{\mathbf{h}\mathbf{s}_i\}) + \frac{1}{2} W \left( |\dot{\mathbf{h}}_1|^2 + |\dot{\mathbf{h}}_2|^2 + |\dot{\mathbf{h}}_3|^2 \right) - PV \\ &= \frac{1}{2} \sum_{i=1}^{N} m_i \dot{\mathbf{s}}_i^T \mathbf{G} \dot{\mathbf{s}}_i - U(\{\mathbf{h}\mathbf{s}_i\}) + \frac{W}{2} \mathrm{Tr}\,(\dot{\mathbf{h}}^T \dot{\mathbf{h}}) - P \det(\mathbf{h}). \end{aligned} \tag{2.113}$$

where $W$ is the mass associated with the supercell degrees of freedom, and $V = \det(\mathbf{h})$ is the supercell volume. $\frac{W}{2}\mathrm{Tr}\,(\dot{\mathbf{h}}^T\dot{\mathbf{h}})$ and $PV$ represent the fictitious kinetic energy and potential energy of the supercell degrees of freedom, respectively. The equations of motion for $\mathbf{s}_i$ and $\mathbf{h}$ can then be derived from the above Lagrangian as

$$\frac{d}{dt}\left(\frac{\partial \mathcal{L}}{\partial \dot{\mathbf{s}}}\right) - \frac{\partial \mathcal{L}}{\partial \mathbf{s}_i} = 0, \tag{2.114}$$

$$\frac{d}{dt}\left(\frac{\partial \mathcal{L}}{\partial \dot{\mathbf{h}}}\right) - \frac{\partial \mathcal{L}}{\partial \mathbf{h}_i} = 0, \tag{2.115}$$

which gives

$$\ddot{\mathbf{s}}_i = -\frac{\mathbf{G}^{-1}}{m_i}\frac{\partial U(\{\mathbf{h}\mathbf{s}_i\})}{\partial \mathbf{s}_i} - \mathbf{G}^{-1}\dot{\mathbf{G}}\dot{\mathbf{s}}_i, \tag{2.116}$$

$$\ddot{\mathbf{h}} = \frac{1}{W}\left(\sum_i m_i \mathbf{h}\dot{\mathbf{s}}_i \otimes \dot{\mathbf{s}}_i - \frac{\partial U(\{\mathbf{h}\mathbf{s}_i\})}{\partial \mathbf{s}_i} - P\Xi\right). \tag{2.117}$$

Above, $\Xi = \partial \det(\mathbf{h})/\partial \mathbf{h} = \det(\mathbf{h})(\mathbf{h}^{-1})^T$. Using the following relations

$$\frac{\partial U\{\mathbf{h}\mathbf{s}_i\}}{\partial \mathbf{s}_i} = \mathbf{h}^T \frac{\partial U(\{\mathbf{r}_i\})}{\partial \mathbf{r}_i}, \tag{2.118}$$

$$\frac{\partial U\{\mathbf{h}\mathbf{s}_i\}}{\partial \mathbf{h}_i} = \sum_i \left(\frac{\partial U(\{\mathbf{r}_i\})}{\partial \mathbf{r}_i} \otimes \mathbf{r}_i\right)(\mathbf{h}^{-1})^T, \tag{2.119}$$

$$\mathbf{h}\dot{\mathbf{s}}_i \otimes \dot{\mathbf{s}}_i = \dot{\mathbf{r}}_i \otimes \dot{\mathbf{r}}_i \left(\mathbf{h}^{-1}\right)^T, \tag{2.120}$$

Eqs. (2.116)-(2.117) can be further simplified and written in terms real space coordinates $\mathbf{r}_i$ as

$$\ddot{\mathbf{r}}_i = -\frac{1}{m_i}\frac{\partial U(\{\mathbf{r}_i\})}{\partial \mathbf{r}_i} - (\mathbf{h}^T)^{-1}\dot{\mathbf{G}}\mathbf{h}^{-1}\dot{\mathbf{r}}_i, \tag{2.121}$$

$$\ddot{\mathbf{h}} = -\frac{1}{W}(\boldsymbol{\sigma}_{\text{int}} + P\mathbf{I})\Xi, \tag{2.122}$$

where $\boldsymbol{\sigma}_{\text{int}}$ is the microscopic stress tensor of the system

$$\boldsymbol{\sigma}_{\text{int}} = \frac{1}{V}\sum_i \left(-m_i \dot{\mathbf{r}}_i \otimes \dot{\mathbf{r}}_i + \frac{\partial U(\{\mathbf{r}_i\})}{\partial \mathbf{r}_i} \otimes \mathbf{r}_i\right). \tag{2.123}$$

The feedback mechanism of barostat is built into Eq. 2.122. The supercell expands when the internal pressure of the system becomes larger than the external pressure, and changes shape when the internal stress tensor contains non-zero elements.

The Hamiltonian of the system can be obtained from the Lagrangian of Eq. 2.113 through Legendre transformation, which gives

$$\mathcal{H}_{\mathrm{PR}} = \frac{1}{2}\sum_{i=1}^{N} m_i \dot{\mathbf{s}}_i^T \mathbf{G} \dot{\mathbf{s}}_i + U(\{\mathbf{h}\mathbf{s}_i\}) + \frac{W}{2}\mathrm{Tr}\,(\dot{\mathbf{h}}^T \dot{\mathbf{h}}) + PV. \tag{2.124}$$

$\mathcal{H}_{\mathrm{PR}}$ is the constant of motion for the extended system of particles and barostat. According to equipartition theorem, in equilibrium and at temperature $T$, the third term of the above Hamiltonian $\frac{W}{2}\mathrm{Tr}\,(\dot{\mathbf{h}}^T\dot{\mathbf{h}})$, which is the kinetic energy of the supercell degrees of freedom, has an average value of $9/2k_{\mathrm{B}}T$. In comparison, the first term, which is the kinetic energy of the particles in the system, has an average of $3N/2k_{\mathrm{B}}T$. Therefore, in the limit of large $N$, the constant of motion is the enthalpy,

$$H = E + PV, \tag{2.125}$$

where

$$E = \frac{1}{2}\sum_{i=1}^{N} m_i \dot{\mathbf{s}}_i^T \mathbf{G} \dot{\mathbf{s}}_i + U(\{\mathbf{h}\mathbf{s}_i\}) = \frac{1}{2}\sum_{i=1}^{N} m_i |\dot{\mathbf{r}}_i|^2 + U(\{\mathbf{r}_i\}). \tag{2.126}$$

Therefore, the Lagrangian in Eq. 2.113 generates constant pressure and enthalpy ($NPH$) ensemble [59, 60, 61].

In the case arbitrary external stress tensor $\boldsymbol{\sigma}$ is applied on the system, the potential energy of the supercell degrees of freedom in the Lagrangian of Eq. 2.113 needs to be modified. Choosing a reference supercell $\mathbf{h}_0$, which is usually taken to be the supercell $\mathbf{h}$ at the beginning of the simulation or the average value of $\mathbf{h}$ during the simulation, the potential energy associated with the supercell can be written as [61, 62]

$$U_{\mathrm{cell}} = P(V - V_0) + V_0\,\mathrm{Tr}\,(\boldsymbol{\sigma} + P\mathbf{I})\boldsymbol{\epsilon}. \tag{2.127}$$

The first term on the right hand side of the above equation takes into account of the effect of the hydrostatic component of stress tensor $\sigma$, which is defined as $P = -\frac{1}{3}\mathrm{Tr}\,\boldsymbol{\sigma}$, while the second term is due to the deviatoric stress components. The strain tensor

$\boldsymbol{\epsilon}$ is calculated as

$$\boldsymbol{\epsilon} = \frac{1}{2}\left(\mathbf{h}_0^{-T}\mathbf{h}^T\mathbf{h}\mathbf{h}_0^{-1} - \mathbf{I}\right) = \frac{1}{2}\left(\mathbf{h}_0^{-T}\mathbf{G}\mathbf{h}_0^{-1} - \mathbf{I}\right). \tag{2.128}$$

Substituting the above expression for $\boldsymbol{\epsilon}$ into Eq. 2.127, we obtain

$$\begin{aligned} U_{\text{cell}} &= P(V - V_0) + \frac{V_0}{2}\text{Tr}\left[(\boldsymbol{\sigma} + P\mathbf{I})\mathbf{h}_0^{-T}\mathbf{G}\mathbf{h}_0^{-1}\right] - \frac{V_0}{2}\text{Tr}\,(\boldsymbol{\sigma} + P\mathbf{I}) \\ &= P(V - V_0) + \frac{V_0}{2}\text{Tr}\left[\mathbf{h}_0^{-1}(\boldsymbol{\sigma} + P\mathbf{I})\mathbf{h}_0^{-T}\mathbf{G}\right] \\ &= PV + \frac{V_0}{2}\text{Tr}\,(\boldsymbol{\Sigma}\mathbf{G}) - PV_0 \end{aligned} \tag{2.129}$$

where $\boldsymbol{\Sigma} \equiv \mathbf{h}_0^{-1}(\boldsymbol{\sigma}+P\mathbf{I})\mathbf{h}_0^{-T}$. The constant term $PV_0$ in $U_{\text{cell}}$ has no effect on the equations of motion and can be dropped out. Hence the Parrinello-Rahman Lagrangian for arbitrary stress becomes

$$\begin{aligned} \mathcal{L}'_{\text{PR}} &= \mathcal{L}_{\text{PR}} - \frac{V_0}{2}\text{Tr}\,(\boldsymbol{\Sigma}\mathbf{G}) \\ &= \frac{1}{2}\sum_{i=1}^{N} m_i\dot{\mathbf{s}}_i^T\mathbf{G}\dot{\mathbf{s}}_i - U(\{\mathbf{h}\mathbf{s}_i\}) + \frac{W}{2}\text{Tr}\,(\dot{\mathbf{h}}^T\dot{\mathbf{h}}) - P\det(\mathbf{h}) - \frac{V_0}{2}\text{Tr}\,(\boldsymbol{\Sigma}\mathbf{G}). \end{aligned} \tag{2.130}$$

The equations of motion for $\mathbf{s}_i$ remain the same as Eq. 2.116, as the additional term in the Lagrangian $\frac{V_0}{2}\text{Tr}\,(\boldsymbol{\Sigma}\mathbf{G})$ has no dependence on $\mathbf{s}_i$. The equations of motion for $\mathbf{h}$ are modified to be

$$\ddot{\mathbf{h}} = -\frac{1}{W}\left[(\boldsymbol{\sigma}_{\text{int}} + P\mathbf{I})\boldsymbol{\Xi} + V_0\mathbf{h}\boldsymbol{\Sigma}\right]. \tag{2.131}$$

The constant of motion is the generalized enthalpy

$$H' = E + PV + \frac{V_0}{2}\text{Tr}\,(\boldsymbol{\Sigma}\mathbf{G}). \tag{2.132}$$

### 2.3.4 Constant Temperature and Stress Molecular Dynamics

Constant temperature and stress MD can be achieved be combining thermostat and barostat together. The widely used equations of motion that generate constant temperature and stress ensemble are those proposed by Martyna *et al.* [63], which were generalized by Shinoda *et al.* [64] to treat systems under arbitrary external stress using the supercell strain energy formula of Parrinello and Rahman (Eq. 2.129) [61]. These equations of motions are

$$\begin{aligned}
\dot{\mathbf{r}}_i &= \frac{\mathbf{p}_i}{m_i} + \frac{\mathbf{p}_g}{W_g}\mathbf{r}_i, && (2.133)\\
\dot{\mathbf{p}}_i &= \mathbf{F}_i - \frac{\mathbf{p}_g}{W_g}\mathbf{p}_i - \frac{1}{N_f}\frac{\mathrm{Tr}[\mathbf{p}_g]}{W_g}\mathbf{p}_i - \frac{p_\xi}{Q}\mathbf{p}_i, && (2.134)\\
\dot{\mathbf{h}} &= \frac{\mathbf{p}_g}{W_g}\mathbf{h}, && (2.135)\\
\dot{\mathbf{p}}_g &= V(\mathbf{P}_{\mathrm{int}} - P_{\mathrm{ext}}\mathbf{I}) - V_0\mathbf{h}\mathbf{\Sigma}\mathbf{h}^T + \left(\frac{1}{N_f}\sum_{i=1}^{N}\frac{\mathbf{p}_i^2}{m_i}\right)\mathbf{I} - \frac{p_\xi}{Q}\mathbf{p}_g, && (2.136)\\
\dot{\xi} &= \frac{p_\xi}{Q}, && (2.137)\\
\dot{p}_\xi &= \sum_{i=1}^{N}\frac{\mathbf{p}_i^2}{m_i} + \frac{1}{W_g}\mathrm{Tr}[\mathbf{p}_g^T\mathbf{p}_g] - (N_f + d^2)k_{\mathrm{B}}T_{\mathrm{ext}}, && (2.138)
\end{aligned}$$

where $\{\mathbf{r}_i, \mathbf{p}_i\}$ are the position and momentum of particle $i$, $\mathbf{h}$ is the matrix representing the generalized coordinates associate with the supercell degrees of freedom, $\mathbf{p}_g$ is the modularly invariant [65, 66, 63] form of the supercell momenta, and $\{\xi, p_\xi\}$ are the thermostat variable and its conjugate momentum. $W_g$ and $Q$ are the mass of barostat and thermostat respectively. $N_f$ is the number of degrees of freedom in the system, which is equal to $dN$ if there is no constraint for the particle motion in a system of $N$ particles in $d$ dimensions. $P_{\mathrm{ext}} = -\frac{1}{3}\mathrm{Tr}\boldsymbol{\sigma}$ is the hydrostatic component of the externally applied stress tensor $\boldsymbol{\sigma}_{\mathrm{ext}}$. $T_{\mathrm{ext}}$ is the target temperature of the thermostat. $V_0 = \det(\mathbf{h}_0)$ is the volume of the reference supercell, which is usually taken to be the supercell $\mathbf{h}$ at the beginning of simulation or the average value of $\mathbf{h}$ during simulation. $\mathbf{\Sigma}$ has the same definition as discussed earlier in Parrinello-Rahman constant stress MD, namely $\mathbf{\Sigma} = \mathbf{h}_0^{-1}(\boldsymbol{\sigma}_{\mathrm{ext}} + P_{\mathrm{ext}}\mathbf{I})\mathbf{h}_0^{-T}$. The internal pressure $\mathbf{P}_{\mathrm{int}}$ is defined as

$$(P_{\mathrm{int}})_{\alpha\beta} = \frac{1}{V}\left[\sum_{i}^{N} \frac{(\mathbf{p}_i)_\alpha(\mathbf{p}_i)_\beta}{m_i} + (\mathbf{F}_i)_\alpha(\mathbf{r}_i)_\beta - (\mathbf{u}'\mathbf{h}^T)_{\alpha\beta}\right], \tag{2.139}$$

$$(\mathbf{u}')_{\alpha\beta} = \frac{\partial U(\{\mathbf{r}_i\},\mathbf{h})}{\partial(h)_{\alpha\beta}}, \tag{2.140}$$

where $U(\{\mathbf{r}_i\},\mathbf{h})$ is the potential energy of the particles. The above equations of motions have the following conserved quantity,

$$\begin{aligned} H' = &\sum_{i=1}^{N} \frac{\mathbf{p}_i^2}{2m_i} + U(\{\mathbf{r}_i\},\mathbf{h}) + \frac{1}{2W_g}\mathrm{Tr}[\mathbf{p}_g^T\mathbf{p}_g] + P_{\mathrm{ext}}\det[\mathbf{h}] + \frac{V_0}{2}\mathrm{Tr}\left(\mathbf{\Sigma}\mathbf{G}\right) \\ &+ \frac{p_\xi^2}{2Q} + (N_f + d^2)k_{\mathrm{B}}T_{\mathrm{ext}}\xi \end{aligned} \tag{2.141}$$

In the equations of motion above, a single Nosé-Hoover thermostat was coupled to the particles and supercell variables. The Nosé-Hoover algorithm only generates the correct distribution if there is a single constant of motion [45], and in some cases the system may not behave as expected[67]. To over come these difficulties, the Nosé-Hoover chain method has been developed [68]. In this method, the Nosé-Hoover thermostat is coupled with other thermostats to form a chain of thermostats. If a system of $M$ Nośe-Hoover chains are used together with the barostat, the equations of motion for the thermostat variables and their conjugate momenta $\{\xi_k, p_{\xi_k}\}$ become [64]

$$\dot{\xi} = \frac{p_{\xi_k}}{Q_k} \qquad k = 1,\ldots,M, \tag{2.142}$$

$$\dot{p}_{\xi_1} = \sum_{i=1}^{N} \frac{\mathbf{p}_i^2}{m_i} + \frac{1}{W_g}\mathrm{Tr}[\mathbf{p}_g^T\mathbf{p}_g] - (N_f + d^2)k_{\mathrm{B}}T_{\mathrm{ext}} - p_{\xi_1}\frac{p_{\xi 2}}{Q_2}, \tag{2.143}$$

$$\dot{p}_{\xi_k} = \left(\frac{p_{\xi_{k-1}}^2}{Q_{k-1}} - kT_{\mathrm{ext}}\right) - p_{\xi_k}\frac{p_{\xi_{k+1}}}{Q_{k+1}} \qquad k = 2,\ldots,M-1 \tag{2.144}$$

$$\dot{p}_{\xi_M} = \left(\frac{p_{\xi_{M-1}}^2}{Q_{M-1}} - kT_{\mathrm{ext}}\right). \tag{2.145}$$

The conserved quantity has additional terms due to the added thermostats

$$H'' = H' + \sum_{k=2}^{M} \left( \frac{p_{\xi_k}^2}{2Q_k} + kT_{\mathrm{ext}}\xi_k \right) . \tag{2.146}$$

# Chapter 3

# Envelope Function Method for Electrons in Slowly-Varying Inhomogeneously Strained Crystals

## 3.1 Introduction

It has long been recognized that elastic strain can be used to tune the properties of materials. This idea of elastic strain engineering (ESE) is straightforward because the derivative of a material property $P$ with respect to applied elastic strain $\varepsilon$, $\partial P/\partial\varepsilon$, is in-general non-zero [12]. However, ESE has traditionally been limited by the small amount of elastic strain a material can accommodate, before plastic deformation or fracture occurs. Recent experiments, however, reveal a class of ultra-strength materials [12] whose elastic strain limit can be significantly higher than conventional bulk solids. Notable examples are two-dimensional (2D) atomic crystals such as graphene and monolayer molybdenum disulfide ($MoS_2$)[69]. The experimentally measured elastic strain limit of graphene can be as high as 25% [13, 70], while that of bulk graphite seldom reaches 0.1%. Monolayer $MoS_2$ can also sustain effective in-plane strain up to 11% [14]. Such large elastic strain limit make it possible to induce significant material property changes by imposing elastic strain. In particular, position-dependent properties can be induced by applying *inhomogeneous* strain which is slowly varying at atomic scale but has large sample-wide difference. For instance, Feng *et al.* demonstrated that indenting a suspended $MoS_2$ monolayer can create a local electronic bandgap profile in the monolayer with $1/r$ spatial variation, $r$ being the distance to the center of indenter tip [71]. This creates an "artificial atom" in which electrons moves in a semiclassical potential resembling that of a two-dimensional hydrogenic atom. In this article, we will develop a new envelope function formalism that could be used to study the electronic structure of such slowly-varying inhomogeneously strained crystals.

*Ab initio* electronic structure methods such as density functional theory (DFT) are nowadays routinely used to calculate the properties of materials. However, the steep scaling of computational cost with respect to system size limits their use to periodic solids, surfaces and small clusters. An inhomogeneously strained structure usually involves a large number of atoms and thus fall beyond the current capabilities of these methods.

In the past, several semi-empirical electronic structure methods capable of treating systems larger than *ab initio* methods have been developed to study the electrical and optical properties of semiconductor nanostructures. Among those the most notable are the empirical tight binding method [72, 73], empirical pseudopotential method (EPM) [74, 75, 76] and multi-band $\mathbf{k} \cdot \mathbf{p}$ envelope function method [77, 78, 79, 80, 81, 82]. Both tight-binding and EPM are microscopic methods [73] that treat the electronic structure at the level of atoms, while the multi-band $\mathbf{k} \cdot \mathbf{p}$ envelope function method describes electronic structure at the level of the envelope of wavefunctions, whose lengthscale is in general much larger than the lattice constant. Excellent articles discussing the merits and shortcomings of these methods exist in the literature [73, 74]. Below we shall briefly review the multi-band $\mathbf{k} \cdot \mathbf{p}$ envelope function method and the EPM method, as these two methods have been demonstrated to treat vary large nanostructures (up to a million atoms [83, 76]) and are most relevant to our article.

The starting point of wavefunction based semi-empirical electronic structure methods is usually the single-particle Schrödinger equation:

$$\left[\frac{\mathbf{p}^2}{2m} + V(\mathbf{r})\right] \Psi(\mathbf{r}) = E\Psi(\mathbf{r}). \tag{3.1}$$

Here $V(\mathbf{r})$ is the crystal potential; $\Psi(\mathbf{r})$ is the electronic wavefunction. In $\mathbf{k}\cdot\mathbf{p}$ envelope function method, $\Psi(\mathbf{r})$ is expanded in terms of a complete and orthonormal basis set $\chi_{n\mathbf{k}_0} = e^{i\mathbf{k}\cdot\mathbf{r}}\psi_{n\mathbf{k}_0}(\mathbf{r})$ [77], where $\psi_{n\mathbf{k}_0}(\mathbf{r})$ represent the Bloch functions of the underlying periodic solid at a reference crystal momentum $\mathbf{k}_0$. Mathematically, the expansion is written as

$$\Psi(\mathbf{r}) = \sum_{n\mathbf{k}} c_{n\mathbf{k}} \left\{ e^{i\mathbf{k}\cdot\mathbf{r}}\psi_{n\mathbf{k}_0}(\mathbf{r}) \right\}. \tag{3.2}$$

The summation is over band index $n$ and wave vector $\mathbf{k}$, which is restricted to the first Brillouin zone (BZ) of the crystal. This expansion can be re-written as

$$\Psi(\mathbf{r}) = \sum_n \left( \sum_{\mathbf{k}} c_{n\mathbf{k}} e^{i\mathbf{k}\cdot\mathbf{r}} \right) \psi_{n\mathbf{k}_0}(\mathbf{r}) = \sum_n F_n(\mathbf{r})\psi_{n\mathbf{k}_0}(\mathbf{r}). \tag{3.3}$$

The functions $F_n(\mathbf{r}) = \sum_{\mathbf{k}} c_{n\mathbf{k}} e^{i\mathbf{k}\cdot\mathbf{r}}$ are called envelope functions because they are smooth functions at the unit-cell level due to the restriction of wave vector $\mathbf{k}$ within the first BZ. If all bands $n$ are kept, the above expansion is complete. In practical calculation, only a few bands close to Fermi energy are included. The reference crystal momentum $\mathbf{k}_0$ is normally chosen to be the wave vector corresponding to the valence band maximum or conduction band minimum of a semiconductor.

Using this expansion, the Schrödinger equation can be turned into coupled differential equations for the envelope functions in the following general form

$$\sum_n H(\mathbf{r}, \nabla)_{mn} F_n(\mathbf{r}) = E F_m(\mathbf{r}). \tag{3.4}$$

In $\mathbf{k}\cdot\mathbf{p}$ envelope function method, $H(\mathbf{r}, \nabla)$ is assumed to have the same form as the $\mathbf{k}\cdot\mathbf{p}$ Hamiltonian for bulk crystal [84], after replacing the momentum operators $k_x$, $k_y$, $k_z$ in $\mathbf{k}\cdot\mathbf{p}$ Hamiltonian by $-i\partial/\partial x$, $-i\partial/\partial y$, and $-i\partial/\partial z$ [77, 78, 79]. The empirical parameters in $\mathbf{k}\cdot\mathbf{p}$ Hamiltonian are fitted to the observed properties of bulk crystals or nanostructures themselves. A Numerical solution of the coupled differential equations gives energy eigenvalues and the associated envelope functions. This method has been successfully applied to semiconductor superlattice [78, 80], quantum wires [85], and quantum dots [23, 86].

The $\mathbf{k}\cdot\mathbf{p}$ envelope function method can treat the effect of homogeneous strain by incorporating it as deformation potential [87, 88, 89, 80]. Deformation potential theory assumes small applied strain, such that the strain-induced band edge shift of bulk crystals can be expanded to first-order in terms of the applied strain tensor $\varepsilon$, $\Delta E = \sum_{ij} \Xi_{ij}\varepsilon_{ij}$, where $\Xi_{ij}$ are deformation potentials. A detailed practical implementation of deformation potential in $\mathbf{k}\cdot\mathbf{p}$ envelope function method can be found in literature [80]. Extension of the $\mathbf{k}\cdot\mathbf{p}$ envelope function method to inhomogeneous strain was carried out by Zhang [90].

The EPM method [91, 74, 76] is another well-known approach to nanostructure electronic structure calculation. EPM solves the single-particle Schrödinger equation non-self-consistently through the use of empirical pseudopotential. In EPM, the crystal potential $V(\mathbf{r})$ is represented as a superposition of screened spherical atomic pseudo-potentials [74]

$$V(\mathbf{r}) = \sum_{\text{atom}} v_{\text{atom}}(\mathbf{r} - \mathbf{R}_{\text{atom}}). \tag{3.5}$$

The atomic pseudo-potentials can be extracted from DFT local density-approximation (LDA) calculations on bulk systems, and then empirically adjusted to correct the LDA band structure error [92]. As the laborious self-consistent potential determination procedures in *ab-initio* calculation are avoided, EPM is computationally cheaper and faster, enabling it to treat large nanostructures [75]. Zunger and collaborators showed that EPM can be more advantageous to $\mathbf{k}\cdot\mathbf{p}$ method due to its non-perturbative nature as well as preservation of atomic-level structural details [93, 94]. EPM treats strain effects by weighting the atomic pseudopotentials with a scalar pre-factor fitted to observed properties of strained crystals [76]. While EPM is appealing in many ways, its wide use is limited by the complications involved in pseudopotential fitting and Hamiltonian diagonalization.

In this article, we develop a new envelope function formalism to solve the electronic states in slowly-varying inhomogeneously strained semiconductor crystals. We aim to develop a method that takes advantage of the numerical efficiency of multi-band $\mathbf{k}\cdot\mathbf{p}$ envelope function method, while at the same time incorporates certain microscopic electronic structure information at the level of *ab intio* or EPM method. In speaking of a slowly-varying inhomogeneously strained semiconductor crystal, we mean that the variation of strain in the crystal is very small over the distance of a unit cell, but can be quite large sample-wide (more than a few percent). Our method assumes, with justification, that in such slowly-varying inhomogeneously strained semiconductors, the local crystal potential at the unit-cell level can be well approximated by that of a homogeneously strained crystal with the same strain magnitude. Hence, significant amount of local electronic structure information can be obtained from unit-cell level *ab inito* or EPM calculation of homogeneously strained crystals, which can then be incorporated into the solution of global electronic structure using the framework of envelop function method. To achieve such local to global electronic structure connection, the global wavefunctions will be expanded in terms of a small set of Bloch functions *parametrized* to the strain field $\varepsilon(\mathbf{x})$ in the deformed crystal, each of which is multiplied by a slowly varying envelope function. The strain-parametrized Bloch functions are constructed by smoothly connecting the Bloch functions of homogeneously strained crystals, a process made possible by a coordinate transformation method that maps the deformed crystal back to a undeformed one with deformed crystal potential. This set of strain-parametrized Bloch functions, together with strain-parametrized energy eigenvalues associated with those Bloch functions, can then be used to eliminate the unknown crystal potential term in the global Schröinger equation for the inhomogeneously strained crystal. The electronic structure problem will subsequently be turned into a set of coupled differential equations for the envelope functions, and solved as a generalized matrix eigenvector problem. Due to the slowly-varying nature of the envelope functions, coarse spatial or Fourier grid can be used to represent them, therefore reduces the computational cost of the method compared to full-scale *ab initio* or (potentially) EPM calculation of the inhomogeneously strained crystals.

The structure of this chapter is as follows. In Sec. 3.2, we lay out the general formalism of our envelope function method for slowly-varying inhomogeneously strain crystals. To demonstrate its effectiveness, we will apply the method to a model one-dimensional strained semiconductor in Sec. 3.3. In Sec. 3.4, we will discuss the practical issues when applying the method to three-dimensional realistic solids. Finally, we will derive in Sec. 3.5 a set of differential eigenvalue equations for the envelope functions when our method is used as a purely empirical fitting scheme.

## 3.2 Formalism

### 3.2.1 Coordinate Transformation

To facilitate the formulation of our envelope function method for slowly-varying inhomogeneously strained crystal, we first elaborate a coordinate transformation method which converts the electronic structure problem of a deformed crystal to a undeformed one with deformed crystal potential. This approach has been employed to study electron-phonon interactions [95], and to prove extended Cauchy-Born rule for smoothly deformed crystals [96, 97, 98]. The construction here partly follows E *et al* [98].

In laboratory Cartesian coordinates, denote by $\mathbf{X}_i$ and $\mathbf{X}'_i$ the position vectors of the $i$-th atom in a crystal before and after deformation, we can write

$$\mathbf{X}'_i = \mathbf{X}_i + \mathbf{U}_i. \tag{3.6}$$

Above, $\mathbf{U}_i$ is the displacement of the $i$-th atom. $\mathbf{U}_i$ is assumed to follow a smooth displacement field $\mathbf{u}(\mathbf{x})$ in the smoothly deformed crystal, *i.e.*, there exists a smooth displacement field $\mathbf{u}(\mathbf{x})$, which maps every atom in the crystal to a new position $\mathbf{X}'_i = \mathbf{X}_i + \mathbf{u}(\mathbf{X}_i)$. This assumption is closely related to the Cauchy-Born rule [99] in solid mechanics.

Since the smooth displacement field $\mathbf{u}(\mathbf{x})$ is defined for every point in the space, it can be used to map a function as well. For example, if a function $f(\mathbf{x})$ is originally defined for an unstrained crystal, which for example can be the crystal potential $V(\mathbf{x})$ or wavefunction $\Psi(\mathbf{x})$, after mapping it becomes a new function $h(\mathbf{x}')$ given by

$$h(\mathbf{x}+\mathbf{u}(\mathbf{x})) = f(\mathbf{x}), \tag{3.7}$$

since the value of function $h(\mathbf{x}')$ at point $\mathbf{x}' = \mathbf{x} + \mathbf{u}(\mathbf{x})$ is mapped from function $f(\mathbf{x})$ at point $\mathbf{x}$. This mapping of a known function defined in a undeformed crystal to a deformed crystal can be done reversely. Suppose, for example, the crystal potential of a deformed crystal is $V(\mathbf{x}')$, it can be mapped back to a function $V^*(\mathbf{x})$ defined in the "undeformed coordinates" $\mathbf{x}$ as

$$V^*(\mathbf{x}) = V(\mathbf{x} + \mathbf{u}(\mathbf{x})). \tag{3.8}$$

Namely, the value of function $V^*(\mathbf{x})$ at position $\mathbf{x}$ is the same as the value of function $V(\mathbf{x}')$ at $\mathbf{x}' = \mathbf{x}+\mathbf{u}(\mathbf{x})$. Hereafter, the appearance of the superscript "$*$" on a function denotes that the function has been mapped back to undeformed coordinates $\mathbf{x}$ with the following general mapping rule

$$f^*(\mathbf{x}) = f(\mathbf{x} + \mathbf{u}(\mathbf{x})), \tag{3.9}$$

where $f(\mathbf{x}')$ is a function defined for a deformed crystal.

We can apply the above mapping, which is essentially a nonlinear coordinate transformation, to differential operators as well, such as the Hamiltonian operator in the Schrödinger equation. In Hartree atomic units, the Schrödinger equation for deformed crystal reads

$$\left[-\frac{1}{2}\Delta + V(\mathbf{x}')\right] \Psi(\mathbf{x}') = E\Psi(\mathbf{x}'), \tag{3.10}$$

where $\Delta$ is the Laplacian. Applying the following deformation mapping (coordinate transformation) to the Schrödinger equation,

$$\mathbf{x}' = \mathbf{x} + \mathbf{u}(\mathbf{x}), \tag{3.11}$$

it will be transformed into the undeformed coordinates $\mathbf{x}$ as

$$\left[-\frac{1}{2}\Delta^* + V^*(\mathbf{x})\right]\Psi^*(\mathbf{x}) = E\Psi^*(\mathbf{x}). \tag{3.12}$$

$\Delta^*$, $V^*(\mathbf{x})$ and $\Psi^*(\mathbf{x})$ are the Laplacian, crystal potential and wavefunctions mapped to undeformed coordinates, respectively. $\Delta^*$ can be explicitly written out as

$$\begin{aligned} \Delta^* &= \left((I + \nabla\mathbf{u})^{-T}\nabla\right) \cdot \left((I + \nabla\mathbf{u})^{-T}\nabla\right) \\ &\equiv a_{ij}(\mathbf{x})\frac{\partial^2}{\partial x_i \partial x_j} + b_i(\mathbf{x})\frac{\partial}{\partial x_i}, \end{aligned} \tag{3.13}$$

where $a_{ij}(\mathbf{x})$ and $b_i(\mathbf{x})$ are given by

$$a_{ij}(\mathbf{x}) = (I + \nabla\mathbf{u}(\mathbf{x}))^{-1}_{im}\,(I + \nabla\mathbf{u}(\mathbf{x}))^{-T}_{mj}\,, \tag{3.14}$$

$$b_i(\mathbf{x}) = (I + \nabla\mathbf{u}(\mathbf{x}))^{-1}_{nm}\,\frac{\partial}{\partial x_n}\,(I + \nabla\mathbf{u}(\mathbf{x}))^{-T}_{mi}\,. \tag{3.15}$$

Above, $\nabla\mathbf{u}$ is the deformation gradient matrix (field) whose elements are given by $(\nabla\mathbf{u})_{mn} = \partial u_m/\partial x_n$. $I$ is identity matrix. The superscript $-1$ denotes matrix inversion; $-T$ denotes matrix inversion *and* transposition. Einstein summation applies when an index is repeated. It can be checked that when $\mathbf{u}(\mathbf{x}) = 0$, *i.e.*, the crystal is undeformed, $a_{ij}(\mathbf{x}) = \delta_{ij}$, $b_i(\mathbf{x}) = 0$, leaving the Laplacian untransformed.

### 3.2.2 Strain-Parametrized Expansion Basis

To proceed with our envelope function expansion for inhomogeneously strained crystals, we first imagine a series of *homogeneously* strained crystals with different strain tensors $\varepsilon$, all of which are then mapped back to undeformed coordinates following the same coordinate transformation elaborated in the previous section. Fig. 5-1 illustrates this procedure. For a homogeneously strained crystal, we can choose the

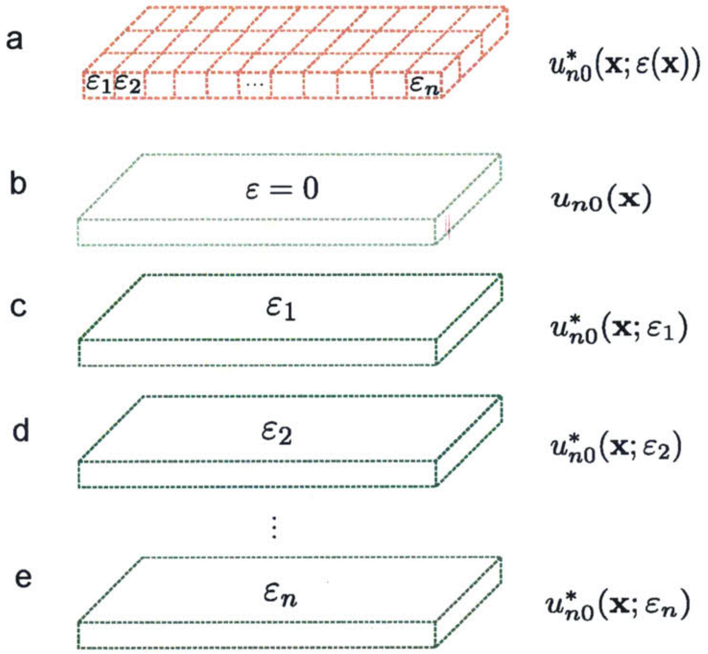

Figure 3-1: Schematic of strained crystals mapped back to undeformed coordinates. After mapping, the atomic coordinates of a strained crystal will be the same as those of a undeformed crystal, but the crystal potential will be different. (a) Inhomogeneously strained crystal. The local strain $\varepsilon_n$ are labeled. (b) Unstrained crystal. (c-e) Homogeneously strained crystals. The mapped Bloch functions $u^*_{n0}(\mathbf{x};\varepsilon)$ are written alongside.

reference unstrained crystal such that the rotation component of the displacement field is zero, which allow the displacement $\mathbf{u}(\mathbf{x})$ to be be written as $\mathbf{u}(\mathbf{x}) = \varepsilon\mathbf{x}$, namely $u_i = \varepsilon_{ik}x_k$. It then follows from Eq. 3.12 and Eq. 3.13 that the Schrödinger equation for homogeneously strained crystals transforms into undeformed coordinates as

$$\left[-\frac{1}{2}(I+\varepsilon)^{-1}_{im}(I+\varepsilon)^{-T}_{mj}\frac{\partial^2}{\partial x_i \partial x_j} + U^*(\mathbf{x};\varepsilon)\right]\Psi^* = E\Psi^*, \tag{3.16}$$

Here, to distinguish the crystal potential of homogeneously strained crystal from that of inhomogeneously strained crystal, we have used the symbol $U^*(\mathbf{x};\varepsilon)$ to represent the mapped crystal potential of homogeneously strained crystal with strain tensor $\varepsilon$. From now on, $U$ and $V$ will be used to represent the crystal potentials of homogeneously strained crystals and inhomogeneously strained crystals respectively.

Given a reference crystal momentum $\mathbf{k}_0$ for unstrained crystal, for each of the homogeneously strained crystal with strain tensor $\varepsilon$, their Bloch functions at the corresponding strained crystal momentum $\mathbf{k} = (I+\varepsilon)^{-T}\mathbf{k}_0$ can be written as

$$\psi_{n\mathbf{k}}(\mathbf{x}';\varepsilon) = e^{i\mathbf{k}\cdot\mathbf{x}'} u_{n\mathbf{k}}(\mathbf{x}';\varepsilon). \tag{3.17}$$

$\psi_{n\mathbf{k}}(\mathbf{x}';\varepsilon)$ can then be mapped back to undeformed coordinates and denoted by

$$\psi^*_{n\mathbf{k}_0}(\mathbf{x};\varepsilon) = e^{i\mathbf{k}_0\cdot\mathbf{x}} u^*_{n\mathbf{k}_0}(\mathbf{x};\varepsilon). \tag{3.18}$$

Without loss of generality, hereafter we chose the reference crystal momentum $\mathbf{k}_0 = 0$, in which case only the periodic part of the Bloch functions $u^*_{n0}(\mathbf{x};\varepsilon)$ will be retained.

For any value of strain $\varepsilon$, the mapped Bloch functions $u^*_{n0}(\mathbf{x};\varepsilon)$ are periodic functions of the original, undeformed lattice translation vectors. Therefore, each of them can be expanded in undeformed coordinates in terms of a complete and orthonormal basis set $\varphi_m(\mathbf{x})$, which for example can be plane waves:

$$u^*_{n0}(\mathbf{x};\varepsilon) = \sum_m C^n_m(\varepsilon)\varphi_m(\mathbf{x}). \tag{3.19}$$

The expansion coefficients $C^n_m(\varepsilon)$ will be dependent of the strain value $\varepsilon$. After this expansion, the strain $\varepsilon$ dependence of the Bloch functions $u^*_{n0}(\mathbf{x};\varepsilon)$ is separated into the expansion coefficients $C^n_m(\varepsilon)$. In the absence of strain-induced phase transition, and choosing the same gauge [100] for different strained Bloch functions, these expansion coefficients should be continuous functions of strain $\varepsilon$. We then can define a *strain-parametrized* basis set $u^*_{n0}(\mathbf{x};\varepsilon(\mathbf{x})) \equiv u^*_{n0}(\mathbf{x};\varepsilon=\varepsilon(\mathbf{x}))$, which means that at position $\mathbf{x}$, the values of the expansion coefficients $C^n_m$ in Eq. 3.19 take the values of $C^n_m(\varepsilon=\varepsilon(\mathbf{x}))$. Mathematically, this can be written out as

$$u^*_{n0}(\mathbf{x};\varepsilon(\mathbf{x})) = \sum_m C^n_m\left(\varepsilon(\mathbf{x})\right)\varphi_m(\mathbf{x}), \tag{3.20}$$

$u^*_{n0}(\mathbf{x};\varepsilon(\mathbf{x}))$ are named "strain-parametrized Bloch functions", since they are parametrized to the strain field $\varepsilon(\mathbf{x})$ in an inhomogeneous strained crystal. In analogy with the conventional envelope function method [77], we can use $u^*_{n0}(\mathbf{x};\varepsilon(\mathbf{x}))$ to expand the mapped global wavefunctions $\Psi^*(\mathbf{x})$ of inhomogeneously strained crystals,

$$\Psi^*(\mathbf{x}) = \sum_n F_n(\mathbf{x}) u^*_{n0}(\mathbf{x};\varepsilon(\mathbf{x})). \tag{3.21}$$

The summation is over the band index $n$, but will normally be truncated to include only bands within certain energy range of interest, as far-away bands have smaller contributions to the electronic states under consideration. Here, $F_n(\mathbf{x})$ are, as in conventional envelope function method, considered to be smooth functions on unit-cell scale. This envelope expansion is, in essence, a continuous generalization of Bastard's envelope expansion method for semiconductor heterostructures [78], where the wavefunctions in the barrier and well regions of heterostructures are expanded in the Bloch functions of respective region.

### 3.2.3 Local Approximation of Strained Crystal Potential and Envelope Function Equation

Our next natural step is to substitute $\Psi^*(\mathbf{x})$ into the mapped Schödinger equation for inhomogeneously strained crystal, the Eq. 3.12, which for convenience is rewritten here as

$$[\mathcal{P}^* + V^*(\mathbf{x})]\, \Psi^*(\mathbf{x}) = E\Psi^*(\mathbf{x}), \tag{3.22}$$

where $\mathcal{P}^*$ is an operator given by

$$\mathcal{P}^* = -\frac{1}{2}\left[a_{ij}(\mathbf{x})\frac{\partial^2}{\partial x_i \partial x_j} + b_i(\mathbf{x})\frac{\partial}{\partial x_i}\right]. \tag{3.23}$$

$a_{ij}(\mathbf{x})$ and $b_i(\mathbf{x})$ have been defined earlier. Replacing $\Psi^*(\mathbf{x})$ by the strain-parametrized envelope function expansion in Eq. 3.21, the above Schrödinger equation becomes

$$\sum_n \mathcal{P}^* \left[F_n(\mathbf{x})u^*_{n0}(\mathbf{x};\varepsilon(\mathbf{x}))\right] + \sum_n F_n(\mathbf{x}) \left[V^*(\mathbf{x})u^*_{n0}(\mathbf{x};\varepsilon(\mathbf{x}))\right] = E\sum_n F_n(\mathbf{x})u^*_{n0}(\mathbf{x};\varepsilon(\mathbf{x})). \tag{3.24}$$

The potential energy operator $V^*(\mathbf{x})$ is the unknown term in the Hamiltonian, which in *ab initio* calculation is determined self-consistently. As we have argued earlier, such self-consistent calculation of $V^*(\mathbf{x})$ is usually impractical for an inhomogeneously strained crystal due to the large system size. Hence, we introduce here an important approximation in our method: for a slowly-varying inhomogeneously strained semiconductor, the crystal potential $V^*(\mathbf{x})$ at position $\mathbf{x}$ can be well approximated by that of a homogeneously deformed crystal with same strain tensor $\varepsilon(\mathbf{x})$, if (a) the applied elastic strain field $\varepsilon(\mathbf{x})$ is sufficiently slowly-varying at atomic scale and (b) long-range electrostatic effects [101] are negligible. This locality principle for the electronic structure of insulators/semiconductors has been proved by E *et al* [96, 97, 98]. It is also implicitly implied in the treatment of strain in the EPM method [76].

Mathematically, the locality principle translates into

$$V^*(\mathbf{x}) = U^*(\mathbf{x}; \varepsilon(\mathbf{x})) + \mathcal{O}(b|\nabla\varepsilon(\mathbf{x})|), \tag{3.25}$$

where $U^*(\mathbf{x}; \varepsilon(\mathbf{x}))$ is the strain-parametrized crystal potential of homogeneously strained crystals, $b$ is the average magnitude of lattice constants, and $\nabla\varepsilon(\mathbf{x})$ is the gradient of strain field. $b|\nabla\varepsilon(\mathbf{x})|$ is thus a measure of how fast strain varies at atomic scale. Clearly, the smaller this measure, the better the locality approximation will be. In the case $\varepsilon(\mathbf{x})$ goes to zero, the approximation becomes exact. Since we are concerned with slowly-varying inhomogeneously strained crystals in this article, in what follows we will only keep the term $U^*(\mathbf{x}; \varepsilon(\mathbf{x}))$, which is the zeroth-order term in strain gradient, or the first-order term in displacement gradient.

Adopting this locality principle greatly facilitates the solution of the electronic structure problem, as we can now use the local electronic structure information of homogeneously deformed crystals, obtained from unit-cell level *ab initio* or semi-empirical calculations, to eliminate the unknown crystal potential term $V^*(\mathbf{x})$ in Eq. 3.24. Specifically, we can write down the local Schrödinger equation for the strain-parametrized expansion basis

$$[\mathcal{P}_0^* + U^*(\mathbf{x};\varepsilon(\mathbf{x}))]\, u_{n0}^*(\mathbf{x};\varepsilon(\mathbf{x})) = \epsilon_{n0}(\varepsilon(\mathbf{x}))\, u_{n0}^*(\mathbf{x};\varepsilon(\mathbf{x})), \tag{3.26}$$

with $\mathcal{P}_0^*$ being

$$\mathcal{P}_0^* = -\frac{1}{2}(I+\varepsilon(\mathbf{x}))_{im}^{-1}(I+\varepsilon(\mathbf{x}))_{mj}^{-T}\, \frac{\partial^2}{\partial x_i \partial x_j}\bigg|_{\varphi(\mathbf{x})}. \tag{3.27}$$

In Eq. 3.26, $\epsilon_{n0}(\varepsilon(\mathbf{x}))$ is the strain-parametrized energy eigenvalues for band $n$ at the reference crystal momentum, defined as $\epsilon_{n0}(\varepsilon(\mathbf{x})) \equiv \epsilon_{n0}(\varepsilon = \varepsilon(\mathbf{x}))$. The subscript $\varphi(\mathbf{x})$ in $\mathcal{P}_0^*$ denotes that, when the partial derivatives operate on the strain-parametrized expansion $u_{n0}^*(\mathbf{x};\varepsilon(\mathbf{x})) = \sum_m C_m^n\,(\varepsilon(\mathbf{x}))\,\varphi_m(\mathbf{x})$, they act on the position dependence coming from $\varphi(\mathbf{x})$, but not on the $\mathbf{x}$ dependence coming from $C_m^n(\varepsilon(\mathbf{x}))$. To better understand Eq. 3.26, one can look at the limit when the strain field $\varepsilon(\mathbf{x})$ is uniform throughout the crystal. Eq. 3.26 then simply becomes a normal Schrödinger equation for homogeneously strained crystal mapped to undeformed coordinates.

We will now use the local Schrödinger equation to eliminate the potential energy operator $V^*(\mathbf{x})$ in global Schrödinger equation. Rearranging Eq. 3.26, we have

$$U^*(\mathbf{x};\varepsilon(\mathbf{x}))u_{n0}^*(\mathbf{x};\varepsilon(\mathbf{x})) = [-\mathcal{P}_0^* + \epsilon_{n0}(\varepsilon(\mathbf{x}))]\, u_{n0}^*(\mathbf{x};\varepsilon(\mathbf{x})). \tag{3.28}$$

We then replace $V^*(\mathbf{x})$ in Eq. 3.24 by $U^*(\mathbf{x};\varepsilon(\mathbf{x}))$ based on the locality principle, and replace $U^*(\mathbf{x};\varepsilon(\mathbf{x}))u_{n0}^*(\mathbf{x};\varepsilon(\mathbf{x}))$ by the right-hand side of Eq. 3.28. Finally, we reach the following coupled differential equation for the envelope functions $F_n(\mathbf{x})$:

$$\begin{aligned}\sum_n \mathcal{P}^*\left[F_n(\mathbf{x})u_{n0}^*(\mathbf{x};\varepsilon(\mathbf{x}))\right] - \sum_n F_n(\mathbf{x})\mathcal{P}_0^*\left[u_{n0}^*(\mathbf{x};\varepsilon(\mathbf{x}))\right] \\ = \sum_n F_n(\mathbf{x})\left[E - \epsilon_{n0}(\varepsilon(\mathbf{x}))\right] u_{n0}^*(\mathbf{x};\varepsilon(\mathbf{x})).\end{aligned} \tag{3.29}$$

This coupled differential eigenvalue equation is the central equation we need to solve in our envelope function method. The unknowns in the equations are the global energy eigenvalues $E$ and their associated envelope functions $F_n(\mathbf{x})$. The strain-parametrized Bloch functions $u^*_{n0}(\mathbf{x};\varepsilon(\mathbf{x}))$ and their energy eigenvalues $\epsilon_{n0}(\varepsilon(\mathbf{x}))$, can be constructed using *ab inito* or semi-empirical calculation of homogeneously strained crystals at unit-cell level, using the procedures described in Sec. 3.2.2. The coupled differential equation can be solved numerically by expanding the envelope functions in an appropriate basis, and then turned into a matrix eigenvalue equation. The expansion basis can be judiciously chosen to reflect the symmetries that the envelope functions could have. The most general expansion basis, however, are plane waves:

$$F_n(\mathbf{x}) = \sum_{\mathbf{k}} B_{n\mathbf{k}} e^{-i\mathbf{k}\cdot\mathbf{x}}. \tag{3.30}$$

Plugging the above equation into Eq. 3.29, it will turn into the following equation

$$\begin{aligned}&\sum_n \sum_{\mathbf{k}} B_{n\mathbf{k}} \left\{\mathcal{P}^* \left[e^{i\mathbf{k}\cdot\mathbf{x}} u^*_{n0}(\mathbf{x};\varepsilon(\mathbf{x}))\right] - e^{i\mathbf{k}\cdot\mathbf{x}} \mathcal{P}^*_0 \left[u^*_{n0}(\mathbf{x};\varepsilon(\mathbf{x}))\right]\right\} \\ &= \sum_n \sum_{\mathbf{k}} B_{n\mathbf{k}} e^{i\mathbf{k}\cdot\mathbf{x}} \left(E - \epsilon_{n0}(\varepsilon(\mathbf{x}))\right) u^*_{n0}(\mathbf{x};\varepsilon(\mathbf{x})).\end{aligned} \tag{3.31}$$

We then multiply the both sides of Eq. 3.31 by $\left[e^{i\mathbf{k}'\cdot\mathbf{x}} u^*_{m0}(\mathbf{x};\varepsilon(\mathbf{x}))\right]^\dagger$ (dagger denotes complex conjugation), and then integrate both side over the whole crystal volume $V$. This results in $N \times M_{\mathbf{k}}$ independent linear equations, where $N$ is the number of bands included in the envelope function expansion in Eq. 3.21, $M_{\mathbf{k}}$ is the number of plane waves used to expand the envelope functions $F_n(\mathbf{x})$ in Eq. 3.30. The system of linear equations are written below as:

$$\sum_{n\mathbf{k}} B_{n\mathbf{k}} \left(W^{m\mathbf{k}'}_{n\mathbf{k}} - R^{m\mathbf{k}'}_{n\mathbf{k}} + S^{m\mathbf{k}'}_{n\mathbf{k}}\right) = E \sum_{n\mathbf{k}} B_{n\mathbf{k}} T^{m\mathbf{k}'}_{n\mathbf{k}}, \tag{3.32}$$

where

$$
\begin{aligned}
W_{n\mathbf{k}}^{m\mathbf{k}'} &= \int_V d\mathbf{x} \, \left[e^{i\mathbf{k}'\cdot\mathbf{x}} u_{m0}^*\right]^\dagger \mathcal{P}^* \left[e^{i\mathbf{k}\cdot\mathbf{x}} u_{n0}^*\right], \\
R_{n\mathbf{k}}^{m\mathbf{k}'} &= \int_V d\mathbf{x} \, e^{i(\mathbf{k}-\mathbf{k}')\cdot\mathbf{x}} (u_{m0}^*)^\dagger \mathcal{P}_0^* u_{n0}^*, \\
S_{n\mathbf{k}}^{m\mathbf{k}'} &= \int_V d\mathbf{x} \, e^{i(\mathbf{k}-\mathbf{k}')\cdot\mathbf{x}} (u_{m0}^*)^\dagger u_{n0}^*, \\
T_{n\mathbf{k}}^{m\mathbf{k}'} &= \int_V d\mathbf{x} \, e^{i(\mathbf{k}-\mathbf{k}')\cdot\mathbf{x}} \epsilon_{n0} \left(\varepsilon(\mathbf{x})\right) (u_{m0}^*)^\dagger u_{n0}^*.
\end{aligned}
$$

$u_{n0}^*$ is short for $u_{n0}^*(\mathbf{x};\varepsilon(\mathbf{x}))$. The system of linear equations can be solved numerically as a generalized eigenvector problem to obtain the eigenvalues $E$ and eigenvectors $B_{n\mathbf{k}}$.

## 3.3 Application to One-Dimensional Models

### 3.3.1 General Framework

To demonstrate the effectiveness of our envelope function method, we will apply the method to one-dimensional (1D) inhomogeneously strained crystals. We will first lay out the general mathematical framework of the method in 1D, followed by a specific example in the next section. Most equations in this section are just 1D special cases of equations in the previous section.

Suppose a slowly varying inhomogeneous strain $\varepsilon(x)$ is imposed on a 1D crystal. The strain field corresponds to a displacement field $u(x) = \int^x \varepsilon(x')dx'$. The operators $\mathcal{P}^*$ and $\mathcal{P}_0^*$ defined in the previous section will have the following form

$$
\mathcal{P}^* = -\frac{1}{2[1+\varepsilon(x)]^2}\frac{d^2}{dx^2} + \frac{\varepsilon'(x)}{2\left[1+\varepsilon(x)\right]^3}\frac{d}{dx}, \tag{3.33}
$$

$$
\mathcal{P}_0^* = -\frac{1}{2[1+\varepsilon(x)]^2}\frac{\partial^2}{\partial x^2}, \tag{3.34}
$$

where $\varepsilon'(x)$ denotes the derivative of strain with respect to $x$. The partial derivative in $\mathcal{P}_0^*$ implies that, for a strain parametrized function $f(x;\varepsilon(x))$, the derivative will not act on the $x$ dependence coming from $\varepsilon(x)$.

The Schrödinger equation mapped back to undeformed coordinates will be

$$[\mathcal{P}^* + V^*(x)]\,\Psi^*(x) = E\Psi^*(x), \tag{3.35}$$

where $V^*(x)$ and $\Psi^*(x)$ are mapped crystal potential and energy eigenfunction in undeformed coordinates. $E$ is energy eigenvalue. $\Psi^*(x)$ will be expanded in terms of envelope functions and strain-parametrized Bloch functions:

$$\Psi^*(x) = \sum_n F_n(x) u^*_{n0}(x; \varepsilon(x)) \tag{3.36}$$

The strain parametrized Bloch functions $u^*_{n0}(x; \varepsilon(x))$ satisfies the local Schrödinger equation for homogeneously strained crystal

$$[\mathcal{P}^*_0 + U^*(x; \varepsilon(x))]\, u^*_{n0}(x; \varepsilon(x)) = \epsilon_{n0}(\varepsilon(x)) u^*_{n0}(x; \varepsilon(x)). \tag{3.37}$$

We then adopt the local approximation of crystal potential $V^*(x) \approx U^*(x; \varepsilon(x))$, which allows us to use the above local Schrödinger equation to transform Eq. 3.35 into the following envelope function equation

$$\begin{aligned} &\sum_n \left\{\mathcal{P}^* \left[F_n(x) u^*_{n0}(x; \varepsilon(x))\right] - F_n(x)\mathcal{P}^*_0 \left[u^*_{n0}(x; \varepsilon(x))\right]\right\} \\ &\quad = \sum_n F_n(x) \left[E - \epsilon_{n0}(\varepsilon(x))\right] u^*_{n0}(x; \varepsilon(x)). \end{aligned} \tag{3.38}$$

Using the explicit forms of $\mathcal{P}^*$ and $\mathcal{P}^*_0$ in Eq. 3.33 and Eq. 3.34, the above equation can be further written as

$$\sum_n \left[p_n(x) F''_n + q_n(x) F'_n + g_n(x) F_n\right] = E \sum_n h_n(x) F_n, \tag{3.39}$$

with $p_n(x)$, $q_n(x)$, $g_n(x)$ and $h_n(x)$ given by

$$\begin{aligned} p_n(x) =& u^*_{n0}(x;\varepsilon(x)) \\ q_n(x) =& 2\frac{d}{dx}u^*_{n0}(x;\varepsilon(x)) - \frac{\varepsilon'(x)}{1+\varepsilon(x)}u^*_{n0}(x;\varepsilon(x)) \\ g_n(x) =& \frac{d^2}{dx^2}u^*_{n0}(x;\varepsilon(x)) - \frac{\partial^2}{\partial x^2}u^*_{n0}(x;\varepsilon(x)) - \frac{\varepsilon'(x)}{1+\varepsilon(x)}\frac{d}{dx}u^*_{n0}(x;\varepsilon(x)) \\ & - 2[1+\varepsilon(x)]^2\epsilon_{n0}(\varepsilon(x))u^*_{n0}(x;\varepsilon(x)) \\ h_n(x) =& -2[1+\varepsilon(x)]^2 u^*_{n0}(x;\varepsilon(x)). \end{aligned} \tag{3.40}$$

After constructing the strain parametrized Bloch functions $u^*_{n0}(x;\varepsilon(x))$ and $\epsilon_{n0}(\varepsilon(x))$ through unit-cell level calculations of homogeneously strained crystals and strain-parametrization, described in Sec. 3.2.2, the coupled differential eigenvalue equation Eq. 3.39 can be solved numerically using the method described in the previous section.

### 3.3.2 Example

Consider a 1D crystal with lattice constant $a_0$ and the following model crystal potential

$$U(x) = -U_0 \cos\left(\frac{4\pi}{a_0}x\right). \tag{3.41}$$

This crystal potential has the following attractive features:

(1) A direct bandgap of magnitude $E_g \approx U_0$ will open up between the second and third energy band at crystal momentum $k = 0$, as shown in Fig. 3-2. Assuming that the first and second band are completely filled by electrons while those bands above are empty, the 1D crystal corresponds to a direct bandgap semiconductor for which the second band ($n = 2$) is the "valence band" and the third band ($n = 3$) is the "conduction band". We will use this designation from now on. The bandgap is $E_g \equiv E_c - E_v \approx U_0$, where $E_c$ is the energy of the conduction band minimum, and $E_v$ is the energy of the valence band maximum.

(2) If we fix $U_0$, the value of bandgap $E_g$ will almost have no change even when the lattice constant $a_0$ is varied. The change of lattice constant $a_0$ is natural when we

apply strain $\varepsilon$ to the system, namely $a_0$ becomes $a_0(1+\varepsilon)$. While $E_g \equiv E_c - E_v \approx U_0$ does not change when lattice constant $a_0$ is changed, the absolute energy values of the conduction band edge $E_c$ and valence band edge $E_v$, however, do shift, mainly due to the change of kinetic energies for electrons in the system when enlarging or shrinking the crystal. we can therefore model the strain-induced energy level shifting without incurring bandgap change in this model crystal potential.

(3) If we want to model bandgap change when strain is applied, we can simply write $U_0$ as a function of strain $\varepsilon$. For example, to model the linear change of bandgap as a function of strain, we can write $U_0(\varepsilon) = U_0 + K\varepsilon$, where $K$ denotes the rate of bandgap change as a function of strain.

Hence, the 1D crystal potential is an excellent model system for 1D semiconductor, whose band edge energy levels $(E_c, E_v)$ and bandgap $E_g$ can be independently tuned. The crystal potential can therefore model deformation potential [87] while being mathematically simple and transparent.

In the spirit of the above discussion, we now assume that, after applying homogeneous strain $\varepsilon$ to the model 1D semiconductor, its crystal potential has the following form:

$$U(x';\varepsilon) = -(U_0 + K\varepsilon)\cos\left[\frac{4\pi}{a_0(1+\varepsilon)}x'\right]. \tag{3.42}$$

This implies that both the energy levels and bandgap of the 1D crystal will change after applying strain. Comparison of the band-structures of the 1D crystal before and after deformation for a specific set of parameters $U_0 = 0.2$, $K = -0.5$, and $\varepsilon = 0.05$ is shown in Fig. 3-2.

The crystal potential of homogeneously strained 1D crystal, $U(x';\varepsilon)$, is up to now defined in strained coordinates $x'$. As discussed earlier, we can map the strained crystal potential back to undeformed coordinates $x$ based the mapping relationship $x' = x + u(x) = (1+\varepsilon)x$. The mapped crystal potential becomes the following

$$U^*(x;\varepsilon) = -(U_0 + K\varepsilon)\cos(4\pi x/a_0). \tag{3.43}$$

Suppose now a continuous strain distribution $\varepsilon(x)$ is defined in the $x$ coordinates.

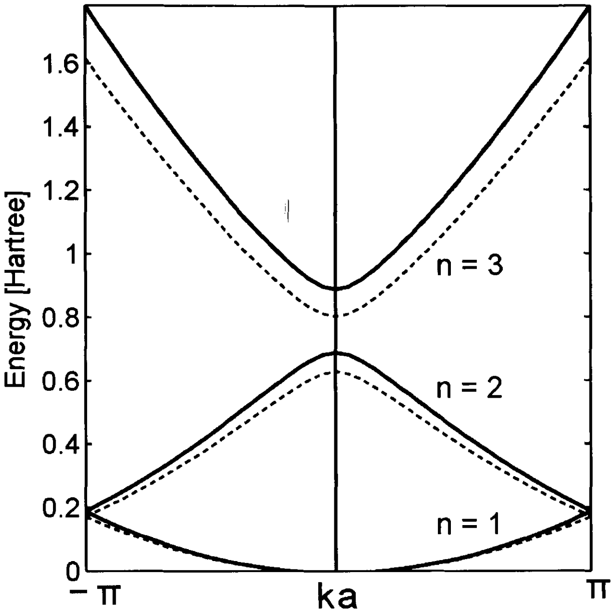

Figure 3-2: Calculated energy band structure of the model 1D crystal before and after applying homogeneous strain (see main text for details of the 1D crystal). Only the first three bands are presented. Solid and dashed line denote the first three energy bands of unstrained crystal and homogeneously strained crystal with $\varepsilon = 0.05$, respectively. The axis label $ka$ denotes the product of crystal momentum $k$ and lattice constant $a = a_0(1+\varepsilon)$.

We can define a strain-parametrized crystal potential $U^*(x;\varepsilon(x))$ such that at position $x$, we first calculate the strain $\varepsilon(x)$ at $x$, then assign $U^*(x;\varepsilon(x))$ a value equal to $U^*(x;\varepsilon=\varepsilon(x))$. Namely,

$$\begin{aligned} U^*(x;\varepsilon(x)) &\equiv U^*(x;\varepsilon=\varepsilon(x)) \\ &= -(U_0 + K\varepsilon(x))\cos(4\pi x/a_0). \end{aligned} \tag{3.44}$$

With the above model set-up, we now apply a Gaussian-type inhomogeneous strain on the 1D crystal. The strain distribution is given by

$$\varepsilon(x) = \varepsilon_{\max} \exp\left[-\frac{(x-L/2)^2}{(L/4)^2}\right], \tag{3.45}$$

where $\varepsilon_{\max}$ is the maximum strain value in the strain field $\varepsilon(x)$, occurring at $x = L/2$.

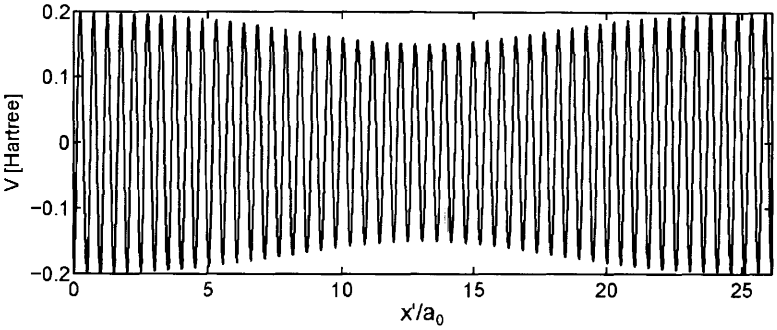

Figure 3-3: Potential of the model 1D crystal after applying Gaussian-type inhomogeneous strain. $V(x') = U^*(x;\varepsilon(x)) = -\left[U_0 + K\varepsilon(x)\right]\cos(4\pi x/a_0)$. $x$ is related to $x'$ via $x' = x + \frac{\sqrt{\pi}L}{8}\varepsilon_{\max}\left[\operatorname{erf}\left(\frac{x-L/2}{L/4}\right) - \operatorname{erf}(-2)\right]$. The values of model parameters $U_0$, $K$, $L$ and $\varepsilon_{\max}$ are given by $U_0 = 0.2$, $K = -0.5$, $L = 25a_0$ and $\varepsilon_{\max} = 0.1$.

$L$ denotes the size of crystal. After applying the inhomogeneous strain, a position $x$ in the undeformed crystal will map to a new position $x'$ in deformed coordinates given by

$$\begin{aligned} x' &= x + \int_0^x \varepsilon(v)dv \\ &= x + \frac{\sqrt{\pi}L}{8}\varepsilon_{\max}\left[\operatorname{erf}\left(\frac{x-L/2}{L/4}\right) - \operatorname{erf}(-2)\right], \end{aligned} \tag{3.46}$$

where $\operatorname{erf}(x)$ denotes error function.

Denote by $V(x')$ the crystal potential of the 1D crystal after applying the Gaussian inhomogeneous strain, we then adopt the local approximation of crystal potential as described in Sec. 3.2.3, which says that the inhomogeneously strained crystal potential at point $x'$ can be well approximated by the crystal potential of a homogeneously strained crystal with the same strain value. This can be mathematically written out as

$$V(x') \approx U^*(x;\varepsilon(x)), \quad x' = x + \int_0^x \varepsilon(v)dv. \tag{3.47}$$

The as-constructed strained crystal potential $V(x')$ is visualized in Fig. 5-3.

We have thus, for demonstration purpose, explicitly constructed the strained crystal potential $V(x')$ using the local approximation of crystal potential. This allows us to solve the energy eigenstates of an inhomogeneously strained crystal using two distinct methods:

Method 1: direct numerical diagonalization of strained Hamiltonian. Since the explicit expression for the inhomogeneously strained crystal potential $V(x')$ has been constructed, we can solve the Schrödinger equation for the inhomogeneously strained crystal in deformed coordinates,

$$\left[-\frac{1}{2}\frac{d^2}{dx'^2}+V(x')\right]\Psi(x')=E\Psi(x'), \tag{3.48}$$

by diagonalizing the Hamiltonian $H=-\frac{1}{2}\frac{d^2}{dx'^2}+V(x')$ using plane wave basis set in Fourier space. More straightforwardly, we can discretize the wavefunction $\Psi(x')$ into a $N\times 1$ matrix vector in real space,

$$\Psi(x')=\begin{bmatrix}\Psi(x'_1) & \Psi(x'_2) & \cdots & \Psi(x'_N)\end{bmatrix}^T, \tag{3.49}$$

and then write the Hamiltonian as a matrix operator $\mathbf{H}$ acting on the wavefunction $\mathbf{H}=-\mathbf{L}/2+\mathbf{V}$, where $\mathbf{L}$ and $\mathbf{V}$ are the matrix operators for the differential operator $\frac{d^2}{dx'^2}$ and the potential operator $V(x')$ respectively:

$$\mathbf{L}=\frac{1}{(\Delta x')^2}\begin{bmatrix}-2 & 1 & & 1\\ 1 & -2 & 1 & \\ & 1 & \ddots & 1\\ 1 & & 1 & -2\end{bmatrix}, \tag{3.50}$$

$$\mathbf{V}=\begin{bmatrix}V(x'_1) & & & \\ & V(x'_2) & & \\ & & \ddots & \\ & & & V(x'_N)\end{bmatrix}. \tag{3.51}$$

$\Delta x'=x'_{i+1}-x'_i$ is the distance between two real space grid points. The Hamiltonian matrix $\mathbf{H}$ can then be numerically diagonalized to obtain the energy eigenvalues $E$ and wavefunctions $\Psi(x')$.

Method 2: solving the energy eigenstates of inhomogeneously strained crystal using our envelope function method. We can solve the Schrödinger equation, Eq. 3.48, by first mapping it back to undeformed coordinates, which becomes

$$[\mathcal{P}^* + U^*(x; \varepsilon(x))]\, \Psi^*(x) = E\Psi^*(x). \tag{3.52}$$

The explicit expression for the differential operator $\mathcal{P}^*$ is given by Eq. 3.33. The mapped wavefunctions $\Psi^*(x)$ will then be expressed in terms of envelope functions $F_n(x)$ and strain-parametrized Bloch functions $u^*_{n0}(x; \varepsilon(x))$:

$$\Psi^*(x) = \sum_n F_n(x) u^*_{n0}(x; \varepsilon(x)). \tag{3.53}$$

We then follow the procedures described in Sec. 3.3.1 to eliminate the crystal potential term $U^*(x; \varepsilon(x))$ in Eq. 3.52 using strain-parametrized Bloch functions $u^*_{n0}(x; \varepsilon(x))$ and the associated strain-parametrized energy eigenvalues $\epsilon(x; \varepsilon(x))$. Eq. 3.52 can then be turned into a coupled differential eigenvalue equation for the envelope functions $F_n(x)$ given by Eq. 3.39, and solved as a generalized matrix eigenvector problem.

The solution of Eq. 3.39 requires the explicit construction of strain-parametrized functions $u^*_{n0}(x; \varepsilon(x))$ and the associated strain-parametrized energy eigenvalues $\epsilon(x; \varepsilon(x))$. The construction of these functions involves unit-cell level calculations of homogeneously strained 1D crystals. Only the Bloch functions and energy eigenvalues of the electronic states at the reference crystal momentum ($k = 0$ in this case) and a few bands close to the valence/conduction band need to be calculated. The homogeneous strain values $\varepsilon$ are coarsely taken from the inhomogeneous strain field (no more than one grid point per unit cell). The calculated periodic Bloch functions of each homogeneously strained crystal are then expressed in plane wave basis as $u^*_{n0}(x; \varepsilon) = \sum_m C^n_m(\varepsilon) e^{i2\pi m x/a_0}$, where $C^n_m(\varepsilon)$ are the expansion coefficients. The strain-parametrized Bloch functions can then be constructed by letting $\varepsilon = \varepsilon(x)$ at position $x$, namely

$$u^*_{n0}(x; \varepsilon(x)) = \sum_m C^n_m(\varepsilon(x)) e^{i2\pi m x/a_0}. \tag{3.54}$$

It is easy to see that, at position $x$, the value of $u^*_{n0}(x; \varepsilon(x))$ is the same as the value of periodic Bloch function $u_{n0}^*(x;\varepsilon)$ at $x$ and $\varepsilon = \varepsilon(x)$. It is in this sense $u_{n0}^*(x;\varepsilon(x))$ are named strain-parametrized functions. Since $C_m^n(\varepsilon)$ are smooth functions of $\varepsilon$ and $\varepsilon(x)$ is a smooth function of $x$, we can use polynomial fitting to obtain smooth functions for $C_m^n(\varepsilon(x))$. As only unit-cell level calculations of homogeneously strained crystals at a reference crystal momentum are involved, the construction of the strain-parametrized functions $u_{n0}^*(x;\varepsilon(x))$ and $\epsilon(x;\varepsilon(x))$ do not require much computational power in this 1D example.

Of the two methods discussed above, Method 1, the direct diagonalization of Hamiltonian, is a well established method, therefore it can be used to benchmark Method 2, our envelope function method. To test the effectiveness of our envelope function method, we have calculated the energy eigenvalues and eigenfunctions of the 1D inhomogeneously strained crystal using both methods. A special note is that we are not testing here how good the local approximation of crystal potential for inhomogeneously strained crystal can be, but how accurate and fast our envelope function method can achieve given the local approximation of crystal potential is a sufficiently good approximation. Also note that, although for the sake of benchmarking our envelope function method, we have explicitly constructed the strained crystal potential in this 1D problem, in practical application of our envelope function method, such explicit construction of crystal potential will not be performed. The information of local strained crystal potential, at the level of approximation used in our method, is reflected in the strain-parametrized Bloch functions $u_{n0}^*(x;\varepsilon(x))$ and the associated strain-parametrized energy eigenvalues $\epsilon_{n0}(x;\varepsilon(x))$.

Choosing the following model parameters $L = 100a_0$, $U_0 = 0.2$, $K = -0.5$, and $\varepsilon_{\max} = 0.1$ for the 1D inhomogeneously strained crystal, we carry out numerical real space diagonalization of the Hamiltonian by spatially discretizing the wavefunction $\Psi(x)$ into a $N \times 1$ matrix. Periodic boundary condition $\Psi(0) = \Psi(L)$ is adopted. As the wavefunction oscillates rapidly even within a unit cell, very large $N$, around 50 times the number of unit cell $L/a_0$, is needed to achieve convergence of energy eigenvalues near valence or conduction band edge.

Fig. 3-4a shows the direct-diagonalization obtained energy eigenvalues near the

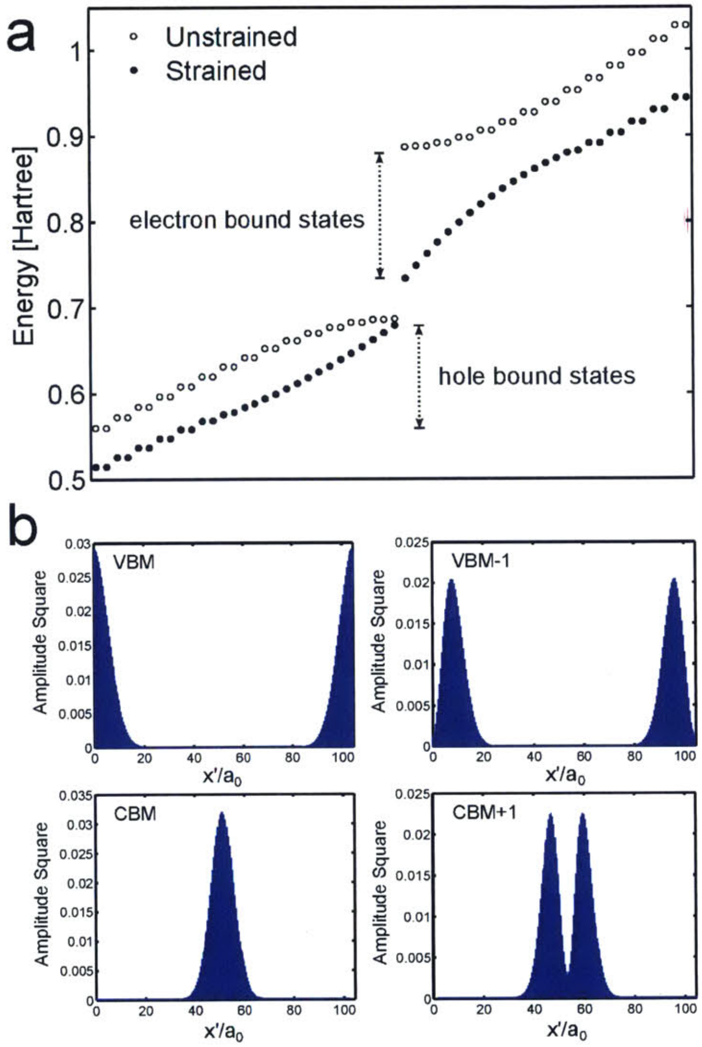

Figure 3-4: (a) Energy eigenvalues of the unstrained (open circles) and inhomogeneously strained model 1D crystal (filled circles) obtained by direct diagonalization. The energy levels are shifted horizontally with respect to each other to resolve energy levels which are very close to each other. The energy range of hole and electron bound states in strained crystals are labeled. (b) Wavefunction probability amplitude for hole and electron bound states, which are labeled in the figure as VBM, VBM-1, CBM, and CBM+1. VBM denotes valence band maximum; VBM-1 denotes one energy level below VBM; CBM means conduction band minimum, while CBM+1 denotes one energy level above CBM. The wavefunctions have rapid oscillation.

band edges. A 5000 × 5000 Hamiltonian matrix is involved in the numerical calculation. For comparison, the energy eigenvalues of unstrained crystal are shown together in the figure. The most distinct feature for the energy spectrum of inhomogeneously

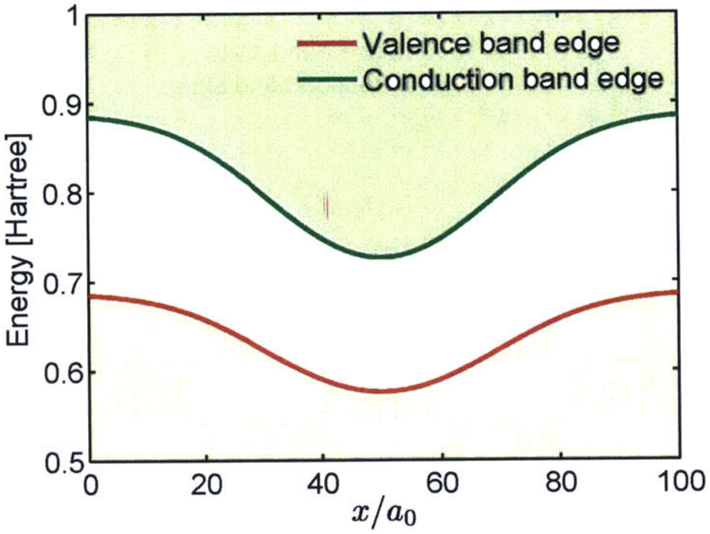

Figure 3-5: Valence and conduction band edge plotted as a function of position in the inhomogeneously strained crystal. The local band edges are calculated from homogeneously strained crystal with the same strain magnitude at position $x$.

strained crystal is the appearance of bound states near the conduction and valence band edges. These bound states, whose wavefunctions are shown in Fig. 3-4b, can be understood by plotting the local valence and conduction band edges as a function of position in the strained crystal, which is shown in Fig. 3-5. The alignment of band edges is reminiscent of semiconductor quantum well, except that in our case, the spatial variation of band-edge is smooth and extended, while in semiconductor quantum well, band edge usually jumps abruptly at the interface between the barrier and well region of quantum well. Hence, the strain-confined bound states in inhomogeneously strained crystal bear resemblance to bound states in quantum well. We want to emphasize that, the band edge alignment in our 1D inhomogeneously strained crystal is not unique to this model. Strain-induced band edge shift in semiconductor is a well-known phenomenon [87]. In fact, the band-edge alignment in our 1D model is similar to those calculated by Feng *et al* for inhomogeneously strained $MoS_2$ monolayer [71]. We can therefore conclude that the existence of electron or hole bound states is a general feature in an inhomogeneously strained crystal.

We have also calculated the energy eigenvalues using our envelope function method.

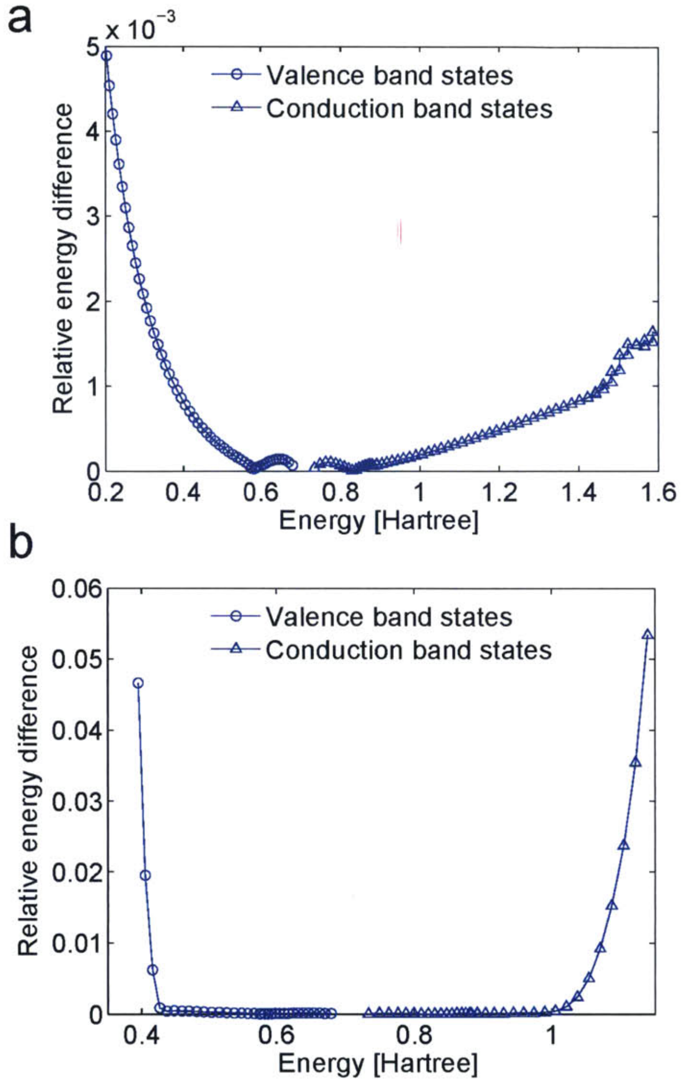

Figure 3-6: Relative difference of energy eigenvalues obtained by direct diagonalization and envelope function method. The energy eigenvalues from direct diagonalization of a 5000 by 5000 Hamiltonian matrix are served as reference to calculate the relative difference. In (a), zone-center Bloch functions of the lowest five bands are used to carry out envelope function expansion. The envelope functions are represented numerically using one mesh grid every unit cell. This leads to the diagonalization of an approximately 500 by 500 matrix. In (b), only valence and conduction bands zone-center Bloch functions are involved in envelope function expansion. The envelope functions are represented using one mesh grid every four unit cells. The resulting matrix for diagonalization is of order 50 by 50.

As shown in Fig. 3-6a, very high accuracy of eigenvalues is achieved for the whole valence and conduction bands using only one mesh grid per unit cell representation of the envelope functions. The lowest five bands are included in the summation over bands in the envelope function expansion (Eq. 3.53). Together, the envelope function method involves the diagonalization of an approximately 500 by 500 matrix, which is an order of magnitude smaller than direct diagonalization. As zone-center Bloch functions are used to carry out envelope function expansion, naturally the error for energy eigenvalues near the band edge is smaller, same as in conventional envelope function method. Furthermore, if one is only concerned with energy levels near the band edge, which in most practical application is true, the expense of envelope function method can be reduced by another order of magnitude by including only the most relevant bands, and using coarser grids for numerical representation of the envelope functions. In Fig. 3-6b, we show that more than 1/4 of energy levels in valence and conduction bands can be calculated with very high accuracy by including only the valence and conduction bands in wavefunction expansion, and using one mesh grid every four unit cells to represent the envelope functions. In this case, one ends up diagonalizing a 50 by 50 matrix, which is two order of magnitude smaller than direct diagonalization. Indeed, for this 1D model, our envelop function method is much faster than the direct diagonalization method.

The success of the envelope function method is because the envelope functions $F_n(x)$ are indeed slowly varying as we conjectured. Fig. 5-7 shows the amplitude square plot of envelope functions for a few electron and hole bound states. For the electron bound states, the envelope function of conduction band is predominant, while the valence band envelope function also contributes. The opposite is true for the hole bound states. Other remote bands have negligible contribution and are therefore not plotted. Comparing with the full wavefunctions calculated from direct diagonalization in Fig. 3-4b, one can notice that the envelope functions are indeed slowly-varying functions modulating the amplitude of fast-varying Bloch functions.

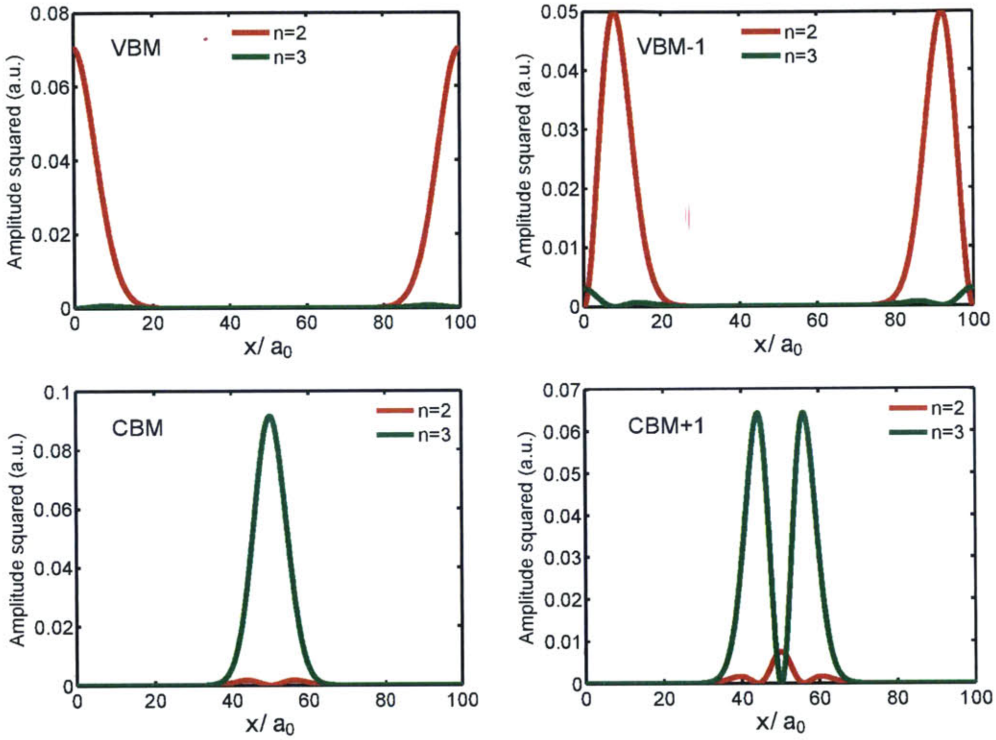

Figure 3-7: Amplitude squared plot of envelope functions $F_n(x)$ for states near valence and conduction band edges. The electronic states plotted are VBM, VBM+1, CBM and CBM−1. For these band edge states, only valence band ($n = 2$) and conduction band ($n = 3$) have significant envelope function amplitudes.

## 3.4 Toward Application to Three-Dimensional Real Materials

We have demonstrated in the previous section that our envelope function method can be successfully applied to a model 1D slowly-varying inhomogeneously strained semiconductor. A real semiconductor, however, is a three-dimensional (3D) object, and its crystal potential and strain response will be more complicated than the 1D model. Therefore, in this section we discuss some of the issues that may arise when applying our method to real 3D semiconductor crystals.

The procedures to carry out our envelope function method in 3D are essentially the same as in 1D, which we summarize in the flow chart of Fig. 3-8.

The first step in the flow chart is the determination of a smooth displacement field

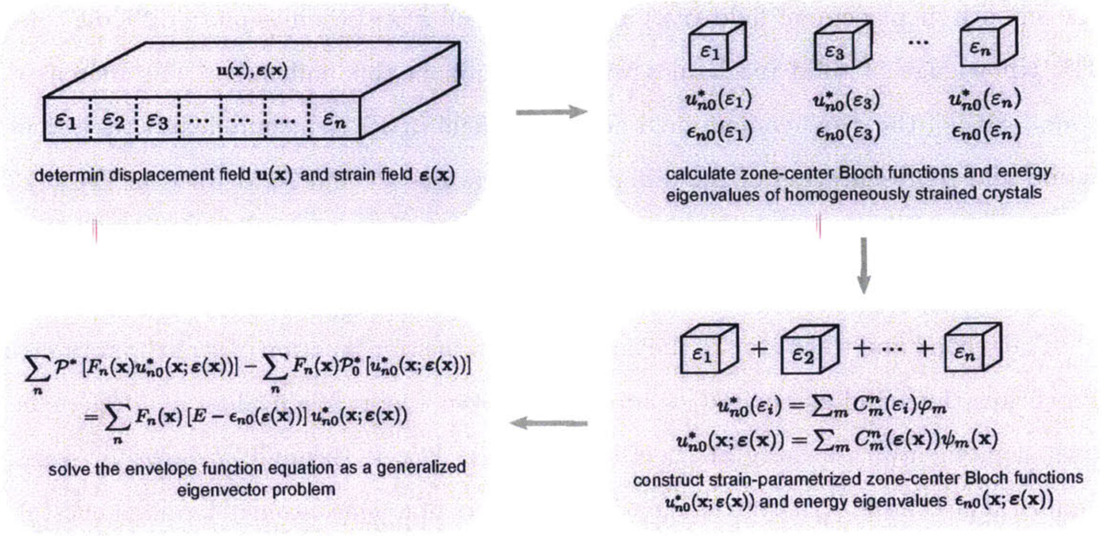

Figure 3-8: Flow chart to implement the envelope function method described in this article. The first step is the determination of a smooth displacement field $\mathbf{u}(\mathbf{x})$ which can map the unstrained crystal (and the associated vacuum space, if any) to the strained crystal. The strain field $\varepsilon(\mathbf{x})$ can be calculated from the displacement field $\mathbf{u}(\mathbf{x})$. The second and third steps are construction of strain-parametrized Bloch functions and energy eigenvalues at the reference crystal momentum (usually Brillouin zone center), through *ab initio* or semi-empirical electronic structure calculations of a series of homogeneously strained crystal, using strain values taken from the inhomogeneously strained crystal. The last step is the solution of the coupled differential equation for the envelope functions as a generalized matrix eigenvector problem.

$\mathbf{u}(\mathbf{x})$ which can map the unstrained crystal (and the associated vacuum space, if any) to the strained crystal. The corresponding strain field $\varepsilon(\mathbf{x})$ needs to be calculated as well. In 1D, displacement field $u(x)$ is a one-dimensional function and contains no rotational component. Thus $u(x)$ is related to the strain field $\varepsilon(x)$ via a simple integral relation $u(x) = \int^x \varepsilon(v)dv$. In 3D, the displacement field $\mathbf{u}(\mathbf{x})$ is three-dimensional, and the strain field $\boldsymbol{\varepsilon}(\mathbf{x})$ is a tensor field with six independent components. Due to the possible existence of rotational components, the components of the strain field are related to the displacement field $\mathbf{u}(\mathbf{x})$ (in the small deformation limit) as:

$$\varepsilon_{ij} = \frac{1}{2}\left(\frac{\partial u_i}{\partial x_j} + \frac{\partial u_j}{\partial x_i}\right) \tag{3.55}$$

Hence, for a generic 3D inhomogeneously strained crystal, finding and representing the smooth displacement field $\mathbf{u}(\mathbf{x})$ and strain field $\varepsilon(\mathbf{x})$ becomes more difficult than 1D. Knowledge of solid mechanics will be helpful in this endeavor. The increased complexity of the displacement field and strain field in 3D also complicates the calculation and representation of the differential operators $\mathcal{P}^*$ and $\mathcal{P}_0^*$ defined in Eq. 3.23 and Eq. 3.27, which need to be determined in order to solve the envelope function equation, Eq. 3.29.

The second and third step in the flow chart are the construction of strain-parametrized Bloch functions and associated strain-parametrized energy eigenvalues at a reference crystal momentum, usually at the Brillouin zone center, through *ab initio* or semi-empirical electronic structure calculation of a series of *homogeneously* strained crystal. The strain values are coarsely taken from the inhomogeneous strain field $\varepsilon$, which in principle is sufficient as the strain field is slowly-varying in space. Nevertheless, in a generic 3D case this step will be challenging as the number of calculations for homogeneously strained crystal can become quite large if the strain field is complex, as there are six independent components of strain tensor in 3D. The construction of strain-parameterized Bloch functions, described in Sec. 3.2.2, might also become non-trivial due to the complexity of electronic wavefunctions in 3D. Proper choice of expansion basis $\varphi_m(\mathbf{x})$ for the Bloch functions in Eq. 3.19 and Eq. 3.20 will be essential.

The fourth step in the flow chart is the solution of coupled differential equation for the envelope functions, the Eq. 3.29. This step, having been discussed in Sec. 3.2.3, should be straightforward once the differential operators $\mathcal{P}^*$ and $\mathcal{P}_0^*$, strain parameterized Bloch functions $u_{n0}^*(\mathbf{x}; \varepsilon(\mathbf{x}))$ and the associated strain parameterized energy eigenvalues $\epsilon_{n0}(\varepsilon(\mathbf{x}))$ have all been determined in the previous steps. Nevertheless, the computational cost of solving the differential eigenvalue equation will become larger as the dimensionality of the problem increases, as more spatial or Fourier grids will be needed to represent the envelope functions $F_n(\mathbf{x})$, resulting in larger matrices for numerical diagonalization.

In summary, the application of our envelope function method to a generic 3D problem will be feasible but challenging. We therefore believe that our method will most likely find applications in cases where the 3D problem is quasi-1D or 2D, namely when only one or very few components of the strain tensor is varying slowly in space.

We also comment here a few issues related to the central approximation adopted in our method, the local approximation of crystal potential in strained crystal elaborated in Sec. 3.2.3. The approximation states that in a slowly-varying inhomogeneously strained semiconductor or insulator, the local crystal potential $V(\mathbf{x}')$ can be well approximated by that of a homogeneously strained crystal with the same strain tensor $\varepsilon(\mathbf{x}')$. This local approximation of strained crystal potential is likely to be a good approximation only for non-polar semiconductors such as silicon and germanium. For polar semiconductors such as gallium arsenide, strain could induce piezoelectric effect, which generates long-range electric field in the deformed crystal and significantly increases the error of this approximation. Furthermore, we note that for certain materials with more than one atoms within a unit cell, strain can induce internal relaxation of atoms relative to each other on top of the displacement described by strain tensor, an effect not included in our present method and must be carefully checked in realistic calculations.

## 3.5 Envelope Function Equation for Empirical Applications

In this section, we will cast the envelope function equation (Eq. 3.29) in a new form in which the strain-parametrized Bloch functions $u^*_{n0}(\mathbf{x};\varepsilon(\mathbf{x}))$ will not appear explicitly. They will be replaced by a set of matrix elements involving their integrals. Doing so allows the method to be used empirically, where the matrix elements can be fitted to experimental data. The connection to traditional $\mathbf{k}\cdot\mathbf{p}$ envelope function method will also become clearer. For convenience, we rewrite the relevant equations below

$$\begin{aligned}&\sum_n \mathcal{P}^*\left[F_n(\mathbf{x})u^*_{n0}(\mathbf{x};\varepsilon(\mathbf{x}))\right] - \sum_n F_n(\mathbf{x})\mathcal{P}^*_0\left[u^*_{n0}(\mathbf{x};\varepsilon(\mathbf{x}))\right]\\ &= \sum_n F_n(\mathbf{x})\left[E-\epsilon_{n0}(\varepsilon(\mathbf{x}))\right]u^*_{n0}(\mathbf{x};\varepsilon(\mathbf{x})),\end{aligned} \tag{3.56}$$

where

$$\mathcal{P}^* = -\frac{1}{2}a_{ij}(\mathbf{x})\frac{\partial^2}{\partial x_i \partial x_j} - \frac{1}{2}b_i(\mathbf{x})\frac{\partial}{\partial x_i}, \tag{3.57}$$

$$\mathcal{P}_0^* = -\frac{1}{2}(I+\varepsilon(\mathbf{x}))^{-1}_{im}(I+\varepsilon(\mathbf{x}))^{-T}_{mj}\left.\frac{\partial^2}{\partial x_i \partial x_j}\right|_{\varphi(\mathbf{x})}. \tag{3.58}$$

$a_{ij}(\mathbf{x})$ and $b_i(\mathbf{x})$ are given by

$$a_{ij}(\mathbf{x}) = (I+\nabla\mathbf{u}(\mathbf{x}))^{-1}_{im}(I+\nabla\mathbf{u}(\mathbf{x}))^{-T}_{mj}, \tag{3.59}$$

$$b_i(\mathbf{x}) = (I+\nabla\mathbf{u}(\mathbf{x}))^{-1}_{nm}\frac{\partial}{\partial x_n}(I+\nabla\mathbf{u}(\mathbf{x}))^{-T}_{mi}. \tag{3.60}$$

$\mathcal{P}^*\left[F_n(\mathbf{x})u^*_{n0}(\mathbf{x};\varepsilon(\mathbf{x}))\right]$ can be expanded out as

$$\begin{aligned}\mathcal{P}^*[F_n(\mathbf{x})u^*_{n0}(\mathbf{x};\varepsilon(\mathbf{x}))] =& [\mathcal{P}^*F_n(\mathbf{x})]u^*_{n0}(\mathbf{x};\varepsilon(\mathbf{x})) + F_n(\mathbf{x})[\mathcal{P}^*u^*_{n0}(\mathbf{x};\varepsilon(\mathbf{x}))]\\ &- a_{ij}(\mathbf{x})\frac{\partial F_n(\mathbf{x})}{\partial x_i}\frac{\partial}{\partial x_j}u^*_{n0}(\mathbf{x};\varepsilon(\mathbf{x})).\end{aligned} \tag{3.61}$$

In above expansion, we have used the symmetry property of $a_{ij}(\mathbf{x})$, namely $a_{ij}(\mathbf{x}) = a_{ji}(\mathbf{x})$.

When strain variation $\varepsilon(\mathbf{x})$ is varying slowly at atomic scale, which is the premise of our envelope function method, the strain-parametrized basis functions $u^*_{n0}(\mathbf{x};\varepsilon(\mathbf{x}))$ for different bands $n$ are approximately independent and orthogonal:

$$\frac{1}{V}\int d\mathbf{x}\ J(\mathbf{x})\left[u^*_{n0}(\mathbf{x};\varepsilon(\mathbf{x}))\right]^\dagger u^*_{m0}(\mathbf{x};\varepsilon(\mathbf{x})) \approx \delta_{mn}. \tag{3.62}$$

The integration is over the whole crystal, whose volume is $V$. The Jacobian of deformation map $J(\mathbf{x}) = \det(I+\nabla\mathbf{u})$ takes into account the change of volume elements during coordinate transformation. We also note that, $J(\mathbf{x})$ can be absorbed into the basis functions by re-defining $u^*_{n0}(\mathbf{x};\varepsilon(\mathbf{x}))$ as $J(\mathbf{x})^{1/2}u^*_{n0}(\mathbf{x};\varepsilon(\mathbf{x}))$, and the whole formalism of our envelope function method will not change. This can be sometimes be more convenient for constructing strain-parametrized basis set.

Using the above orthonormal relation, we can express $\mathcal{P}^*\left[u^*_{n0}(\mathbf{x};\varepsilon(\mathbf{x}))\right]$, $\mathcal{P}_0^*\left[u^*_{n0}(\mathbf{x};\varepsilon(\mathbf{x}))\right]$, and $\frac{\partial}{\partial x_i} u^*_{n0}(\mathbf{x};\varepsilon(\mathbf{x}))$ in terms of $u^*_{n0}(\mathbf{x};\varepsilon(\mathbf{x}))$ as

$$
\begin{aligned}
\mathcal{P}^*\left[u^*_{n0}(\mathbf{x};\varepsilon(\mathbf{x}))\right] &= \sum_{n'} P_{nn'} u^*_{n'0}(\mathbf{x};\varepsilon(\mathbf{x})),\\
\mathcal{P}^*_0\left[u^*_{n0}(\mathbf{x};\varepsilon(\mathbf{x}))\right] &= \sum_{n'} P^0_{nn'} u^*_{n'0}(\mathbf{x};\varepsilon(\mathbf{x})),\\
\frac{\partial}{\partial x_i} u^*_{n0}(\mathbf{x};\varepsilon(\mathbf{x})) &= \sum_{n'} Q^i_{nn'} u^*_{n'0}(\mathbf{x};\varepsilon(\mathbf{x})),
\end{aligned}
$$

where $P_{nn'}$, $P^0_{nn'}$ and $Q^i_{nn'}$ are matrix elements given by

$$
\begin{aligned}
P_{nn'} &= \frac{1}{V}\int d\mathbf{x}\ J(\mathbf{x})\left\{\mathcal{P}^*\left[u^*_{n0}(\mathbf{x};\varepsilon(\mathbf{x}))\right]\right\}\left[u^*_{n'0}(\mathbf{x};\varepsilon(\mathbf{x}))\right]^\dagger,\\
P^0_{nn'} &= \frac{1}{V}\int d\mathbf{x}\ J(\mathbf{x})\left\{\mathcal{P}^*_0\left[u^*_{n0}(\mathbf{x};\varepsilon(\mathbf{x}))\right]\right\}\left[u^*_{n'0}(\mathbf{x};\varepsilon(\mathbf{x}))\right]^\dagger,\\
Q^i_{nn'} &= \frac{1}{V}\int d\mathbf{x}\ J(\mathbf{x})\left\{\frac{\partial}{\partial x_i} u^*_{n0}(\mathbf{x};\varepsilon(\mathbf{x}))\right\}\left[u^*_{n'0}(\mathbf{x};\varepsilon(\mathbf{x}))\right]^\dagger.
\end{aligned}
$$

Eq. 3.56 can now be written in terms of $u^*_{n0}(\mathbf{x};\varepsilon(\mathbf{x}))$ as

$$
\begin{aligned}
&\sum_n \left\{\mathcal{P}^* F_n - \sum_{n'} a_{ij}(\mathbf{x}) Q^i_{n'n} \frac{\partial F_{n'}}{\partial x_j} + \sum_{n'} (P_{n'n} - P^0_{n'n}) F_{n'}\right\} u^*_{n0}\\
&= \sum_n F_n(\mathbf{x})\left[E - \epsilon_{n0}(\varepsilon(\mathbf{x}))\right] u^*_{n0}.
\end{aligned}
\tag{3.63}
$$

Equating coefficients of $u^*_{n0}$ on both side [81], we arrives at a new form of envelope function equation

$$
\begin{aligned}
-\frac{1}{2} a_{ij}(\mathbf{x}) \frac{\partial^2 F_n}{\partial x_i \partial x_j} - \frac{1}{2} b_i(\mathbf{x}) \frac{\partial F_n}{\partial x_i} - \sum_{n'} a_{ij}(\mathbf{x}) Q^i_{n'n} \frac{\partial F_{n'}}{\partial x_j} + \sum_{n'} (P_{n'n} - P^0_{n'n}) F_{n'}\\
+ \epsilon_{n0}(\varepsilon(\mathbf{x})) F_n = E\, F_n
\end{aligned}
\tag{3.64}
$$

In the equation, $a_{ij}(\mathbf{x})$ and $b_i(\mathbf{x})$ are related to deformation mapping and can be calculated once the displacement field $\mathbf{u}(\mathbf{x})$ is known. $Q^i_{n'n}$ and $(P_{n'n} - P^0_{n'n})$ can be calculated either by constructing the strain-parametrized basis set or fit empirically to experimental data. As a sanity check, when a crystal is undeformed, namely $\mathbf{u}(\mathbf{x}) = 0$, we have $a_{ij}(\mathbf{x}) = \delta_{ij}$, $b_i(\mathbf{x}) = 0$, $J(\mathbf{x}) = 1$, $P_{nn'} = P^0_{nn'}$, $\epsilon_{n0}(\varepsilon(\mathbf{x})) = \epsilon_{n0}$, and the envelope function equation will become

$$-\frac{1}{2}\nabla^2 F_n - \sum_{n'} q^i_{n'n}\frac{\partial F_{n'}}{\partial x_i} + \epsilon_{n0}F_n = E\,F_n \tag{3.65}$$

with $q^i_{n'n}$ being

$$q^i_{n'n} = \frac{1}{V}\int d\mathbf{x}\,[u_{n0}(\mathbf{x})]^\dagger\,\frac{\partial}{\partial x_i}u_{n'0}(\mathbf{x}) \tag{3.66}$$

Eq. 3.65 recovers the envelope function equation for bulk crystals [81].

## 3.6 Summary and Conclusion

To summarize, we have developed a new envelope function formalism for electrons in slowly-varying inhomogeneously strained crystals. The method expands the electronic wavefunctions in a smoothly deformed crystal as the product of slowly varying envelope functions and strain-parametrized Bloch functions. Assuming, with justifications, that the local crystal potential in a smoothly deformed crystal can be well approximated by the potential of a homogeneously deformed crystal with the same strain value, the unknown crystal potential in Schrödinger equation can be replaced by the a small set of strain-parametrized Bloch functions and the associated strain-parametrized energy eigenvalues at a chosen crystal momentum. Both the strain-parametrized Bloch functions and strain-parametrized energy eigenvalues can be constructed from *ab initio* or semi-empirical electronic structure calculation of homogeneously strained crystals at unit-cell level. The Schrödinger equation can then be turned into eigenvalue differential equations for the envelope functions. Due to the slowly-varying nature of the envelope functions, coarse spatial or fourier grids can be used to represent the envelope functions, therefore enabling the method to deal with relatively large systems. Compared to the traditional multi-band $\mathbf{k}\cdot\mathbf{p}$ envelope function method, our envelope function method has the advantage of keeping unit-cell level microstructure information since the local electronic structure information is obtained from *ab initio* or EPM calculations. Compared to the conventional EPM method, our method uses envelope function formalism to solve the global electronic structure, therefore has the potential to reduce the computational cost. The method can also be used empirically by fitting the parameters in our derived envelope function equations to experimental data. Our method thus provides a new route to calculate the electronic structure of slowly-varying inhomogeneously strained crystals.

# Chapter 4

# Deviatoric Stress-Driven Fusion of Nanoparticle Superlattices

## 4.1 Introduction

Colloidal nanocrystals of metals and semiconductors are usually passivated with organic ligands to prevent aggregation in solution. Monodisperse ligand-passivated nanocrystals can self-assemble into long-range ordered superstructures, often called Nanoparticle Superlattice (NPSL), supercrystal or supracrystal. NPSLs have been subject of intense research in recent years [102]. These soft-sphere colloidal supercrystals have much richer inter-particle interactions than their hard-sphere counterparts, evidenced by the variety of crystal structures that can be formed in binary NPSLs [103]. Study of collective phenomena in these "artificial solids" is a frontier of materials research. Mechanical properties of NPSLs are emergent properties in the sense that they derive from the collective interaction of the constituent nanoparticles. The study of mechanical behavior of NPSLs has only begun, and several pioneering experimental studies have appeared [104, 105, 106, 107, 108]. However, detailed, molecular-level understanding of the mechanical behavior of NPSLs is still very limited. An interesting possibility is room-temperature sintering ("fusion") of passivated nanoparticles ("artificial atoms") under stress, akin to the nuclear fusion of real atoms under ultra-high temperature and pressure. Recent experimental studies demonstrated that, mechanical deformations of gold and PbS nanoparticle assemblies in a pressurized environment lead to the formation of extended nanostructures, such as gold nanowire array [109], 3D nanostructured gold architecture [110] and PbS nano-sheet [111]. Yet the conditions under which such stress-driven transformations happen in NPSLs, as well as the associated molecular-level mechanisms, are not well understood.

In this chapter we use large-scale Molecular Dynamics (MD) simulations to study the mechanical behavior of gold NPSLs under both ambient and elevated pressures. We find that, due to the dominant roles of organic ligands in mechanical response [106, 107, 112], the NPSLs exhibit entropic viscoelasticity during compressive deformation at ambient pressure. At moderately elevated stresses, our simulation confirms Wu *et al*s experimental report [109] that gold NPSLs can be transformed into ordered gold nanowire arrays via deviatoric stress driven sintering ("fusion") of gold nanoparticles in the NPSLs. The following stress conditions are required to enable such fusion: (a) the presence of a background hydrostatic pressure $P$ of the order several hundred megapascal (MPa); (b) the presence of a critical deviatoric stress (uniaxial) $\tau$ in addition to the aforementioned hydrostatic pressure (triaxial) background. The direction of the deviatoric stress should be properly aligned with the crystallographic direction of the superlattice. In face-centered cubic (*fcc*) structure, this is the [110] nearest-neighbor (Burgers vector) direction of nanoparticles in the superlattice. On the basis of these insights, we demonstrate that stress-driven fusion of silver-gold (Ag-Au) binary NPSLs can lead to the formation of Ag-Au multi-junction nanowire arrays with similar kind of stresses.

## 4.2 Molecular Model and Computational Details

### 4.2.1 Molecular Model

The structural units of the gold NPSLs in our simulation are alkanethiol-passivated gold nanocrystals. To achieve a balance between computational cost and experimental relevance, each icosahedron-shaped gold nanocrystal in our simulation has diameter $d \approx 3$ nm, containing 561 gold atoms and exhibiting only (111) surfaces. The nanocrystals are capped by octanethiols ($S(CH_2)_7CH_3$). The ligands are self-assembled and absorbed onto the gold nanocrystal surfaces via gold-sulfur interaction in MD simulation. The coverage density of ligand is 136 molecules per nanocrystal, which corresponds to full ligand coverage density for the gold nanocrystal under consideration [113]. Individual gold nanoparticles are subsequently arranged into NPSLs with *fcc* superstructure. Our extensive Parrinello-Rahman MD simulation [60, 61] with variable size and shape of simulation box confirms that *fcc* is indeed the most stable superstructure for the system considered here. After equilibration, different mechanical loads are imposed on the superlattice. Periodic boundary conditions are employed. The size of simulation system is chosen based on the mechanical behavior under investigation. When plastic deformation is involved, the system typically contains more than 2500 nanoparticles.

The assignment of interaction potential is a critical issue in MD simulation. In our simulation, Morse potential was chosen to describe the interaction between gold atoms [114, 115]. Although embedded-atom method (EAM) potential [116] is known to be a more accurate potential model for metals, especially for metallic nanostructures, we found in our simulation that EAM potential has a few problems when used together with pair potential description of gold-sulfur interaction. Sulfur atoms tend to cause surface roughening of gold nanocrystals modeled with EAM potential. A small portion of sulfur atoms can penetrate one atomic layer beneath the gold surface, which no experimental evidence is available for support and is unphysical in our belief. This motivates our choice of Morse potential to model gold-gold interaction [114, 115]. While the simulations reported in this paper use Morse potential, we have nevertheless performed extensive simulations using EAM potential. The conclusions drawn in our study are not qualitatively affected. The critical hydrostatic pressure and deviatoric stress needed for fusion of gold NPSL into gold nanowire array was found to be higher (within a factor of two) for nanocrystals modeled with EAM potential. The higher values can be explained by the aforementioned penetration of sulfur atoms beneath gold nanocrystal surface, which makes it more difficult for ligands being displaced from the contact region between two neighboring nanoparticles before fusion.

To describe the interaction of alkanethiol ligands, we use the united atom (UA) potential by Paul *et al* [117]. Kushik *et al*'s recent work [118] demonstrated that Paul *et al*'s UA potential can accurately reproduce the chain conformation and dynamics of ligands modeled by very accurate, but computationally demanding all-atom MM3 potential [119]. The UA potential includes bond, angle, dihedral and non-bonded interactions.

The interaction between thiol ligands and gold nanocrystals is subtle, due to the quantum-mechanical nature of sulfur-gold bonding. The adsorption configuration of thiol on gold surface is still under debate [120]. Most studies in the literature used Morse potential to parameterize gold-sulfur interaction [121, 122, 123, 124]. Our gold-sulfur interaction model follows Zhang *et al* [121], except that we use Lennard-Jones potential instead of Morse potential to fit the adsorption energies of sulfur atoms on gold surfaces, as Morse potential has a relatively soft core which induces unphysical features at very high pressure. We note that Schapotschnikow *et al* [113] also use Lennard-Jones potential to model gold-sulfur interaction in their simulation of interactions between individual gold nanoparticles. We have selected Zhang *et al*'s gold-sulfur model [121] because the thiol diffusion barrier computed from Zhang *et al*'s model is very close to first-principles calculated thiol diffusion barrier on gold (111) surface assuming direct adsorption geometry [125], as well as gold adatom diffusion barrier on gold (111) surface [126]. The gold adatom model, namely thiol ligands bind to gold surface via gold adatoms, has recently emerged as a strong candidate for ligand adsorption on gold surface [120]. Due to the covalent bonding between sulfur and gold, thiol diffusion on gold surface may involve diffusion of thiol-adatom complex, in which case the thiol diffusion barrier should be close to that of gold adatom. Indeed, fast diffusion of thiol ligands on gold surface was experimentally observed [127], suggesting that the thiol diffusion barrier should be close to thermal energy at room temperature.

For silver-gold (Ag-Au) binary nanoparticle superlattice simulation, we use Morse potential [114] to describe the interaction between the silver atoms. The cross-interaction between gold and silver atoms are computed using Lorentz-Berthelot mixing rules. As previous studies showed that the interaction strength and equilibrium distance of Ag-S bond is very close to those of Au-S bond [128, 129], we use the Au-S interaction parameters to approximate those of Ag-S interaction. The non-bonded interactions between the alkyl group of thiol ligands and silver are relatively weak. Small variation of these interaction parameters is unlikely to influence the simulation results much. Hence, the parameters are taken to be same as those between ligands and gold nanoparticles.

The force field parameters for the interaction models described above are listed in details bellow.

### Gold-Gold Interaction

$$E = D_0 \left[ e^{-2\alpha(r-r_0)} - 2e^{-\alpha(r-r_0)} \right], \qquad r < r_c \tag{4.1}$$

where $D_0 = 10.956$ kcal/mol, $\alpha = 1.5830$ Å$^{-1}$, $r_0 = 3.0242$ Å. The interaction cut-off distance $r_c = 10$ Å is the default value for non-bonded interactions in our simulations. Interaction potentials are shifted to zero at $r_c$.

### Ligand Intra- and Inter-Molecular Interactions

The thiol ligands ($S(CH_2)_nCH_3$) are coarse-grained such that each $CH_2$ or $CH_3$ unit is treated as a single atom. The total conformation energy of thiol molecules consists of energy coming from bond-stretching, angle-bending, dihedral-torsion, and non-bonded interactions.

$$E = E_{bond} + E_{angle} + E_{torsion} + E_{non-bonded} \tag{4.2}$$

where

$$E_{bond} = k(r - r_0)^2 \tag{4.3}$$

$$E_{angle} = k' \left[\cos(\theta) - \cos(\theta_0)\right]^2 \tag{4.4}$$

$$E_{dihedral} = \frac{1}{2}K_1 \left[1 + \cos(\phi)\right] + \frac{1}{2}K_2 \left[1 - \cos(2\phi)\right] + \frac{1}{2}K_3 \left[1 + \cos(3\phi)\right] \tag{4.5}$$

$$E_{non-bonded} = 4\epsilon \left[\left(\frac{\sigma}{r}\right)^{12} - \left(\frac{\sigma}{r}\right)^{6}\right], \qquad r < r_c \tag{4.6}$$

The interaction parameters for the alkyl groups of thiol ligands are the original values of Paul *et al* [117, 118]. Interactions parameters involving sulfur atoms were taken from literature [124, 130, 131, 132]. These interaction parameters are listed in Table 4.1.

Table 4.1: Interaction Parameters for Ligand Molecules.

| bond | $r_0$ (Å) | $k$ [kcal/(mol/Å$^2$)] |
|---|---|---|
| S-$CH_2$ | 1.81 | 222 |
| $CH_2$-$CH_2$ | 1.53 | 317 |
| $CH_2$-$CH_3$ | 1.53 | 317 |

| angle | $\theta_0$ (degree) | $k'$ (kcal/mol) |
|---|---|---|
| S-$CH_2$-$CH_2$ | 114.4 | 62.5 |
| $CH_2$-$CH_2$-$CH_2$ | 110.01 | 60.0 |
| $CH_2$-$CH_2$-$CH_3$ | 110.01 | 60.0 |

| dihedral | $K_1$ (kcal/mol) | $K_2$ (kcal/mol) | $K_3$ (kcal/mol) |
|---|---|---|---|
| S-$CH_2$-$CH_2$-$CH_2$ | 1.6 | -0.8670 | 3.24 |
| $CH_2$-$CH_2$-$CH_2$-$CH_2$ | 1.6 | -0.8670 | 3.24 |
| $CH_2$-$CH_2$-$CH_2$-$CH_3$ | 1.6 | -0.8670 | 3.24 |

| non-bonded interaction | $\sigma$ (Å) | $\epsilon$ (kcal/mol) |
|---|---|---|
| S | 4.25 | 0.39743 |
| $CH_2$ | 4.009 | 0.09344 |
| $CH_3$ | 4.009 | 0.22644 |

For non-bonded interactions, the standard Lorentz-Berthelot mixing rules are used to compute the cross-interaction terms.

### Ligand-Gold Interaction

The ligand-gold interaction consists of sulfur-gold interaction and alkyl group-gold interaction. The interaction between gold and sulfur is modeled by Lennard-Jonnes potential:

$$E = 4\epsilon \left[ \left( \frac{\sigma}{r} \right)^{12} - \left( \frac{\sigma}{r} \right)^{6} \right], \qquad r < r_c \tag{4.7}$$

where $\epsilon = 3.182$ kcal/mol, $\sigma = 2.586$ Å.

The interaction of alkyl units with gold is modeled by Lennard-Jones potential as well. The interaction strength, however, is much weaker than sulfur-gold interaction. The interaction parameters are taken from literature [124, 130]. For interaction between Au and $CH_2$ units, $\epsilon = 0.0678$ kcal/mol, $\sigma = 3.42$ Å. For interaction between Au and $CH_3$ unit, $\epsilon = 0.0826$ kcal/mol, $\sigma = 3.42$ Å.

### Interaction Parameters for Silver-Gold Binary Nanoparticles Superlattices

For silver-gold binary NPSLs simulation, we also use Morse potential to describe the interaction between the silver atoms:

$$E = D_0 \left[ e^{-2\alpha(r-r_0)} - 2e^{-\alpha(r-r_0)} \right], \qquad r < r_c \tag{4.8}$$

The interaction parameters, taken from literature [114], are $D_0 = 7.499$ kcal/mol, $\alpha = 1.3535$ Å$^{-1}$, and $r_0 = 3.1300$ Å. The cross-interaction between gold and silver atoms are computed using Lorentz-Berthelot mixing rules, which gives $D_0 = 9.2275$ kcal/mol, $\alpha = 1.4683$ Å$^{-1}$, $r_0 = 3.0771$ Å.

For the interaction between the sulfur atoms of thiol ligands and silver nanoparticles, previous studies showed that the interaction strength and equilibrium distance of Ag-S bond are very close to those of Au-S bond [128, 129]. Therefore, we use the interaction parameter of Au-S to describe Ag-S interaction, namely

$$E = 4\epsilon \left[ \left( \frac{\sigma}{r} \right)^{12} - \left( \frac{\sigma}{r} \right)^{6} \right], \qquad r < r_c \tag{4.9}$$

where $\epsilon = 3.182$ kcal/mol, $\sigma = 2.586$ Å.

The van der Waals interaction between the alkyl group of thiol and silver is relatively weak. Small variation of this set of parameters will not influence the simulation results much. Hence, the parameters are taken to be same as those of thiol-gold interaction.

### 4.2.2 Simulation Procedure for Stress-Driven Fusion of Nanoparticle Superlattices

We first build individual ligand-passivated gold nanoparticles through MD simulation. An icosahedral gold nanocrystal is located at the center of a simulation box, surrounded by thiol ligands. The number of ligands is larger than the number corresponding to the maximum ligand coverage on nanocrystal surface. The simulation box is large enough so that periodic images do not interact with each other. Initially, the temperature of the system is set to be 450 K in the constant particle number, constant volume and constant temperature ($NVT$) ensemble. Due to the strong attractive interactions between gold and sulfur atoms, the thiol ligands start to self-assemble on the nanocrystal surface. After running simulation for ~1 ns, the temperature of the system is decreased to 300 K over a period of 1 ns. The system is then allowed to equilibrate at 300 K for more than 3 ns. At the end of simulation, ligands not absorbed on the nanocrystal surface will be removed and the configuration will be used for building nanoparticle superlattice.

To build NPSLs, the ligand-passivated gold nanoparticles are initially put at the lattice sites corresponding to *fcc* superlattice. Previous simulation of gold NPSLs using different potential models by Landman *et al* suggested that the favorable superlattice structure is controlled by the ratio of between ligand length and nanocrystal core size [112]. Our own extensive (more than 20 ns) Parrinello-Rahman MD simulation [60, 61] with variable size and shape of simulation box confirm that *fcc* is indeed the most stable superstructure for the nanoparticle superlattice considered in this work. If the length of ligand is increased or the size of gold core is decreased, we are able to observe *fcc* to body-centered cubic (*bcc*) or body-centered tetragonal (*bct*) structural transitions [112].

The nanoparticles put at the lattice sites of *fcc* superstructure are initially far away from each other, with the distance between two nearest-neighbor nanoparticles about two times the diameter of a nanoparticle. We then put the system under constant temperature, constant stress (thermodynamic tension), and particle number ($T\mathbf{t}N$) ensemble. Nosé-Hoover type thermostat and barostat [63, 61, 64, 133] are used to control temperature and stress, and the simulation box are allowed to change in both size and shape [60, 61]. The damping coefficients for thermostat and barostat are both 0.01 fs$^{-1}$. Barostat damping coefficients equal to 0.001 fs$^{-1}$ has also been tested but no noticeable difference in simulation results was found. Subsequently, we set the target pressure of the $T\mathbf{t}N$ ensemble to zero at constant temperature of 300 K, and run simulation for 1 ns. At this stage, the $x$, $y$ and $z$ dimensions of the simulation box are allowed to shrink or expand independently, but not the $xy$, $yz$ and $xz$ dimensions. As the barometer couples to the size and shape of simulation box, the nanoparticles would approach each other and the supercrystal becomes compact. In the next step, we allow all dimensions of the simulation box to relax, and equilibrate the superlattice at 300 K and zero stresses in the $T\mathbf{t}N$ ensemble for 2 ns. At the end of this step, the energy and volume of the system would typically have converged.

To study stress-driven fusion of nanoparticle superlattices under different pressure, we first build gold NPSLs with one of the low-index superlattice direction, namely the [100], [110] or [111] direction, orienting along, for example, the $z$ direction of the orthorhombic simulation box in Cartesian coordinates. We then equilibrate the system in the $T\mathbf{t}N$ ensemble with zero stress components according to the procedures described above. Afterward, the $xx$, $yy$ and $zz$ stress components of the ensemble ($\sigma_{xx}$, $\sigma_{yy}$ and $\sigma_{zz}$) are elevated to the target pressure $P$ over a 1 ns simulation, while $\sigma_{xy}$, $\sigma_{yz}$ and $\sigma_{xz}$ are fixed at zero. Subsequently, we equilibrate the system under stress components $\sigma_{xx} = \sigma_{yy} = \sigma_{zz} = P$ and $\sigma_{xy} = \sigma_{yz} = \sigma_{xz} = 0$ for 2 ns, followed by uniaxial deformation of the NPSLs. We deform the $z$ dimension of the simulation box (corresponding to one of the low-index superlattice direction) with a fixed engineering strain rate of $-1.0 \times 10^{-4}$ per ps. The length of simulation box dimension along the $z$ direction will be one half of the original length after 5 ns simulation. During deformation, barostat controls the stress components to simulate the uniaxial deformation of the NPSLs in the presence of fluid-generated pressure background. For example, if we deform along the $z$ direction of the simulation box, $\sigma_{xx}$ and $\sigma_{yy}$ will be fixed at $P$, while $\sigma_{xy}$, $\sigma_{yz}$ and $\sigma_{xz}$ are all controlled to be zero.

The simulation procedures for equilibration and stress-driven fusion of binary NPSLs are similar to single component gold NPSLs.

### 4.2.3 Computing the Elastic Constants of Nanoparticle Superlattices

We use strain-fluctuation method [134, 135] to compute the elastic constants of NPSLs. Direct calculation of elastic constants from stress-strain curves of NPSLs is challenging at finite temperature, due to the presence of thermal fluctuation which necessitates careful statistical averaging. The benefit of strain-fluctuation method is that full elastic tensor can be obtained in one simulation. However, strain-fluctuation method is known to converge very slowly. In our simulation, convergence of elastic constants computed via strain fluctuation method typically takes more than 10 nanoseconds after the simulation cell is fully equilibrated. We have confirmed that the elastic constants calculated using strain-fluctuation method is the same as those obtained via direct deformation in constant particle, constant volume and constant temperature ($NVT$) ensemble in the small deformation strain limit.

#### Elastic Constants in Voigt Notation

In linear elasticity, stress and strain are related by Hooke's law

$$\sigma_{ij} = \sum_{k,l} C_{ijkl}\epsilon_{kl}, \tag{4.10}$$

where $\sigma_{ij}$ and $\epsilon_{kl}$ denote stress and strain tensor respectively. $C_{ijkl}$ is the fourth-rank elastic stiffness tensor. Symmetry relations between the tensor elements allow the use of Voigt notation to simplify Hooke's law. The indices mapping scheme in Voigt notation is shown in Table 4.2:

Table 4.2: Indices Mapping in Voigt Notation

| Regular Index | 11 | 22 | 33 | 23 or 32 | 13 or 31 | 12 or 21 |
|---|---|---|---|---|---|---|
| Voigt Index | 1 | 2 | 3 | 4 | 5 | 6 |

It then follows $C_{1111} = C_{11}$, $C_{1122} = C_{12}$, $C_{1123} = C_{14}$, $C_{2323} = C_{44}$, *etc.* The elements of stress tensor can be written in Voigt notation as $\sigma_{11} = \sigma_1$, $\sigma_{22} = \sigma_2$, $\sigma_{33} = \sigma_3$, $\sigma_{23} = \sigma_{32} = \sigma_4$, $\sigma_{13} = \sigma_{31} = \sigma_5$, $\sigma_{12} = \sigma_{21} = \sigma_6$. Elements of strain tensor can be written as $\epsilon_{11} = \epsilon_1$, $\epsilon_{22} = \epsilon_2$, $\epsilon_{33} = \epsilon_3$, $2\epsilon_{23} = 2\epsilon_{32} = \epsilon_4$, $2\epsilon_{13} = 2\epsilon_{31} = \epsilon_5$, $2\epsilon_{12} = 2\epsilon_{21} = \epsilon_6$. With this index transformation, Hooke's law becomes

$$\sigma_i = C_{ij}\epsilon_j, \tag{4.11}$$

where $C_{ij}$ is now a 6×6 matrix. $C_{ij}$, the elastic constant matrix, is what we aim to compute from simulation.

We can invert Hooke's law as

$$\epsilon_i = S_{ij}\sigma_j. \tag{4.12}$$

$S_{ij}$, the compliance matrix, is the matrix inverse of $C_{ij}$. In Voigt notation, $S_{ij}$ is related to $S_{ijkl}$ (full compliance tensor) as:

$S_{mn} = 2S_{ijkl}$ if one and only one of $m$ or $n$ is equal to 4, 5, or 6;

$S_{mn} = 4S_{ijkl}$ if both $m$ and $n$ are equal to 4, 5, or 6;

$S_{mn} = S_{ijkl}$ otherwise.

The full compliance tensor $S_{ijkl}$ is what we can obtain from strain-fluctuation method, which we will describe below. Once $S_{ijkl}$ is known, the compliance matrix can be constructed via the above rules. The elastic constant matrix is then obtained by matrix inversion of $S_{ij}$.

### Fluctuation and Elastic Constants in Molecular Dynamics Simulation

The fundamental equation employed in strain-fluctuation method is [134, 135]

$$\langle \epsilon_{ij}\epsilon_{kl} \rangle - \langle \epsilon_{ij} \rangle \langle \epsilon_{kl} \rangle = \frac{k_{\mathrm{B}}T}{V} S_{ijkl}, \tag{4.13}$$

where $k_{\mathrm{B}}$ is the Boltzmann constant, $V$ is the volume of the system; $\langle\,\rangle$ denotes ensemble average in constant temperature, constant stress (thermodynamic tension), and constant particle number ($T\mathbf{t}N$) ensemble [136]. In practical molecular dynamics simulation, the size and shape of simulation box are allowed to change according to the method of Parrinello and Rahman [60, 61]. Let $h = \{\mathbf{a}, \mathbf{b}, \mathbf{c}\}$ represents matrix constructed from the supercell vectors $\mathbf{a}, \mathbf{b}$ and $\mathbf{c}$. The instantaneous strain tensor $\boldsymbol{\epsilon}$ is related to the $h$ matrix as [135]

$$\boldsymbol{\epsilon} = \frac{1}{2} \left[ (h_0^{-1})^{\mathrm{T}} h^{\mathrm{T}} h (h_0^{-1}) - I \right], \tag{4.14}$$

where $h_0$ is a reference matrix. In our case, $h_0$ is taken to be the time average of $h$ after the system has equilibrated. The superscript $-1$ and T stand for matrix inversion and transposition, respectively. $I$ represents identity matrix. Running sufficiently long simulation after equilibration, one can compute $\langle \epsilon_{ij}\epsilon_{kl} \rangle$, $\langle \epsilon_{ij} \rangle \langle \epsilon_{kl} \rangle$ and average volume $V$. The compliance tensor $S_{ijkl}$ is then calculated according to Eq. 4.13. The elastic constant matrix $C_{ij}$ can be obtained following the procedures described in the previous section.

The bulk modulus $K$ can be calculated from volume fluctuations in molecular dynamics simulation. The fluctuation formula for bulk modulus is [137]

$$K = \frac{\langle V \rangle k_{\mathrm{B}} T}{\langle V^2 \rangle - \langle V \rangle^2} \tag{4.15}$$

### Simulation Procedures for Calculation of Elastic Constants

A gold NPSL system consisting of 2×2×2 *fcc* supercell is created by placing 32 gold nanoparticles $\mathrm{Au}_{561}(\mathrm{SC}_8)_{136}$ at the initial lattice positions, totaling 57120 (united) atoms. The configurations of individual gold nanoparticles are fully equilibrated at 300 K. In total, the superlattice contains 57120 (united) atoms. The relaxation procedures for superlattice are the same as those for single-component gold nanoparticle superlattices. Enlarging the system from a 2×2×2 supercell to a 3×3×3 supercell does not change the calculated elastic constants beyond the convergence error limit.

For calculation of elastic constants under different hydrostatic pressure, we first raise the pressure of the system in the $T\mathbf{t}N$ ensemble to a target pressure $P$ over a simulation period of 1 ns. The system is then equilibrated at $P$ for 2 ns. Both the size and shape of the simulation box are allowed to change. The $\sigma_{xx}$, $\sigma_{yy}$ and $\sigma_{zz}$ components of the stress tensor in the $T\mathbf{t}N$ ensemble are independently controlled at the target pressure, while the $\sigma_{xy}$, $\sigma_{yz}$ and $\sigma_{xz}$ components are independently controlled at zero. The simulation system is then fully equilibrated until the potential energy and total volume of the system reach equilibrium values. This step takes less than 1 ns when $P$ is around ambient pressure but could take more than 10 ns when $P$ is larger than 100 MPa, as we find higher pressure leads to slower relaxation dynamics of the ligands. Production run for the computation of elastic constants takes 15 ns to 20 ns for the elastic constants to converge.

## 4.3 Results and Discussion

### 4.3.1 Entropic Viscoelasticity of Gold Nanoparticle Superlattices

Figure 4-1a shows a typical molecular configuration of the gold NPSLs. We compute the full elastic tensor of the NPSL at 300 K using strain fluctuation method [112, 135, 134]. The computed three independent elastic constants are $C_{11} = 1.18$ GPa, $C_{12} = 1.15$ GPa and $C_{44} = 68$ MPa at $P = 0$, and the bulk modulus $B = 1.16$ GPa. Compared to simple atomic elastic solids [116], the ratio of $C_{44}/B$ is smaller by an order of magnitude, which however is reminiscent of complex fluids. The computed elastic moduli are in close agreement with Landman and Luedtke's simulation of

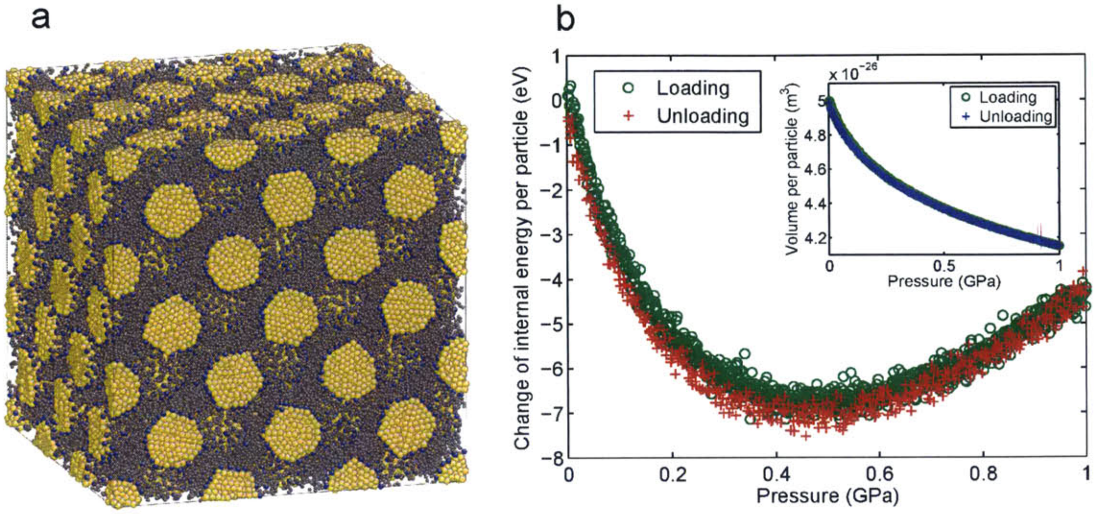

Figure 4-1: (a) Equilibrium configuration of octanethiol passivated gold NPSL at 300 K and zero pressure. The atoms depicted are gold (yellow), sulfur (blue), and carbon (gray). The system, which is primarily used for studies involving only hydrostatic pressure, contains 108 gold nanoparticles. (b) Internal energy change ($\Delta U$) per nanoparticle during an isothermal compression-decompression cycle of gold NPSL at 300 K. Inset shows the change of volume per nanoparticle during the cycle.

gold NPSLs [112], although in their study, the gold nanocrystals are modeled as undeformable rigid bodies. The correspondence can be accounted by the much higher mechanical rigidity of metallic gold compared to the organic ligands, resulting in the dominance of ligands in the mechanical response of the NPSLs at ambient pressure [106, 107].

Indeed, we find the NPSLs exhibit polymer-like entropic viscoelasticity during compressive deformation at low pressure. Figure 4-1b shows the change of internal energy per nanoparticle of the NPSLs during an isothermal compression-decompression cycle at 300 K, for hydrostatic pressure $P$ varied between zero to 1 GPa. The initial configuration is fully equilibrated at zero external stress in the constant temperature, constant stress, and particle number ($T\mathbf{t}N$) ensemble[61, 134, 64, 63] for 20 ns, before cycling pressure in the ensemble over a 10 ns simulation period. When the pressure is lower than 0.5 GPa, the internal energy $U$ of the system decreases while the pressure is increased. This behavior is contrary to that of enthalpy-dominated hard materials like simple metals. While mechanical work $W$ is continuously done to the system, the system dumps *more* heat to the environment (thermostat), $\Delta Q = \Delta U - \Delta W < 0$. If the compression is performed quasi-statically (without dissipation) and reversibly, $T\Delta S = \Delta Q$ , then the system entropy must decrease rapidly. Analysis of the loading-unloading cycle indicates that the heat exchange is mainly due to entropy reduction (dissipation is small), and $T|\Delta S| \gg |\Delta U|$ , which is the defining characteristics of entropy-dominated (instead of enthalpy-dominated) elasticity. As shown in Figure 4-1b, after loading and unloading, the potential energy and volume of the system almost return to the initial values. The remaining differences of potential energy and enthalpy between the initial and final configurations can be eliminated after equilibrating the system at zero pressure for another 1 ns. The small hysteresis during the loading-unloading cycle indicates that most of the mechanical work performed on the system is not dissipated, and $|\Delta Q| \approx T|\Delta S| \gg |\Delta U|$. Such entropic mechanical response is also observed in uniaxial compression of the NPSLs, albeit for uniaxial compression, viscoelasticity [104, 107] and energy dissipation become more pronounced. The entropy reduction of the NPSLs during compressive deformation comes from the decrease of the configurational entropy of the ligands, which results from the significant reduction of free volume accessible to the ligands under compression (inset of Figure 4-1b). The simultaneous decrease of potential energy comes from stronger van der Waals attraction between the ligands [112]. The total free energy change, given by $\Delta F = \Delta U - T\Delta S = \Delta Q + \Delta W - T\Delta S \approx \Delta W = -\int PdV$ , remains positive.

### 4.3.2 Structural Stability of Gold Nanoparticles Superlattices under High Pressure

The structural stability of NPSLs under high pressure has been subjected to experimental studies recently [109, 138]. However, whether purely hydrostatic pressure alone can induce fusion of NPSLs is still under debate. To help answer this question, we carry out hydrostatic deformation of gold NCSLs under high pressure. Starting with a fully equilibrated gold NPSL with the same configuration as in Figure 4-1a, we increase the normal stress components of the $T\mathbf{t}N$ ensemble ($\sigma_{xx}$, $\sigma_{yy}$ and $\sigma_{zz}$) from zero to 20 GPa over a simulation period of 20 ns, while setting the shear stress components of the ensemble ($\sigma_{xy}$, $\sigma_{xz}$ and $\sigma_{yz}$) to fluctuate around zero. This aims to simulate the hydrostatic compression of the NPSL in a fluid environment. The normal stresses of the ensemble are then kept at 20 GPa for another 5 ns. The simulation box is allowed to change in both size and shape. Over the entire course of the simulation, the system maintains *fcc* superstructure. No first-order phase transformation, nor fusion of nanoparticles, is observed. This is consistent with Podsiadlo *et al*'s recent high pressure experiment, where they observed "nearly perfect structural stability" of PbS NPSL with fcc superlattice for pressure up to 12.5 GPa [138]. Our simulation also indicates that purely hydrostatic high pressures result in the jamming of ligands in gold NPSLs, reducing the ligands surface diffusivity and preventing the gold nanoparticles from sintering with each other.

### 4.3.3 Deviatoric Stress-Driven Fusion of Nanoparticles Superlattices into Ordered Nanowire Arrays

While high hydrostatic pressure alone does not induce the fusion of gold NPSLs in our simulation, we find that a moderate level of pressure, combined with a deviatoric stress $\tau$ of hundreds of MPa along an appropriate direction of the superlattice, transform the gold NPSLs into ordered gold nanowire arrays, which is consistent with previous experimental observation [109]. Uniaxial stresses along one of the three low-index directions of the fcc superlattice, namely the [100], [111] and [110] directions, are considered. We build gold NPSLs with one of the low-index directions orienting along, for example, the $z$ edge of the orthorhombic simulation box in Cartesian coordinates. The system, which includes around 2500 gold nanoparticles, is initially equilibrated in the $T\mathbf{t}N$ ensemble at zero stress. The pressure $P$ of the system is then raised from zero to 1 GPa in the $T\mathbf{t}N$ ensemble over a period of 1 ns. This is followed by equilibration at 1 GPa for 2 ns, at the end of which large fluctuations in energy and volume have ceased. Subsequently, the $z$ dimension of the simulation box is deformed with a fixed engineering strain rate of $1.0 \times 10^{-4}$ per ps. Meanwhile, the $\sigma_{xx}$ and $\sigma_{yy}$ of the ensemble are controlled by barostat at 1 GPa, while $\sigma_{xy}$, $\sigma_{xz}$ and $\sigma_{yz}$ are controlled to be zero. This aims to simulate the uniaxial deformation of the NPSLs in the backdrop of a fluid-generated triaxial pressure. The deviatoric stress along the $z$ direction is defined as $\tau \equiv \sigma_{zz} - P$. The engineering strain of deformation is calculated as $\varepsilon \equiv (L_z - L_{z0})/L_{z0}$ , where $L_{z0}$ and $L_z$ are the lengths of the simulation box along the $z$ direction at the beginning and during deformation, respectively.

For deformation along the [100] or [111] direction of the gold NPSLs, we could not observe ordered fusion of nanoparticles in the superlattices. Compressive stress along these two directions induces significant variation in the size and shape of simulation box, indicating plasticity and/or phase transformation of the supercrystal, but the ordered fusion of nanoparticles does not occur. We note that Wu *et al* did not observe ordered fusion of [111] oriented gold NPSLs in their high pressure experiment [110] either.

For uniaxial compression along the [110] direction, however, we observe stress-driven fusion of gold nanoparticles into ordered gold nanowire array. The [110] direction is the nearest-neighbor direction of nanoparticles in fcc superlattice. Therefore, uniaxial compression along the [110] direction drives neighboring nanoparticles along this direction closer to each other. Uniaxial compression overcomes the entropic and steric repulsion of the ligands between the neighboring nanoparticles, and eventually leads to the sintering of nanocrystal cores along the [110] direction. Ordered nanowire array forms as a result. This process is illustrated in Figure 4-2. Figure 4-2a shows the configuration of the gold NPSLs before deformation. The schematic beneath illustrates the idealized configuration of the nanoparticles in the (001) plane of the superlattice. In Figure 4-2b, the engineering strain of the deformation reaches $-0.2$. The associated schematic shows the conformation change and reorganization of ligands on the nanocrystal surfaces, a picture supported by our detailed analysis (Figure 4-6). When strain reaches $-0.4$ (Figure 4-2c) neighboring nanoparticles have overcome the passivation of ligands and attached to each other, forming ligand-passivated gold nanowire array.

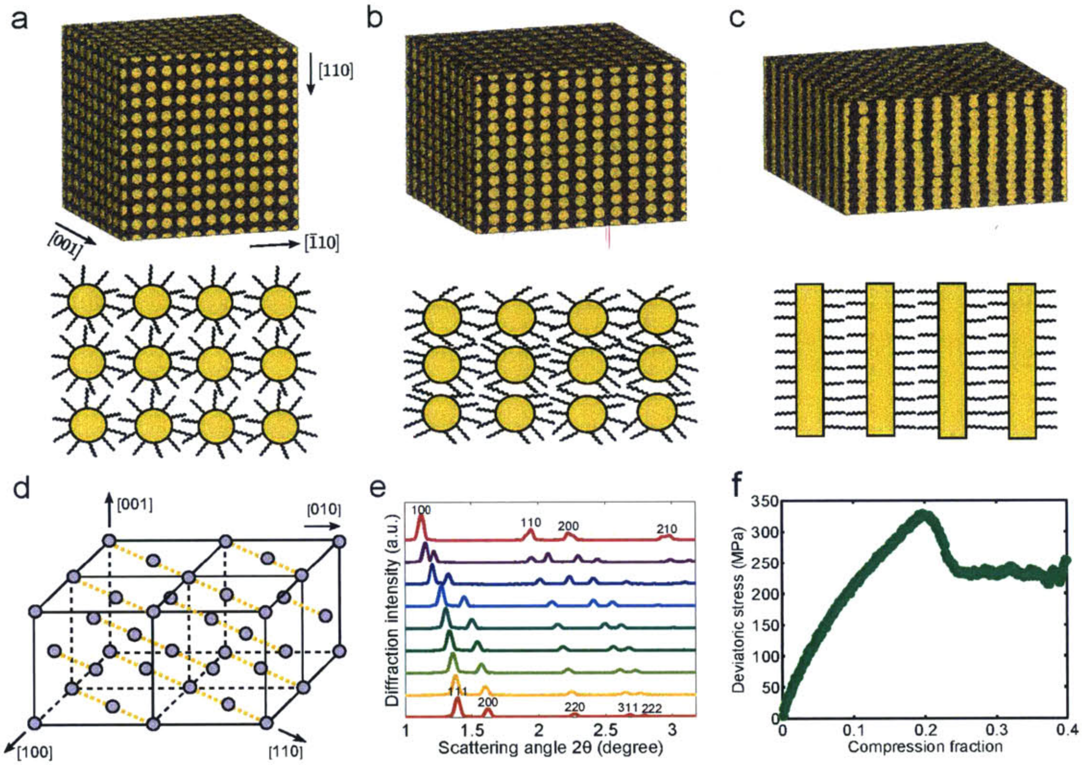

Figure 4-2: Stress-driven fusion of gold NPSLs along the [110] direction of superlattice at 1 GPa pressure. (a-c): MD simulation snapshots and schematics showing the structural evolution of NPSL at different deformation stages. (a) Configuration of the system equilibrated at 1 GPa. The superlattice directions are labeled. (b) Configuration at engineering strain $\varepsilon$ equal to $-0.2$. After deformation, neighboring nanoparticles become closer along the [110] direction. The process is accompanied by ligand conformation change and relocation. (c) Configuration at $\varepsilon = -0.4$. Most of the gold nanoparticles have fused together along the [110] direction and ordered nanowires are formed. (d) Lattice model of nanoparticle fusion along the [110] direction of *fcc* superlattice. Neighboring nanoparticles fuse along the dashed orange lines in the figure. (e) Evolution of SAXS patterns computed from simulation data. The incident beam passes along the [110] direction. Diffraction peaks due to the *fcc* superlattice (the bottom curve) and the nanowire array arranged in triangular lattice (the top curve) are labeled. The X-ray wavelength used for diffraction calculation is the same as in Wu *et al*'s experiments [109]. (f) Deviatoric stress as a function of compression fraction (absolute value of strain).

In Figure 4-2d, we illustrate the fusion of NPSL in a crystallographic model. The fused nanoparticles form parallel nanowires along the [110] direction. Under compression, these wires pack closely into triangular lattice, with $P6mm$ symmetry. The structural evolution is also captured by computing the small-angle X-ray scattering

(SAXS) patterns during stress-driven fusion, which is shown in Figure 4-2e. The evolution of the SAXS patterns agrees with Wu *et al*'s experimental data[109]. The critical deviatoric stress $\tau_{\mathrm{fusion}}$ fusion needed to drive fusion at $P = 1$ GPa pressure, as determined from the deviatoric stress versus engineering strain curve in Figure 4-2f, is around 330 MPa.

In addition to the orientation of superlattices, the existence of a moderate pressure background is found to be crucial for ordered fusion of NPSLs. We carry out uniaxial deformation of [100], [111] and [110] oriented superlattices at $P = 0$. In all three cases, ordered fusion could not be observed. This is because with $C_{44}(P = 0) = 68$ MPa, $\tau$ of hundreds of MPa would exceed the ideal shear strength [11] and thus the plastic yield strength $\tau_{\mathrm{Y}}(P = 0)$ of the supercrystal, which will trigger supercrystal plasticity before fusion can happen. A moderate pressure $P > 0$ is needed so $\tau_{\mathrm{Y}}(P > 0)$ is enhanced, delaying the competing supercrystal plasticity processes.

This idea motivates us to map out the pressure-dependent fusion behavior of [110] oriented gold NPSLs. We simulate the uniaxial deformation of [110] oriented gold NPSLs under different pressures, and look at the configuration of the system at the end of deformation. The system, which is initially equilibrated at a given pressure $P$, is deformed along the z dimension of the simulation box corresponding the [110] direction, during which the $\sigma_{xx}$ and $\sigma_{yy}$ of the ensemble are fixed at $P$. The shear stress components of the ensemble, $\sigma_{xy}$, $\sigma_{xz}$ and $\sigma_{yz}$, are controlled by barostat to be zero. When $P$ is small, uniaxial compression leads to twinning-like plastic deformation of the superlattice along the [110] direction when the strain reaches around $\varepsilon = -0.2$. This triggers mechanical yielding of the system. Further deformation leads to partial structural disordering of the superlattice. When $P$ is increased to around 100 MPa, partial fusion of nanoparticles along the [110] direction starts to emerge. If $P$ is further increased, more and more nanoparticles are fused together along the [110] direction before the system mechanically yields. Finally, when $P$ reaches 350 MPa, all the nanoparticles are able to fuse together along the [110] direction. This transition is shown in the simulation snapshots of Figure 4-3a-c. Such simulation over a wide range of pressure P enables us to plot a non-equilibrium stress-driven "pro-

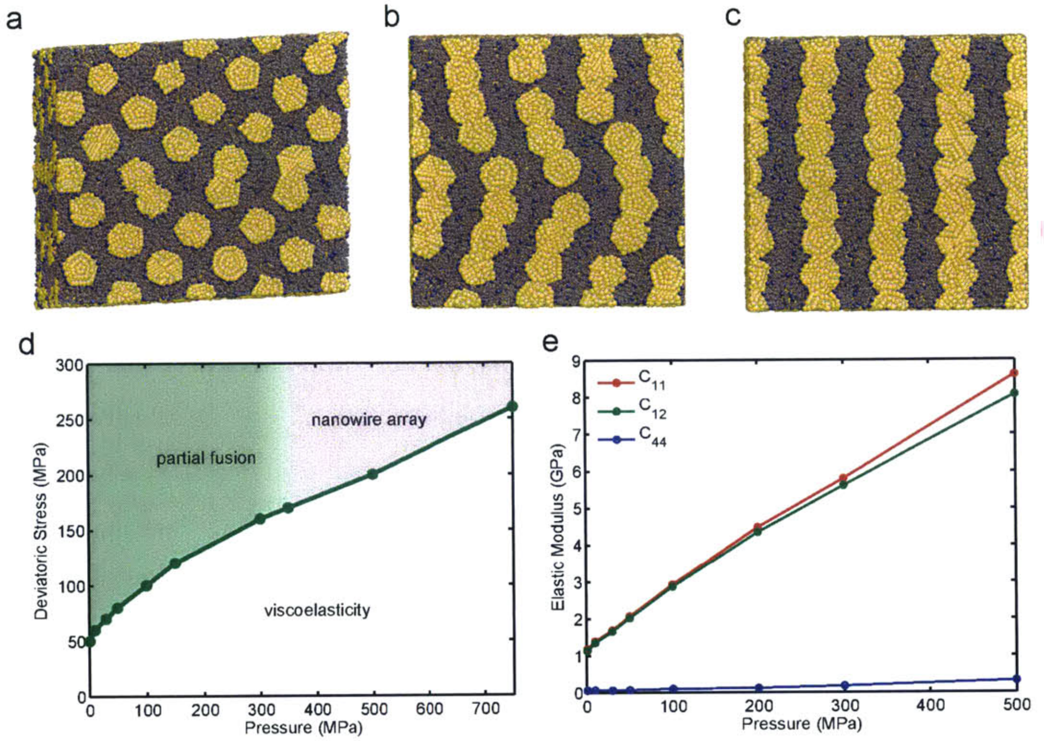

Figure 4-3: (a-c): Configurations of gold NPSLs at strain equal to $\varepsilon = -0.4$ after uniaxial deformation along the [110] direction in the presence of different hydrostatic pressure. (a), (b) and (c) correspond to pressure equal to 100 MPa, 300 MPa, and 500 MPa respectively. Gold nanoparticles are partially fused together along the [110] direction in (a) and (b), while in (c), nanowire array is formed. (d) Non-equilibrium stress-driven fusion processing diagram of the simulated [110] oriented gold NPSL. The horizontal axis is the pressure applied on the system, while the vertical axis is the maximum deviatoric stress applied along the [110] direction during deformation. The green line represents the maximum deviatoric stress before fusion or mechanical yielding of NPSL at different pressure. By observing the configurations of the systems at the end of deformation, different regions in the stress space are determined and labeled in the diagram. Nanowire array are formed when both applied pressure and deviatoric stress exceed certain critical values. (e) Computed elastic moduli $C_{11}$, $C_{12}$ and $C_{44}$ of the NPSL as a function of pressure

cessing diagram" of the [110] oriented gold NPSLs, which is presented in Figure 4-3d. The processing diagram indicates the existence of three regions in stress space, corresponding to viscoelasticiy, partial fusion and formation of ordered nanowire arrays, respectively. Formation of nanowire arrays only happens when both the pressure $P$ and the deviatoric stress $\tau \equiv \sigma_{zz} - P$ exceed certain critical values. The critical fusion pressure is found to be $P_{\text{fusion}} \approx 350$ MPa, and the critical fusion deviatoric stress is found to be $\tau_{\text{fusion}} \approx 170$ MPa.

We have also studied stress driven fusion of gold NPSLs consisting of larger-sized gold nanoparticles, and found the same order of magnitude of critical pressure and deviatoric stress values. For gold NPSLs consisting of dodecanethiol ($S(CH_2)_{11}CH_3$) passivated gold nanocrystals with core diameter ~4 nm in *fcc* type superstructure, the critical pressure $P_{\text{fusion}}$ and deviatoric stress $\tau_{\text{fusion}}$ needed for formation of nanowire arrays are both found to be around 200 MPa.

While stress-driven fusion of single-component gold NPSLs have been demonstrated in experiments [109, 110], stress-driven fusion of binary NPSLs [103] has not been shown experimentally. We hence carried out MD simulation of a model binary NPSL, Ag-Au binary NPSL in sodium-chloride (NaCl) type superstructure. Binary NPSLs with this type of supercrystal structure have been created experimentally [103, 139]. Previous studies demonstrated that the structure of binary NPSLs depends on the size ratio of small and large nanoparticles, $\gamma = R_{\text{small}}/R_{\text{large}}$ [140, 141]. The icosahedron-shape gold nanocrystal in our Ag-Au binary NPSL has diameter around 2 nm, containing 309 gold atoms. The silver nanocrystal has diameter around 5 nm and contains 3871 silver atoms. This gives $\gamma \approx 0.4$, which is very close to the most stable value for NaCl-type structure[139]. The gold and silver nanocrystals are both fully passivated by octanethiol ligands. The simulation system, shown in Figure 4-4a, is a $4 \times 4 \times 4$ supercell, containing 256 silver nanoparticles and 256 gold nanoparticles. The simulation set up and procedures for stress-driven fusion of the binary NPSL are similar to those for gold NPSLs discussed earlier.

Figure 4-4a-d show that, if we deform the binary NPSL along the [100] direction of the superlattice under $P = 0$, no ordered fusion of nanoparticles occurs. The system mechanically yields at around $\tau_Y = 90$ MPa before the gold and silver nanocrystal cores were able to jam together to form contact. Accompanied with this yielding, the smaller-sized gold nanoparticles are displaced from their lattice sites along the [100] direction, which is the nearest-neighbor direction in NaCl-type superlattice. In contrast, when the binary NPSL is deformed in the presence of $P = 500$ MPa, the system is superstructurally stiffer and the nanoparticles remain jammed in their

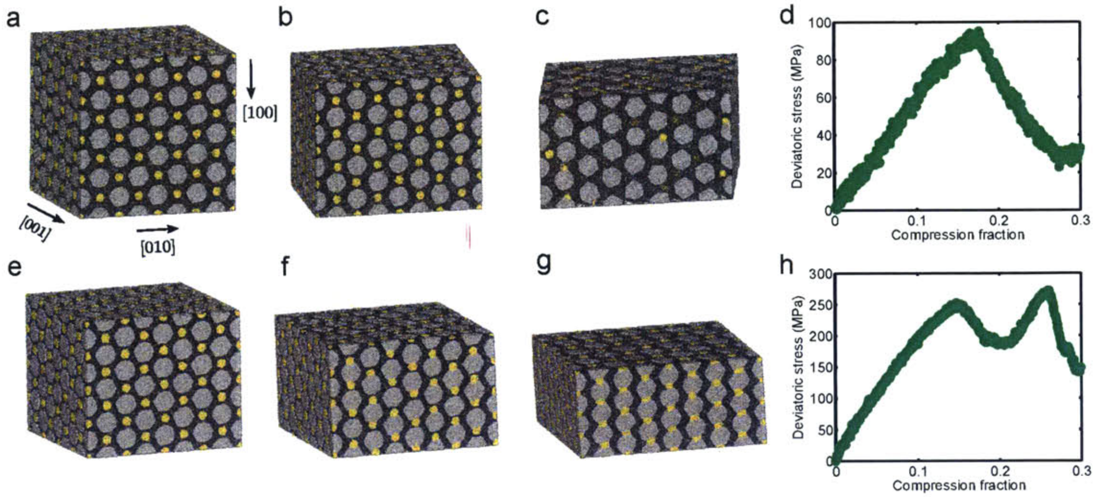

Figure 4-4: Stress-driven fusion of Ag-Au binary NPSL in NaCl-type superstructure. (a)-(c): MD simulation snapshots showing the structural evolution of the system deformed at zero external pressure along the [100] direction. (a) The configuration of the system before uniaxial deformation. The silver nanocrystals are colored in silver and the gold nanocrystals are colored in gold. The black region between the nanocrystals contains thiol molecules adsorbed on the nanocrystal surfaces. (b) and (c): Configurations at strain equal to $-0.15$ and $-0.3$, respectively. (d) Stress-strain curve associated with the deformation at zero external pressure. The yield stress is around 90 MPa. (e)-(g): Structural evolution of the binary NPSL deformed along the [100] direction in the presence of 500 MPa pressure. Multi-junction nanowire array consists of periodic domains of gold and silver nanocrystals are formed at the end of deformation. (h) Stress-strain curve associated with the deformation at 500 MPa pressure. The critical deviatoric stress to induce fusion is around 280 MPa.

lattice sites during deformation. This pressure-induced increase in yield strength $\tau_{\mathrm{Y}}(P > 0) > \tau_{\mathrm{Y}}(P = 0)$, so-called Mohr-Coulomb [142] or non-Schmid yield shown in Figure 4-4d-f, allows the uniaxial stress to rise high enough to drive the fusion of silver and gold nanoparticles along the [100] direction, forming Ag-Au multi-junction nanowires arrays.

### 4.3.4 Mechanistic Understanding of Stress-Driven Fusion

Our simulations of gold NPSLs and Ag-Au binary NPSLs reveal that a few conditions need to be met simultaneously for ordered fusion of nanoparticles in these NPSLs: (a) the presence of a pressure background of more than several hundred MPa. The presence of a moderately high pressure $P$ on the supercrystal, $P > 0.2B$, increases its uniaxial yield strength $\tau_Y$ significantly (Figure 4-3d). The computed finite-pressure elastic constants $C_{11}$, $C_{12}$ and $C_{44}$ of the gold NPSLs also increase significantly (Figure 4-3e). When the mechanical strength of the system is increased such that the yielding deviatoric stress becomes larger than the critical fusion deviatoric stress, $\tau_{\mathrm{Y}}(P) > \tau_{\mathrm{fusion}}(P)$, ordered fusion of NPSL can happen. (b) The applied deviatoric stress needs to be larger than the critical fusion deviatoric stress, $\tau > \tau_{\mathrm{fusion}}$. It can be seen from Figure 4-3d that if the deviatoric stress has not reached the critical value, the system is still in the viscoelasticity regime. Physically, neighboring nanoparticles have not come close enough to enable the contact formation of the nanocrystal cores. (c) Right alignment of the deviatoric stress with respect to the crystallographic direction of the superlattice. Our simulation indicates that proper alignment of deviatoric stress ensures ordered nanoparticle fusion. Formation of nanowire array is found to occur when the deviatoric stress aligns with the nearest-neighbor direction of nanoparticles in NPSLs.

If the fusion criterion is $\tau_{\mathrm{Y}}(P) > \tau_{\mathrm{fusion}}(P)$, what then controls $\tau_{\mathrm{fusion}}$? At molecular level, the mechanism of nanoparticle fusion is deviatoric stress induced ligand displacement on nanocrystal surface, which depassivates the gold nanocrystals locally and allows them to form direct metal-metal contact (grain boundary) and fuse together. The ligands between neighboring nanocrystals along the deviatoric stress direction sustain higher local pressure than ligands elsewhere on the surface, creating chemical potential gradient for ligand surface diffusion. It has been shown recently that surface diffusion on sub-10 nm metallic nanoparticles is so active at room temperature that it can support Coble creep [143, 144]. The large surface curvature of nanocrystal facilitates ligand surface diffusion, as the free volume per ligand is higher on surfaces with higher curvature [145]. If the nanoparticles are continuously pushed toward each other, ligands will eventually leave the contact region (ligand source) to regions of less local pressure (ligand sink), followed by the fusion of gold nanocrystal. This ligand source-to-ligand sink process by surface diffusion is shown in the simulation snapshots of Figure 4-5a. The possibility of ligands being displaced by

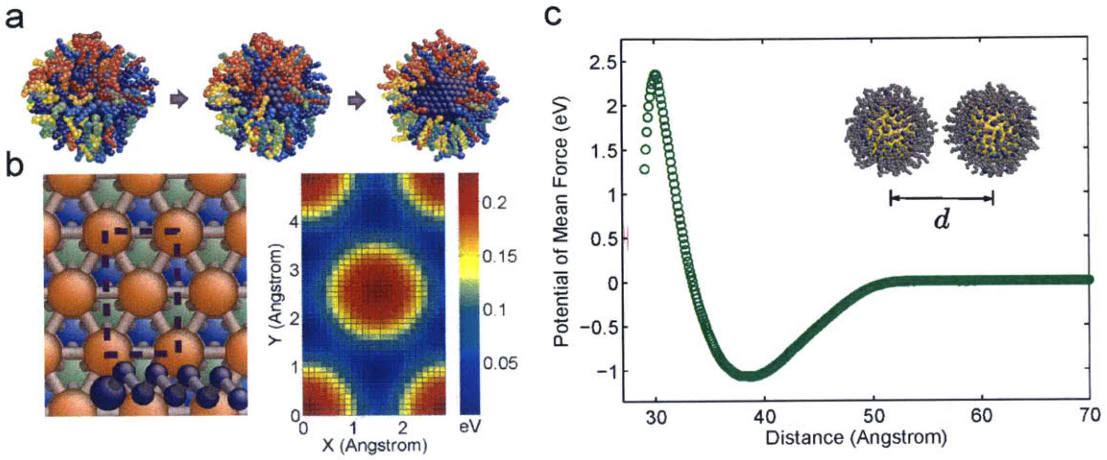

Figure 4-5: (a) Simulation snapshots of ligands being displaced from the contact region between two nanoparticles during stress-driven fusion. Atoms belong to the same ligand molecule are colored the same. (b) Surface configuration of the gold nanocrystal in our model and calculated potential energy surface for moving a ligand on the surface. In the left panel of (b), the top surface layer of the nanocrystal is colored in orange, which is shown together with the two layers beneath (green and blue). A thiol molecule is also depicted in the figure. The dashed box represents the region for potential energy surface calculation, the result of which is shown in the right panel of (b). (c) Calculated potential of mean force as a function of distance between two nanoparticles. The potential of mean force reaches maximum shortly before the fusion of two nanoparticles.

mechanical force on gold surfaces had been unequivocally demonstrated by Liu *et al* [146], where they found the tip of AFM can displace self-assembled thiol layers on gold surfaces above a critical contact pressure around 1 GPa.[147] Due to the aforementioned curvature effects, the critical contact pressure for displacing ligands on nanocrystal surface should be lower, which in our study was found to be several hundred MPa. The calculated potential energy barrier $Q$ for displacing of an single ligand on gold (111) surface is around 50 meV in our simulation (Figure 4-5b), a value that agrees with first-principles calculated thiol diffusion barrier on gold (111) surface [125]. This low energy barrier at $P = 0$ means such surface migration can indeed happen at room temperature [127].

The critical deviatoric stress for fusion of NPSL can be estimated by calculating the free energy barrier of fusion between two individual nanoparticles. The Potential of Mean Force (PMF) between two nanoparticles can be calculated via steered molecular dynamics (SMD)[113]. Based on Jarzynski's equality [148], PMF reflects the free energy difference between the initial and final states during a non-equilibrium process. During our SMD calculation of PMF, two individual gold nanoparticles, initially separated over a distance of 150 Å, are coupled together by a fictitious spring and pulled toward each other with a constant pulling velocity equal to 0.1 Å per picosecond. This pulling speed, when translated into engineering strain rate of deformation, is close to the strain rate we used for stress-driven fusion simulation. The nanoparticles are allowed to rotate freely about their centers of mass during the SMD pulling process. The final PMF is the average of six independent trajectories along the same pulling path. Figure 4-5c shows the calculated PMF. The PMF has a well-defined potential minimum where entropic repulsion between the ligands balances the van der Waals enthalpic attraction. The PMF also has a steep repulsive region, the maximum of which corresponds to the "fusion distance" [113] between two nanoparticles. Two nanoparticles will fuse together when their distance is smaller than the fusion distance. From the computed PMF, the fusion free energy barrier between two nanoparticles is determined to be $\Delta F = 3.5$ eV. This number can be approximated as the free energy barrier of fusion per nanoparticle in the gold NPSL. We can then estimate the minimum deviatoric stress based on the thermodynamic principle that work done on the system must be larger than the free energy change. Assuming linear stress-strain relation, the net work done on the NPSL per particle before fusion is $w = \tau_{\text{fusion}}\varepsilon_c\Omega/2$, where $\varepsilon_c$ is the critical fusion strain, and $\Omega$ is the volume per nanoparticle in the NPSL. We then reach the following inequality:

$$\frac{1}{2}\tau_{\text{fusion}}\varepsilon_c\Omega > \Delta F \tag{4.16}$$

Using the numbers from simulation, $\varepsilon_c \approx 0.2$ and $\Omega \approx 4.5 \times 10^4 \text{Å}^3$ (Figure 4-1b), we calculate the critical deviatoric stress $\tau_{\text{fusion}} > 120$ MPa. This number is close to the critical deviatoric stress obtained from the fusion processing diagram Figure 4-3d (170 MPa). The success of this "independent particle" model suggests that at critical fusion compression $\tau_{\text{fusion}}$, many-body effects on the fusion of nanoparticle in the NPSL are still relatively minor.

We would like to point out that, while we conclude from our simulations that stress-driven fusion of gold NPSLs require pressure and deviatoric stress of order several hundred MPa, these critical values are obtained from simulations with very high strain rate of deformation and very small simulation supercell, thereby may not necessarily reflect the minimum critical stress values to achieve fusion in laboratory experiments with much lower strain rate. Due to the time-scale limit of MD simulation, strain rate in MD simulation are typically very high, ranging from $10^{-1}$ to $10^{-5}$ per picosecond. The strain rate of deformation in our simulation ($1.0 \times 10^{-4}$ per picosecond) is a common value for MD simulation but still many orders of magnitude higher than common experimental strain rate. We have carried out preliminary studies on the effects of strain rate on the critical fusion deviatoric stress, and found lower stress value when strain rate is reduced. This is not surprising considering the NPSLs are viscoelastic. Therefore, the experimental critical fusion pressure and deviatoric stresses could be lower than the values obtained by our simulation, if the interatomic potentials used in our simulation are sufficiently accurate. We also emphasize that, the critical fusion deviatoric stress is not the stress to realize the sintering of bare, unpassivated gold nanocrystals. Instead, the majority of the load in stress-driven fusion was the flow stress to deform and replace the passivating ligands absorbed on the nanocrystal surfaces. Once the ligands are displaced, sintering of gold nanocrystals can happen with much lower applied load. Indeed, Lu *et al* demonstrated that cold welding of gold nanowires can occur with contact pressure less than a few MPa at room temperature [149].

A potentially important implication of our simulation is that stress-driven fusion of NPSLs may only require pressure and deviatoric stress of order several hundred MPa or even lower, in which case special pressure-generating devices such as diamond anvil cell may not be necessary. In Wu *et al*'s high pressure experiment[109], formation of gold nanowire arrays from gold NPSLs occurs at pressure above 10 GPa. This is because the deviatoric stress in their experiment is generated only when the Pressure Transmitting Medium (PTM), namely silicone oil, is solidified in that range of pressure. Yet solidification of PTM is not the only way to generate deviatoric stress. One can directly compress a NPSL sample immersed in a PTM to induce deviatoric stress on top of a compressive pressure. Indeed, hydraulic compression machines, capable of generating axial deviatoric stress while maintaining radial pressure up to 400 MPa, had been used to study the phase transformation of zirconia [150]. Such instruments are clearly more suitable than diamond anvil cell should stress-driven fusion of NPSLs become a viable route for large-scale synthesis of nanowire arrays.

### 4.3.5 Ligand Conformation Change and Displacement During Stress-Driven Fusion

We have studied the conformation change and displacement of ligands on nanocrystal surface during stress-driven fusion along the [110] direction of gold NPSL at 1 GPa pressure. To measure the ligand conformation change, we calculate the angle between ligand end-to-end vector and the unit vector along the deformation direction, as schematically shown in Figure 4-6(a). The end-to-end vector for the $i$-th ligand is defined as $\vec{h}_i = \vec{r}_{i,\mathrm{CH_3}} - \vec{r}_{i,\mathrm{S}}$, where $\vec{r}_{i,\mathrm{CH_3}}$ and $\vec{r}_{i,\mathrm{S}}$ denote the coordinates of the outmost $\mathrm{CH_3}$ structural unit and the sulfur atom, respectively. Defining $\hat{z}$ to be the unit vector along the deformation direction, the angle between $\vec{h}_i$ and $\hat{z}$ is then calculated as $\theta^i = \arccos\left(\vec{h}_i \cdot \hat{z}/|\vec{h}_i|\right)$. The change of $\theta^i$ during deformation would reflect the rotation of the ligand with respect to the deformation direction. We calculate the angle for all ligands in the system at strain zero and strain equal to $-0.2$, and plot their distributions in Figure 4-6(b). It can be seen from the figure that the distribution, centered at 90 degree, becomes narrower when strain goes from zero to $-0.2$. This indicates that the ligands are being pushed away from the deformation direction.

In Figure 4-6(c), we illustrate the measure of ligand displacement on nanocrystal surface. $\vec{d}_i$ is defined to be the vector going from the center of a nanoparticle, on which the $i$-th ligands is adsorbed, to the sulfur atom of that ligand. The location of sulfur atom is considered to be the binding site of the ligand. The projection of $\vec{d}_i$ along the deformation direction $\hat{z}$, written as $d_i^{||}$, can be calculated as $d_i^{||} = \vec{d}_i \cdot \hat{z}$. $d^{||}$

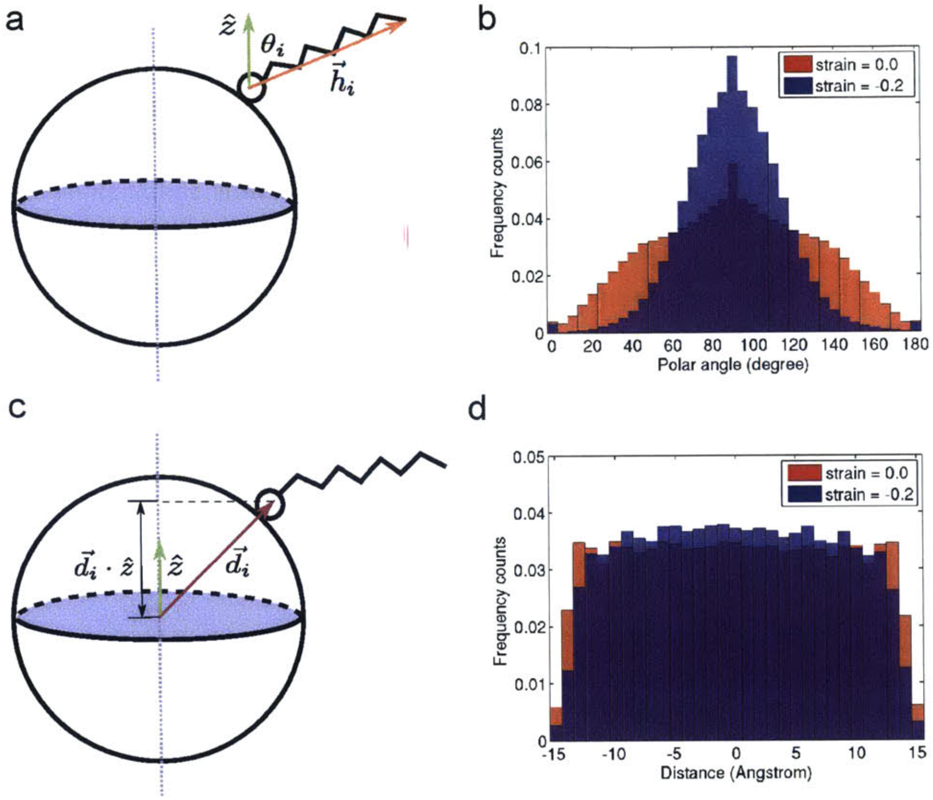

Figure 4-6: Conformation change and displacement of ligands on nanocrystal surface during stress-driven fusion of gold NPSL along the [110] direction of *fcc* superlattice at 1 GPa pressure. (a) Schematic of a ligand adsorbed on the surface of a gold nanocrystal. $\hat{z}$ denotes the unit vector along the direction of uniaxial deformation. $\vec{h}_i$ is the end-to-end vector for the $i$-th ligand; $\theta^i$ denotes the angle between $\hat{z}$ and $\vec{h}_i$. Note the actual shape of the gold nanocrystals is icosahedral, not spherical as we schematically draw here. (b) The distribution of angle $\theta$ for all ligands at strain $\varepsilon = 0$ and $\varepsilon = -0.2$. The red region belongs only to $\varepsilon = 0$, while the blue region belongs only to $\varepsilon = -0.2$. The purple region is the overlap between two distributions. (c) Illustration of quantities defined for studying ligand displacement on nanocrystal surface. $\vec{d}_i$ is the vector from the center of a nanoparticle to the adsorption site of a ligand adsorbed on it. The dot product between $\vec{d}_i$ and the unit vector $\hat{z}$, written as $\vec{d}_i^{||} = \vec{d}_i \cdot \hat{z}$, is a measure of the location of binding site with respect to the center of nanocrystal along the deformation direction. (d) Distributions of $\vec{d}^{||}$ calculated for all ligands at $\varepsilon = 0$ and $\varepsilon = -0.2$.

gives information about the adsorption site of a ligand with respect to the center of nanocrystal along the deformation direction. The distributions of $d^{||}$ for all ligands at strain zero and strain equal to $-0.2$ are shown in Figure 4-6(d). We can see that from strain zero to strain equal to $-0.2$, fewer ligands have adsorption sites near the "south and north poles" of nanocrystals, where ligands are subjected to deformation directly. Simultaneously, more ligands adopt adsorption sites near the "equators" of nanocrystals. This clearly indicates that ligands are being displaced from the contact regions between two nanoparticles along the deformation direction.

## 4.4 Summary and Conclusion

To summarize, we have studied the mechanical response and stress-driven fusion of gold NPSLs and Ag-Au binary NPSLs. We study the conditions under which ordered nanowire array can be formed via stress-driven fusion, and present molecular-level understanding of the fusion process. First, deviatoric (uniaxial) stress $\tau_{\text{fusion}}$ of hundreds of MPa is needed to set up ligand source ligand sink mass action on the surface of the same nanoparticle, with sufficient chemical potential gradient to drive surface diffusion, which is certainly facile enough at room temperature ($Q \sim 50$ meV) if the pressure is not exceedingly high. Second, moderate hydrostatic (triaxial) pressure $P \sim 0.2B(P = 0)$ is necessary to elevate the supercrystal yield strength $\tau_{\text{Y}}$ significantly. This is because the applied deviatoric stress can also be relaxed by superstructural plasticity (dislocation, twinning, phase transformation, etc.) of the supercrystal, and if these processes happen before fusion, it will be difficult to have ordered fusion. These conditions are summarized in a single equation $\tau_{\text{Y}}(P) > \tau > \tau_{\text{fusion}}(P)$, and we have given numerical estimates of both $\tau_{\text{Y}}(P)$ and $\tau_{\text{fusion}}(P)$ in this paper, $\tau_{\text{Y}}(P)$ by Mohr-Coulomb type of calculation, and $\tau_{\text{fusion}}(P)$ by molecular level energy estimates, and direct calculations. Based on these understandings we have constructed a room-temperature processing diagram (Figure 4-3d) that is shown to be effective for both Au and Ag-Au NPSLs. Our study suggests that stress-driven fusion could potentially be employed to create novel nanostructures, such as multi-junction nanowire arrays, in a scalable and cost-effective way. This is an exciting opportunity considering the structural richness and compositional tunability that can be achieved in binary and multi-component NPSLs [103, 151]. Because both $\tau$ and $P$ required are rather low (several hundred MPa), it should then be entirely possible that stress-driven fusion of binary NPSLs could be used for industrial-scale production of multi-junction nanowire arrays, for use in bulk-scale applications such as photovoltaics [152, 153] and catalysis.

# Chapter 5

# Deformation-Driven Diffusion and Plastic Flow in Two-Dimensional Amorphous Granular Pillars

## 5.1 Introduction

Disordered materials such as metallic glasses can exhibit highly localized deformation and shear band formation[154, 155]. Most experiments on these systems, however, use loading geometries in which there are free boundaries and inhomogeneous strains, while simulations have typically focused on systems with periodic boundary conditions under homogeneously-applied shear strain. To understand at a microscopic level the effects of loading geometry on the macroscopic mechanical response, it is useful to study a disordered system in which individual particles can be imaged and tracked as they rearrange under an applied load. In this chapter we introduce a granular packing–a packing of discrete macroscopic particles for which thermal agitation plays a negligible role [156, 157]–in a pillar geometry commonly used for mechanical testing of metallic glasses. We combine experiment and simulation to study the response of these two-dimensional (2D) pillars to athermal, quasistatic, uniaxial compression (the experiments were carried out by our experimental collaborators Jennifer Rieser and Douglas Durian at the University of Pennsylvania).

One question of interest is how the mechanical response of the pillar depends on pillar size. We find that the pillar shape evolves under load in a self-similar fashion, so that the shape of the pillar at a given strain is independent of system size. We also find that as the pillars deform, the strain rate localizes into transient lines of slip, whose thickness of a few particle diameters is independent of system size. Thus, the system is self-similar in shape at the macroscopic scale, but, surprisingly, its yielding is not self-similar at the microscopic scale.

A second question concerns the random motions of particles as they rearrange under inhomogeneous loading conditions. Because particles jostle each other, they display diffusive behavior in homogeneously sheared systems that are devoid of random thermal fluctuations [158]. Recently, crystal nucleation and growth were observed *in situ* in mechanically fatigued metallic glasses at low temperature [159]. Crystallization is typically thought to require diffusion. Therefore, it was suggested that the "shear transformation zones" (STZs) [155] should be generalized to "shear diffusion transformation zones" (SDTZs) [159], to reflect the contributions of random motions driven by loading, even under inhomogeneous conditions. Our amorphous granular pillar is an athermal system as far as the macroscopic particles are concerned (effective vibrational temperature $\approx 0$), so our experiment and simulations can examine how inhomogeneous loading affects particle motion. We find that the idea of load-induced diffusion can be generalized to inhomogeneous loading by replacing time with the cumulative deviatoric strain, and the mean-squared displacement with the mean-squared displacement of a particle relative to the best-fit affine displacement of its neighborhood (*i.e.* the mean-squared non-affine displacement [42]). With this generalization, we observe that the mean-squared non-affine particle displacement crosses over from ballistic to diffusive behavior as a function of the cumulative deviatoric strain.

## 5.2 Methods

The compacted 2D amorphous granular pillars in our study consist of 50-50 mixture of bidisperse cylindrical particles (grains) standing upright on a substrate. A top-view of the schematic setup is shown in Fig. 5-1. The pillars have aspect ratio $H_0/W_0 \approx 2$, where $H_0$ and $W_0$ are the original height and width of the pillars respectively. In our experiment, the cylindrical granular particles are made of acetal plastic. The diameter of the large grains in the pillars, denoted by $D$, is 1/4 inch (0.635 cm), while for the small grains the diameter $d$ has the value of 3/16 inch (0.47625 cm). The ratio of diameter between large and small grains is therefore $D/d = 4/3$. Both types of grains are 3/4 inch (1.905 cm) tall. The masses for the large and small grains are 0.80 gram and 0.45 gram respectively. The pillars are confined between a pair of parallel bars. The bottom bar is static while the top bar deforms the pillars uniaxially with a slow, constant speed $v_c = 1/300$ inch per second (0.0084667 cm/sec). The force sensors connected to the bars measure the forces on the top and the bottom bars, and the trajectory of each particle in a pillar is tracked by a high-speed camera mounted above the pillar. The basic parameters in our simulation, including the size and mass of the grains, as well as the velocity of the bars, are the same as in the experiment.

### 5.2.1 Packing Generation Protocol

Properly prepared initial configurations are crucial for the study of the mechanical properties of amorphous solids. In our experiment, 50-50 random mixture of bidisperse grains are compacted to form a pillar with aspect ratio 2 to 1. To facilitate direct comparison between experiment and simulation, for small-sized pillars (number of grains in the pillar $N = 1000$), the simulation initial conditions are taken from the experimental data, which are then relaxed in simulation to avoid particle overlapping resulted from measurement error. For large-sized pillars, which can only be studied by simulation, we generate compacted, amorphous granular pillars through computer simulation, using the protocol described below. The particle area density in the simulation-generated pillar is controlled to be at the onset of jamming tran-

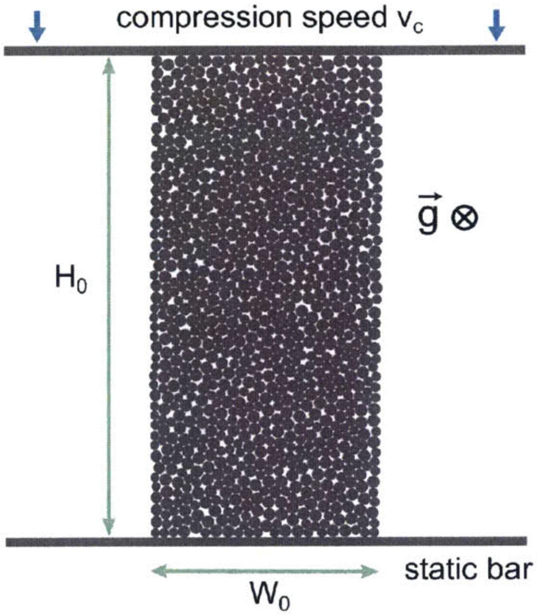

Figure 5-1: Top-view of the experimental/simulation setup. A two-dimensional pillar of granular particles on a frictional substrate are deformed quasistatically and uniaxially by a rigid bar from one side. The direction of gravity is perpendicular to the substrate. The compacted, disordered granular packing consists of 50-50 mixture of bidisperse cylindrical-shape grains. The ratio of radius between large and small grains is 4:3. The aspect ratio of the pillar, defined as the initial height of the pillar ($H_0$) divided by the initial width ($W_0$), is 2:1. The pillar is confined between two rigid bars placed at the top and bottom end of the pillar respectively. The top bar deforms the pillar with a constant speed $v_c$ while the bottom bar is kept static.

sition [160]. To generate the initial conditions, we assign the following truncated Lennard-Jones potential with purely repulsive interaction to the large (L) and small (S) grains

$$U_{\alpha\beta}(r) = \begin{cases} \epsilon\left[(\sigma_{\alpha\beta}/r)^{12} - 2\,(\sigma_{\alpha\beta}/r)^{6}\right] & \text{for } r < \sigma_{\alpha\beta}, \\ -\epsilon & \text{for } r \geq \sigma_{\alpha\beta}, \end{cases} \tag{5.1}$$

where the subscripts $\alpha$, $\beta$ denote L or S. The zero-force cut-off distances $\sigma_{\alpha\beta}$ are chosen to be the sum of radii of two particles in contact, namely $\sigma_{\mathrm{LL}} = D$, $\sigma_{\mathrm{LS}} = 7D/8$, and $\sigma_{\mathrm{SS}} = 3D/4$, where $D$ is the diameter of a large grain. We note that this potential will only be used to generate the initial conditions of the granular packings, and is different from the particle interaction model we describe later for the deformation of the granular pillars.

To create a disordered granular packing with 50-50 mixture of $N$ total number of large and small grains, a rectangular simulation box with dimensions $\Lambda \times 2\Lambda$ is initially created, where the width of the box $\Lambda$ is chosen such that the initial particle area density, $\rho = N/2\Lambda^2$, is slightly above the particle overlapping threshold. We then randomly assign the positions of the particle within the simulation box, and subsequently use conjugate-gradient (CG) method to minimize the total potential energy of the system. Periodic boundary conditions are applied during this process. The particle positions are adjusted iteratively until the relative change of energy per particle between two successive CG steps is smaller than $10^{-12}$. When this stage is reached, the pressure of the system is calculated using the following virial formula

$$p = -\frac{1}{2A}\sum_{i>j} r_{ij}\frac{dU}{dr_{ij}}, \tag{5.2}$$

where $A$ is the area of the simulation box, $r_{ij}$ is the distance between particles $i$ and $j$. If the pressure is greater than zero, both dimensions of the simulation box will be enlarged by a fraction of $10^{-5}$, and the particles in the box will be mapped to the corresponding new positions in the enlarged box via affine transformation. CG energy minimization will then be carried out on the new configuration. This iterative process stops when the calculated pressure of the system at the end of a CG run becomes smaller than $10^{-10}\epsilon/D^2$. The final configuration will be taken as the initial conditions of close-packed 2D amorphous granular assembly. Vacuum space is then added on the lateral sides of simulation box to create a pillar with 2:1 aspect ratio. Calculation of radial distribution functions for different-sized pillars indicates that the structure of the amorphous assemblies generated following the above procedures does not show noticeable size dependence. Comparison of the radial distribution functions computed for the experimental and simulation-generated initial conditions is shown in Fig. 5-2.

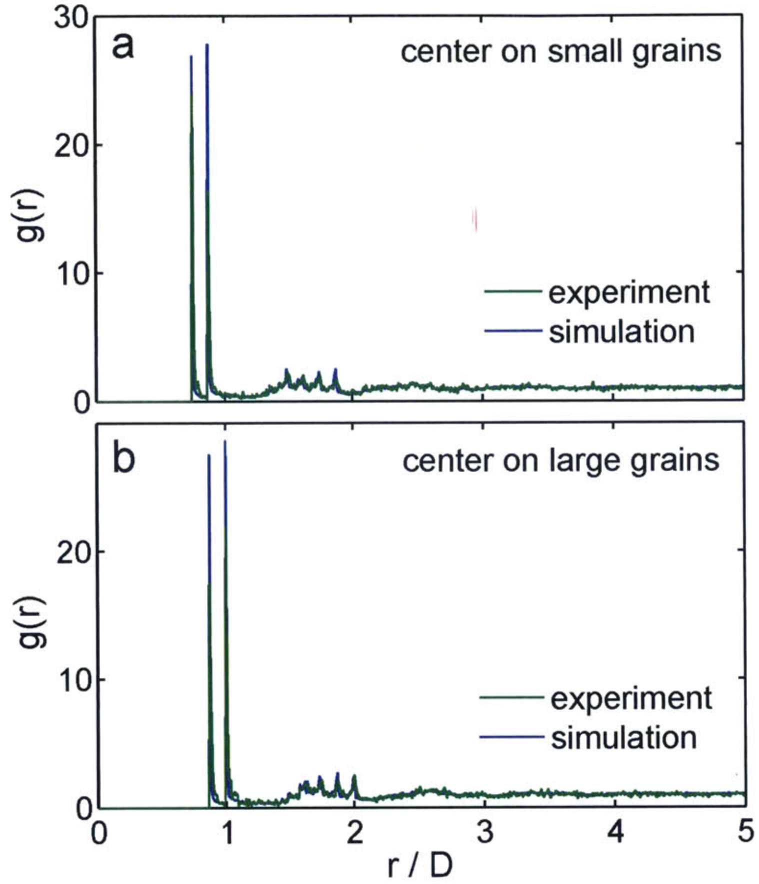

Figure 5-2: Comparison of the radial distribution functions $g(r)$ for experiment-derived and simulation-generated initial conditions computed using (a) small grains as the central particles and (b) larger grains as the central particles are shown respectively. The distance $r$ is scaled by the diameter $D$ of the large particles.

### 5.2.2 Simulation Methodology

We use the method of MD to simulate the quasistatic deformation of the 2D granular pillars. The simulation force model includes three components: the grain-grain interaction, the grain-bar interaction and the grain-substrate interaction. Each of these forces will be described in the following.

#### Grain-Grain Interaction

As illustrated in Fig. 5-3a, the interaction between two grains includes normal and tangential contact force, which are denoted by $\mathbf{F}_n$ and $\mathbf{F}_t$ respectively. Two grains

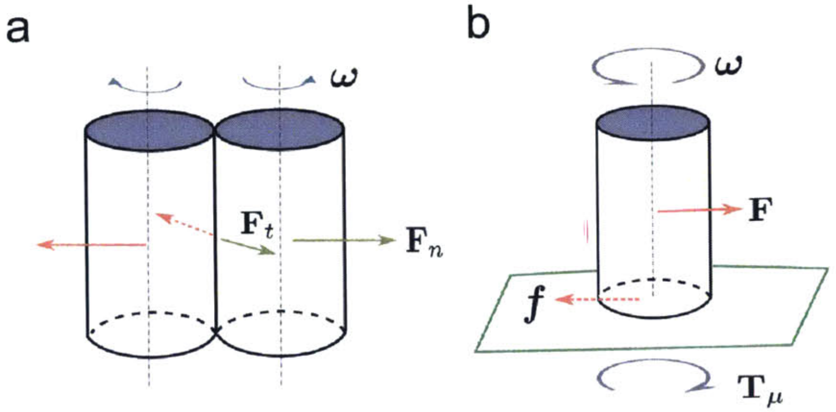

Figure 5-3: (a) Illustrations of grain-grain interaction in the granular pillar. The contact force between two grains consists of normal repulsive contact force $\mathbf{F}_n$ and tangential shear contact force $\mathbf{F}_t$. (b) Illustration of grain-substrate interaction. If the velocity of a grain $i$ is non-zero, or the vector sum of the forces on the grain due to other grains and the bars is non-zero, the substrate will exert a frictional force $\mathbf{f}$ on the grain, the maximum value of which is $m_i g \mu$, where $m_i$ is the mass of the particle, $g$ is the gravity acceleration constant and $\mu$ denotes the friction coefficient between the grain and the substrate. Likewise, if the angular velocity of the grain is non-zero or the torque on the grain due to other interactions is non-zero, the substrate will induce a frictional torque whose maximum magnitude is $|\mathbf{T}_{\mu,i}| = \frac{2}{3} m_i g \mu R_i$, where $R_i$ is the radius of the particle.

experience a repulsive normal contact force if the distance between the particle centers is smaller than the sum of their radii. For two smooth, elastic cylindrical particles with parallel axes, the normal contact force as determined by the Hertzian theory of contact mechanics is proportional to the indentation depth between the two particles [161]. For our granular particles, denote by $\mathbf{r}_i$ and $\mathbf{r}_j$ the positions of particles $i$ and $j$, and denote by $\mathbf{r}_{ij} = \mathbf{r}_i - \mathbf{r}_j$ the distance vector between the two particles, the indentation depth $\delta_{ij}$ is calculated as

$$\delta_{ij} = R_i + R_j - r_{ij}, \tag{5.3}$$

where $r_{ij} = |\mathbf{r}_{ij}|$. $R_i$ and $R_j$ are the particle radius of $i$ and $j$ respectively. $\delta_{ij}$ will be zero if the two particles are not in contact. The normal contact force acting on the particle $i$ by particle $j$ is then given by

$$\mathbf{F}_{n_{ij}} = k_n \delta_{ij} \mathbf{n}_{ij}, \tag{5.4}$$

where $\mathbf{n}_{ij} = \mathbf{r}_{ij}/r_{ij}$, and $k_n$ is the normal contact stiffness. The corresponding normal contact force on particle $j$ is given by Newton's third law, namely, $\mathbf{F}_{n_{ji}} = -\mathbf{F}_{n_{ij}}$. In Hertzian theory of contact mechanics [161], the constant $k_n$ for two cylinders in contact can be calculated as

$$k_n = \frac{\pi}{4} E^* l, \tag{5.5}$$

where $l$ is the height of the cylinders. $E^*$ is the normalized contact elastic modulus, which is computed from the respective elastic modulus of the two cylinders, $E_1$ and $E_2$, and their Poisson's ratios, $\nu_1$ and $\nu_2$:

$$\frac{1}{E^*} = \frac{1-\nu_1^2}{E_1} + \frac{1-\nu_2^2}{E_2}. \tag{5.6}$$

The existence of a friction force between two particles in contact is a characteristic feature of granular materials. Appropriate modeling of contact friction is crucial to the study of granular dynamics. The tangential frictional force between two grains in contact can be very complicated in reality [162]. We adopt the history-dependent shear contact model initially developed by Cundall and Strack [163]. This well-tested model has been used by many others to model the dynamics of granular assemblies [162, 164, 165, 166, 167, 168, 169, 170, 171, 172]. The essence of this model is to keep track of the elastic shear displacement of two particles throughout the lifetime of their contact, and applying the Coulomb elastic yield criterion when the displacement reaches a critical value. Our implementation of the Cundall-Strack model follows Silbert *et al.* [162]. Specifically, the tangential contact force between particle $i$ and $j$ is calculated as:

$$\mathbf{F}_{t_{ij}} = -k_t \mathbf{u}_{t_{ij}}, \tag{5.7}$$

where the shear displacement $\mathbf{u}_{t_{ij}}$ is obtained by integrating the tangential relative velocities of the two particles during the lifetime of their contact [162]. Here $k_t$ is the tangential contact elastic modulus. It is taken to be proportional to the normal contact stiffness $k_n$. Following Silbert *et al.*, we choose $k_t = \frac{2}{7}k_n$. Previous studies showed that the dynamics of system is relatively insensitive to this parameter [162], which is confirmed by our own simulation.

To model the elastic yield of shear contact, the magnitude of $\mathbf{u}_{t_{ij}}$ is truncated to satisfy the Coulomb yield criterion $|\mathbf{F}_{t_{ij}}| \leq |\mu_g \mathbf{F}_{n_{ij}}|$, where $\mu_g$ is the friction coefficient between the grains.

The tangential contact force will induce torques on the two grains in contact, as given by

$$\mathbf{T}_{ij} = -\frac{1}{2}\mathbf{r}_{ij} \times \mathbf{F}_{t_{ij}}. \tag{5.8}$$

Here $\mathbf{T}_{ij}$ is the torque exerted by grain $j$ on grain $i$ due to the tangential contact force $\mathbf{F}_{t_{ij}}$.

### Grain-Bar Interaction

The grain-bar interaction is modeled in a similar way to the grain-grain interaction. The bar is essentially treated as a rigid grain with infinitely large radius. When a grain comes in contact with a bar, the grain can experience normal and shear contact force induced by the bar, and the shear contact force is also calculated by tracking the elastic shear displacement between the grain and the bar. The motion of the moving bar is not affected by the grains. The static bar at the bottom side of the pillar is always static, while the top bar deforms the pillar at a constant speed $v_c$. Compared to grain-grain interaction, the interaction parameters between the grains and the bar is slightly modified. Since the bars are modeled as rigid bodies that cannot be elastically deformed, it means that the elastic modulus of the bars is considered to be infinite. Consequently, the effective interaction modulus $E^*$ between the bars and the grains, based on Eq. 5.6, is twice as large as that between the grains. Therefore, from Eq. 5.5, the normal interaction stiffness between the bars and the grains is twice as large as that between the grains, i.e., $k_n(\text{grain-bar}) = 2k_n(\text{grain-grain})$. Since the shear modulus of contact $k_t$ is proportional to $k_n$, we have $k_t(\text{grain-bar}) = 2k_t(\text{grain-grain})$

as well.

### Grain-Substrate Interaction

The effect of the substrate on the grains is determined after all the forces and torques on each grain due to other grains and bars have been determined. The substrate can induce both frictional force and torque on the grains, as illustrated in Fig. 5-3b. If a grain is initially static, unless the magnitude of total force due to other grains/bars is larger than the maximum frictional force that can be exerted by the substrate $|\mathbf{f}_i| = m_i g \mu$, the substrate frictional force will cancel out other forces on the grain and the particle will continue to have zero velocity. Here $m_i$ is the mass of the grain $i$, $g$ is the gravitational acceleration and $\mu$ denotes the frictional coefficient between the grains and the substrate. In another case, if the velocity of the grain is non-zero, the substrate will induce a frictional force opposite to the direction of particle motion, with magnitude $|\mathbf{f}_i| = m_i g \mu$. A similar algorithm applies to the rotational motion of a particle. An initially static grain will not start to rotate unless the torque due to other interactions surpasses the maximum substrate-induced frictional torque $|\mathbf{T}_{\mu_i}| = \frac{2}{3} m_i g \mu R_i$, where $R_i$ is the radius of the cylindrical-shape particle. The prefactor $\frac{2}{3}$ is based on the assumption that frictional force is evenly distributed on the circular contact interface between a cylindrical-shape grain and the substrate. If the angular velocity of the grain is non-zero, a frictional torque

$$\mathbf{T}_{\mu,i} = -\frac{2}{3} m_i g \mu R_i \hat{\boldsymbol{\omega}}_i, \tag{5.9}$$

will slow down the rotational motion of the particles, where $\hat{\boldsymbol{\omega}}_i = \boldsymbol{\omega}_i / |\boldsymbol{\omega}_i|$ and $\boldsymbol{\omega}_i$ denotes the angular velocity of particle $i$.

### Equations of Motion

After all the forces and torques on an individual grain are determined, they are summed up and the velocities and angular velocities of the grains are then updated according to Newtonian equations of motion:

$$m_i \frac{d^2 \mathbf{r}_i}{dt^2} = \mathbf{F}_i, \qquad I_i \frac{d\boldsymbol{\omega}_i}{dt} = \mathbf{T}_i, \tag{5.10}$$

where $\mathbf{F}_i$ and $\mathbf{T}_i$ are the total force and torque on the particle $i$ respectively. $I_i = \frac{1}{2} m_i R_i^2$ is the moment of inertia for grain $i$. The standard velocity Verlet integrator is used to update the positions and velocities of the particles, while a finite difference method is used to integrate the first-order differential equation for the angular velocities.

There is a subtle numerical issue that must be addressed when modeling velocity and angular velocity changes of the particles in the presence of the damping effects of a frictional substrate. In numerical integration of equation of motion, time is discretized into small timesteps with each timestep being a small increment $\delta t$. To complete the simulation within a reasonable time frame, $\delta t$ cannot be too small, which means that the changes of velocity and angular velocity of the grains due to the substrate induced force and torque within a timestep are not infinitesimal. Hence, the motion of particles might not be able to be brought to a halt by the substrate – the velocity and angular velocity of the particles could oscillate around the zero. Consider, for example, a stand-alone cylindrical grain with initial velocity $\mathbf{v}_i$ and angular velocity $\boldsymbol{\omega}_i$. Without other interactions, the substrate will induce friction $|\mathbf{f}_i| = m_i g\mu$ and frictional torque $|\mathbf{T}_{\mu,i}| = 2m_i g\mu/3$ on the grain, which slows down the translational and rotational motion of the grain respectively. According to the equations of motion in Eq. 5.10, the translational and rotational acceleration will be $a_v = g\mu$ and $a_\omega = 4g\mu/(3R_i)$, with $R_i$ being the radius of particle $i$. Hence, within a timestep $\delta t$, the change of velocity or angular velocity is a finite number: $\delta v = g\mu\delta t$, $\delta\omega = 4g\mu\delta t/(3R_i)$. If the velocity or angular velocity have been damped to values below these two numbers, they cannot be damped further but instead oscillate around zero, which is clearly a numerical artifact. To work around this issue, we introduce two small parameters

$$\xi_v = g\mu\delta t, \quad \xi_{\omega_i} = \frac{4g\mu}{3R_i}\delta t, \tag{5.11}$$

such that when $|\mathbf{v}_i| < \xi_v$ and $|\sum_j \mathbf{F}_{ij} + \mathbf{F}_i^{\rm bar}| \leq m_i g \mu$ are both satisfied, the velocity and total force on the particle will be set to zero. Here $\mathbf{F}_{ij}$ is the force of particle $j$ on particle $i$, and $\mathbf{F}_i^{\rm bar}$ is the force of the bars on particle $i$. Similarly, for the rotational motion, if $|\boldsymbol{\omega}_i| < \xi_{\omega_i}$ and $|\sum_j \mathbf{T}_{ij} + \mathbf{T}_i^{\rm bar}| \leq \frac{2}{3} m_i g \mu R_i$, the angular velocity and total torque of the particle is set to zero.

### 5.2.3 Choice of Simulation Model Parameters

The independent parameters in the interaction model of our simulation include the grain-grain stiffness $k_n$, grain-grain friction coefficient $\mu_g$, grain-substrate friction coefficient $\mu$, and the timestep for integration of equations of motion $\delta t$. Among these parameters, $\mu$ has been experimentally measured to be around 0.23. Hence $\mu = 0.23$ will be adopted in our simulations. The grain-grain friction coefficient $\mu_g$ is unknown. We have carried out simulation using multiple values of $\mu_g$, and the results indicate that choosing $\mu_g = 0.2$ can achieve good match between the experiment and simulation. Due to the quasistatic nature of deformation by the moving bar on the pillars, the increment of force on a grain by the bar within one timestep $\delta t$ must be much smaller than the maximum static friction by the substrate on a grain, namely

$$2 k_n v_c \delta t \ll m_i g \mu, \tag{5.12}$$

where $v_c$ is the speed of the top moving bar. Hence, the smaller the value of $\delta t$, the higher the value of $k_n$ that can be adopted in simulation. While there is no physical reason for a lower bound of $\delta t$, smaller $\delta t$ results in an increased time span to complete simulation. Realistic consideration leads to our choice of $\delta t = 10^{-5}$ second. The upper bound of allowed $k_n$ calculated from Eq. 5.12 is considered to be smaller than the real contact stiffness of two particles in experiment. For this reason, we have systematically studied the influence of $k_n$ on the simulation results in a small-sized pillar containing 1000 grains. The relatively small sized pillar allows us to use $\delta t = 10^{-6}$ second and thus access a wider range of $k_n$, from $k_n = 1$ N/mm to $k_n = 100$ N/mm. The results indicate that the statistical behaviors of deformation dynamics, such as flow stress and particle-level deformation characteristics, are not significantly influenced by the value of the $k_n$. We therefore choose $k_n = 10$ N/mm and $\delta t = 10^{-5}$ in our simulation.

The results of our study will be expressed in terms of several characteristic units. Length will be expressed in the diameter of the large grains $D$ or the radius $R = D/2$. The unit of velocity will be the bar speed $v_c$ and the unit of time will be $R/v_c$, which is the time it takes for top bar to move over a distance equal to $R$. The units for force and stress will be $mg\mu$, $mg\mu/D$ respectively, where for convenience, we will use the symbol $m$ to denote the mass of a large grain. $mg\mu$ is thus the minimum force to induce the translational motion of a stand-alone large grain and $mg\mu/D$ is the corresponding averaged stress of the bar on the grain.

## 5.3 Combined Experiment and Simulation on Deformation of Small-Sized Pillars

Deformation of an $N = 1000$ pillar has been studied by both experiment and simulation. The experimental initial particle arrangement in the pillar is the same as those depicted in Fig. 5-1. To facilitate comparison between experiment and simulation, our parallel simulation of pillar deformation uses the experimentally measured initial conditions, which were further relaxed in simulation to avoid particle overlapping resulted from measurement error. When the pillar is deformed by the moving bar, the strain of deformation $\varepsilon$ is defined as the change of pillar height $\Delta H$ divided by the original height of the pillar $H_0$, namely, $\varepsilon \equiv \Delta H/H_0$. The deformation stress $\sigma$ is calculated as the normal force on the top moving bar $F_{\text{bar}}$ divided by the maximum width of the pillar near the top edge $W$, namely $\sigma \equiv F_{\text{bar}}/W$.

Fig. 5-4 shows the experimental and simulation stress-strain curve of the $N = 1000$ pillar. The measured stress shows yielding behavior when the deformation strain exceeds a very small value $\varepsilon_y$. From our simulation, we find that the yield strain $\varepsilon_y$ in general becomes smaller as the grain-grain stiffness $k_n$ or the packing density of the

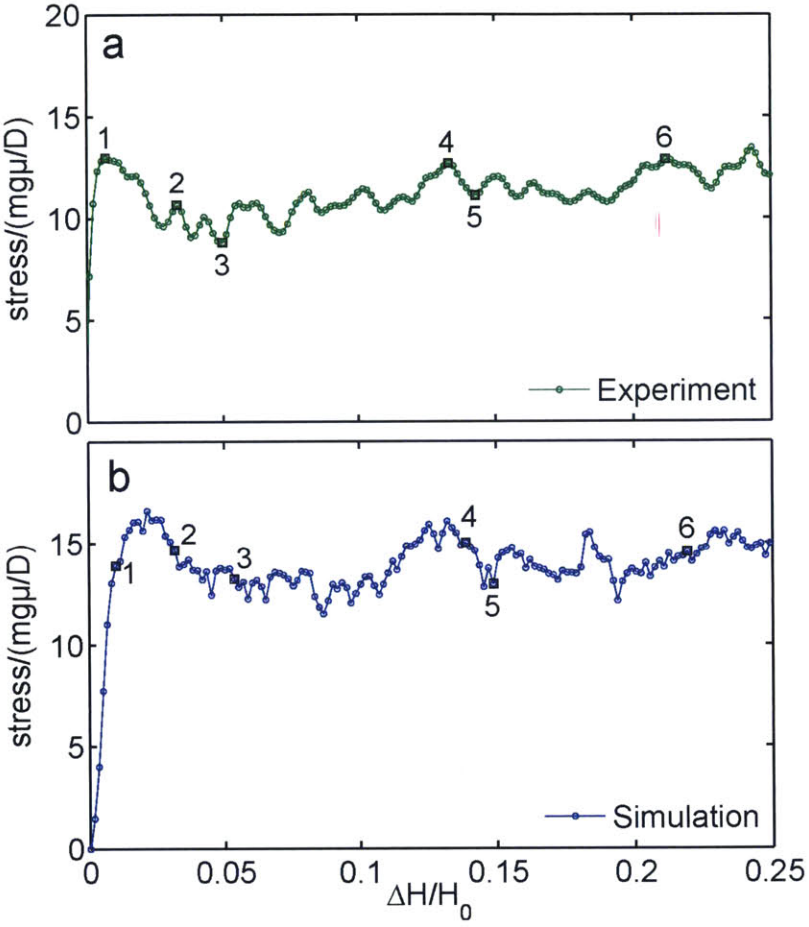

Figure 5-4: Comparison between the (a) experimental and (b) simulation stress-strain curves for the deformation of a $N = 1000$ granular pillar. The compressing stress is measured in units of $mg\mu/D$, while the strain is computed as the change of pillar height ($\Delta H$) divided by the original height of the pillar $H_0$. The special labels (1-6) indicate the stress strain values at which deformation characteristics in the pillar will be compared side to side between experiment and simulation.

pillar is increased. The yield stress $\sigma_y$ however shows little dependence on $k_n$. The parameter that affects $\sigma_y$ most was found to be the grain-grain friction coefficient $\mu_g$. In the range of $\mu_g$ we have studied ($\mu_g$ from 0 to 0.3), $\sigma_y$ increases monotonically with the increase of $\mu_g$. The simulation results presented in this paper use $\mu_g = 0.2$, which was found to achieve overall good match between the experiment and simulation.

In Fig. 5-4, we label several stress/strain values and calibrate the corresponding particle-level structural changes in the pillar. The experimental and simulation results are then compared side-to-side in Fig. 5-5. Fig. 5-5a shows the mean particle velocity field in the pillar at six different stages of deformation. The mean velocity of a particle $i$, denoted by $v_i(t, \Delta t)$, is calculated as the average displacement magnitude of the particle from current time $t$ to a later time $t + \Delta t$,

$$v_i(t, \Delta t) = |\mathbf{r}_i(t + \Delta t) - \mathbf{r}_i(t)|/\Delta t, \tag{5.13}$$

where the value of time interval $\Delta t$ is chosen to be $2/15\ R/v_c$ for the present purpose. $v_i(t, \Delta t)$ contains information of the absolute amount of displacement of the particle $i$ within $\Delta t$. As shown in Fig. 5-5a, the mean velocities of the particles near the moving bar are close to $v_c$, which is expected as the pillar is deformed quasistatically by the bar. The mean velocity of a particle in general becomes smaller as the particle is further away from the moving bar. At the early stages of deformation, particles at the bottom part of the pillar have not moved and therefore have zero values of $v$. A sharp boundary between the moving and non-moving regions of the pillar often forms along the the direction that is roughly 45 degree to the direction of uniaxial deformation.

In the simulations we have access to detailed information on the inter-particle interactions. In Fig. 5-6 we plot the grain-grain normal force $F_n$, tangential force $F_t$ and substrate-induced force frictional force $f$ on the particles at six stages of deformation corresponding to the special labels in Fig. 5-4. Comparing Fig. 5-6a with Fig. 5-6b and Fig. 5-6c, we find that $F_n$ is in general much larger than $F_t$, which is further larger than $f$, namely $F_n \gg F_t \gg f$. In particular, Fig. 5-6a shows that particles with large $F_n$ are connected with force chains. The magnitude of forces in these force chains is higher for particles residing in the interior the pillar. This indicates that the stress in the pillar is rather inhomogeneous, with larger stresses in the interior region of the pillars than close to the surface.

We further look at the rearrangement of particles in the pillar by defining a neighbor sampling distance $R_c$, and calculate the affine transformation strains and non-affine displacements of the particles with respect to their neighbors within $R_c$. The

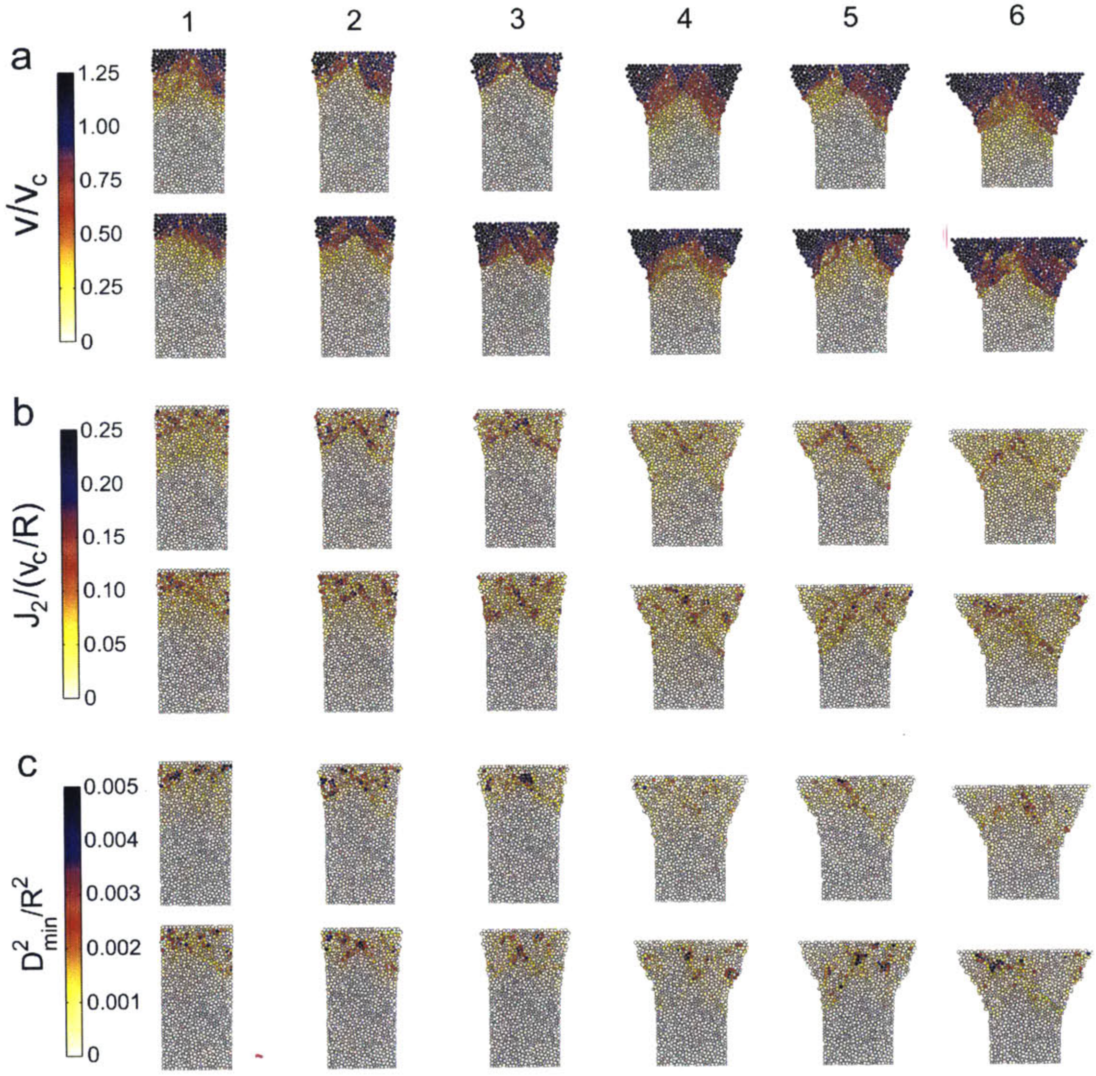

Figure 5-5: Comparison between experiment and simulation of the particle velocity $v$, deviatoric strain rate $J_2$ and non-affine displacement $D^2_{\mathrm{min}}$ during deformation of a $N = 1000$ granular pillar. The six stages of deformation (1-6) correspond to the stress and strain values labeled in Fig. 5-4. Within each subplot (a), (b) and (c), the top panel corresponds to the experimental result, while the bottom panel corresponds to the simulation result. (a) Velocities of the particles in the pillar. The magnitude of the displacement of a particle from the current position after time interval $\Delta t = (2/15)R/v_c$ is divided by $\Delta t$ to obtain the average velocity across the time interval. (b) Deviatoric strain rate $J_2$ for each particle. $J_2$ is computed by comparing the current configuration of a particle and its neighbors with the configuration after $\Delta t$, using neighbor sampling distance $R_c = 1.25D$. $J_2$ is measured in the unit of $v_c/R$. (c) Non-affine displacement $D^2_{\mathrm{min}}$ for each particle in the pillar. The procedures for calculating $D^2_{\mathrm{min}}$ are discussed in the main text.

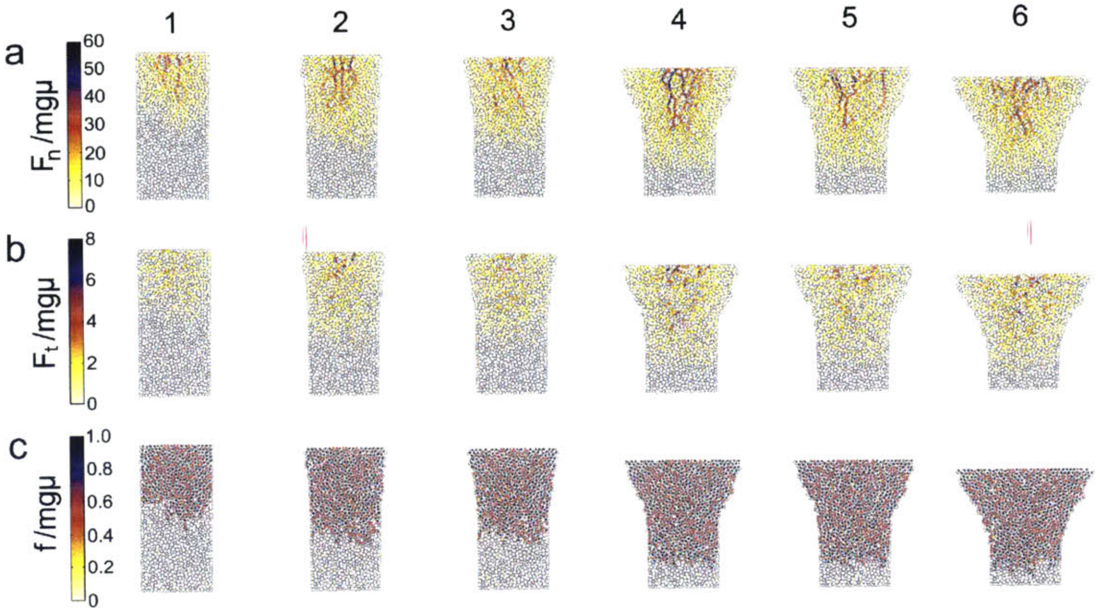

Figure 5-6: Forces in the granular pillar during deformation as obtained from simulation. The special labels (1-6) correspond to the deformation stages labeled in Fig. 5-4b. (a) Grain-grain normal force $F_n$; (b) grain-grain tangential force $F_t$ and (c) grain-substrate friction force $f$. The forces are measured in the unit of $mg\mu$, which is the largest possible value of substrate induced friction on a large grain.

value of $R_c$ is chosen to be $1.25D$, which roughly corresponds to the average first nearest-neighbor distance of the particles in the pillar, as can be seen from the computed radial distribution functions in Fig. 5-2. A particle $j$ is considered to be the neighbor of a particle $i$ if their distance is smaller than $R_c$, which is illustrated in Fig. 5-7. The configurations of the particle $i$ and its neighbors at a given time $t$ and a subsequent time $t + \Delta t$ will then be used to compute the best-fit local affine transformation matrix $\mathbf{J}$ and the non-affine displacement $D^2_{\min}$ associated with particle $i$, using the method introduced by Falk and Langer [42, 43]. Specifically, $D^2_{\min,i}$ is obtained by calculating the best affine transformation matrix $\mathbf{J}_i$ that minimizes the error of deformation mapping:

$$D^2_{\min,i}(t, \Delta t) = \frac{1}{N_i} \min_{\mathbf{J}_i} \sum_{j \in N_i} \left[\mathbf{r}_{ji}(t + \Delta t) - \mathbf{J}_i \mathbf{r}_{ji}(t)\right]^2, \tag{5.14}$$

where $\mathbf{r}_{ji}(t) = \mathbf{r}_j(t) - \mathbf{r}_i(t)$ is the distance vector between particles $j$ and $i$ at time

$t$. $\mathbf{r}_{ji}(t+\Delta t)$ is the distance vector at a later time $t+\Delta t$. The summation is over the neighbors of particle $i$ at time $t$, whose total number is given by $N_i$. The best-fit affine transformation matrix $\mathbf{J}_i(t,\Delta t)$ is usually non-symmetric due to the presence of rotational component. A symmetric Lagrangian strain matrix $\boldsymbol{\eta}_i$ can be calculated from $\mathbf{J}_i$ as

$$\boldsymbol{\eta}_i = \frac{1}{2}\left(\mathbf{J}_i^T \mathbf{J}_i - \mathbf{I}\right), \tag{5.15}$$

where $\mathbf{I}$ is an identity matrix. The hydrostatic invariant is then computed from $\boldsymbol{\eta}_i$ as

$$\eta_i^m = \frac{1}{2}\mathrm{Tr}\boldsymbol{\eta}_i. \tag{5.16}$$

The shear (deviatoric) invariant is then given by

$$\eta_i^s = \sqrt{\frac{1}{2}\mathrm{Tr}\left(\boldsymbol{\eta}_i - \eta_i^m \mathbf{I}\right)^2}. \tag{5.17}$$

Hereafter we will refer to $\eta_i^s(t,\Delta t)$ as the deviatoric strain associated with the particle $i$ from $t$ to $t+\Delta t$. The deviatoric strain rate, denoted by $J_2$, is the normalization of $\eta_i^s(t,\Delta t)$ with respect to $\Delta t$:

$$J_2(t,\Delta t) = \eta^s(t,\Delta t)/\Delta t \tag{5.18}$$

Fig. 5-5b-c shows the computed deviatoric strain rate $J_2$ and $D^2_{\mathrm{min}}$ for each particle in the pillar at six different stages of deformation, where the experimental and simulation results are compared side to side. $J_2(t,\Delta t)$ and $D^2_{\mathrm{min}}(t,\Delta t)$ are computed using $\Delta t = (2/15)R/v_c$, which is the same as the value of $\Delta t$ used for computing the mean velocities of the particles in Fig. 5-5a. Comparing Fig. 5-5b with Fig. 5-5a, it can be seen that large values of deviatoric strain rate occur at places where the gradient of mean velocity, and hence the gradient of particle displacement, is large, which is understandable as strain is a measure of displacement gradient. One can also notice from Fig. 5-5b the presence of thin shear lines in the pillars, where particles with large deviatoric strain rate reside. The width of these shear lines is about twice

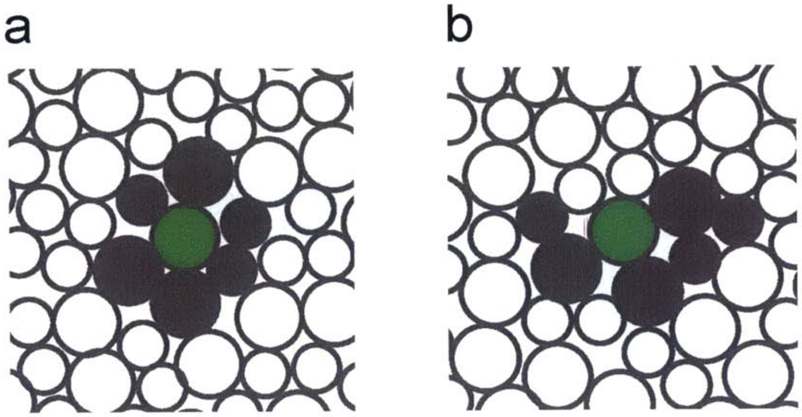

Figure 5-7: (a) Illustration of a particle (colored in green) and its neighbors (colored in black) within a cut-off distance $R_c = 1.25D$ at an initial reference configuration. (b) The same set of particles at a later stage of deformation. We seek to find the best-affine transformation matrix $\mathbf{J}$ that maps the coordinates of the particles illustrated in (a) to those in (b). This optimization procedure also gives the non-affine displacement $D^2_{\text{min}}$ associated with the central (green) particle, and the deviatoric strain $\eta^s$ in the neighborhood, as discussed in the main text.

the diameter of the particles. These shear lines largely correspond to the moving boundary between the deformed and undeformed regions in the pillar. The presence of such shear lines will appear clearer as pillar size increases, which will be discussed in the later part of the article.

Comparing the $D^2_{\text{min}}$ profile in Fig. 5-5c with deviatoric strain rate $J_2$ in Fig. 5-5b, it is clear that particles with larger values of $D^2_{\text{min}}$ are correlated with larger values of $J_2$, and hence also deviatoric strain $\eta^s$ (Eq. 5.18). The deviatoric strain $\eta^s$ reflects the local shear component of affine deformation (shape change), while $D^2_{\text{min}}$ measures additional particle displacement with respect to its neighbors that cannot be described by mere shape change. The positive correlation between $D^2_{\text{min}}$ and $\eta^s$ is understandable because the larger the value of $\eta^s$ (which usually drives plastic deformation), the error of describing local particle rearrangement in terms of purely shape change, which is the definition of $D^2_{\text{min}}$, will more likely to be larger.

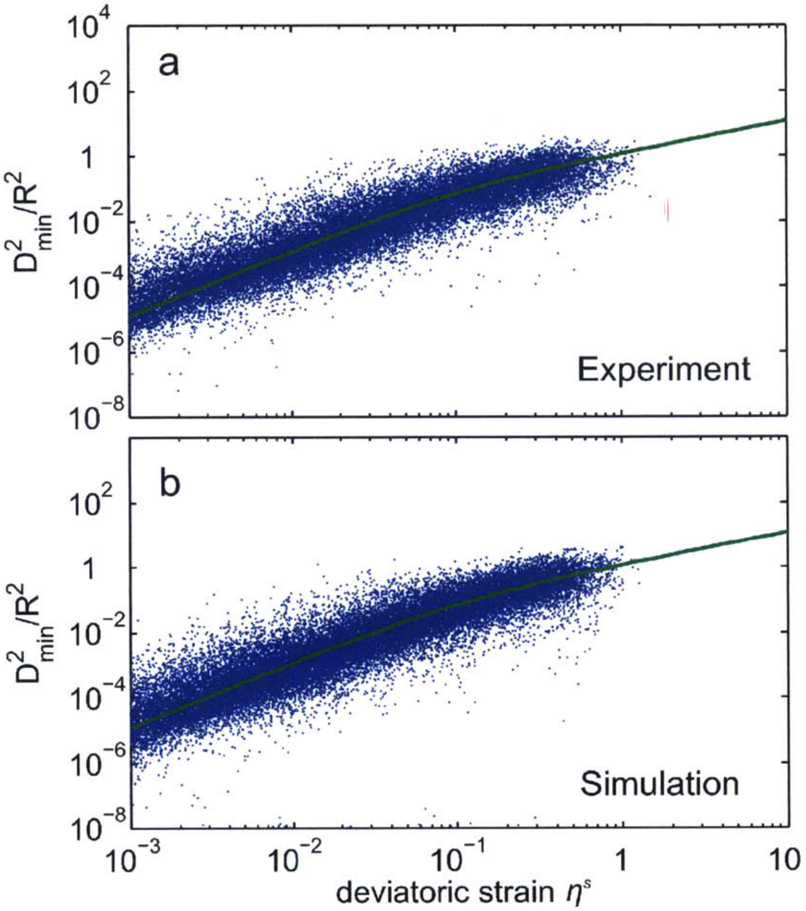

Figure 5-8: Fitting of $D^2_{\text{min}}/R^2$ with respect to deviatoric strain $\eta^s$ for both (a) experiment and (b) simulation. The data are fitted to an exponential crossover equation from quadratic to linear scaling (see the main text for details). In (a), the green curve is the best-fitting curve for the experimental data. For (b), as the fitting results is nearly identical to (a), we plot the same fitting curve as in (a) to demonstrate the closeness in the fitting result.

## 5.4 Local Deviatoric Strain Driven Particle Diffusion

The positive interdependence between $D^2_{\text{min}}$ and $\eta^s$ motivates us to map out their correlation quantitatively. Starting with an initial configuration of the pillar at time $t$ that corresponds to deformation strain $\varepsilon = v_c t/H_0$, we fix the neighbor sampling distance $R_c = 1.25D$ and calculate $\eta^s(t, \Delta t)$ and $D^2_{\text{min}}(t, \Delta t)$ for each particle in the pillar using a logarithmic series of time interval $\Delta t \in [2, 4, 8, ..., 128]/15\ R/v_c$. This procedure is then repeated for at least eight values of initial times $t$ equally spaced by $\frac{2}{3}R/v_c$. We then plot all the calculated values of $D^2_{\min}(t, \Delta t)$ with respect to $\eta^s(t, \Delta t)$ on a single plot, using logarithmic axes for both $D^2_{\min}$ and $\eta^s$. The results of experiment and simulation are shown together in Fig. 5-8. From Fig. 5-8, it can be seen that while for a given specific value of $\eta^s$, the possible values of $D^2_{\min}$ are scattered, the existence of statistical correlation between $D^2_{\min}$ and $\eta^s$ is apparent. We find that in the range of small values of $\eta^s$, $D^2_{\min}$ scales quadratically with $\eta^s$, which gradually transits to linear scaling at larger values of $\eta^s$. This is reminiscent of the scaling relationship between the growth of mean squared displacement (MSD) for a thermally diffusive particle and time $t$, which is often explained pedagogically by an unbiased random walker. Indeed, we find that, by considering $D^2_{\min}$ as MSD, and deviatoric strain $\eta^s$ as time, the data in Fig. 5-8 can be fit very well using the following equation that describes the exponential crossover of a thermal particle from ballistic to diffusive motion, expected for a Langevin particle with no memory [173]:

$$D^2_{\min}(\eta^s)/R^2 = 4\Theta\eta^s - 4\Theta\eta^s_c\left[1 - \exp(-\eta^s/\eta^s_c)\right], \qquad (5.19)$$

where on the left hand side of the above equation, the calculated $D^2_{\min}$ is scaled by $R^2$ to render it dimensionless. $\Theta$ is the dimensionless effective diffusivity while $\eta^s_c$ takes meaning of "crossover deviatoric strain". Our fitting of the data gives $\Theta = 0.3$, $\eta^s_c = 0.049$ for the experiment, and $\Theta = 0.3$, $\eta^s_c = 0.05$ for the simulation.

The analogy between $D^2_{\min}$ and MSD, and between $\eta^s$ and time $t$, may have deep implications. $D^2_{\min}$ describes the mean-squared non-affine displacement of a particle with respect to its neighbors and can be naturally identified as an analogy to MSD. The analogy between deviatoric strain $\eta^s$ and time $t$ implies that, for the granular packings, where there is no thermal agitation and the system is deformed heterogeneously, the cumulative deviatoric strain plays the role of time and drives effective particle diffusion. Argon had originally used bubble raft deformation to illustrate the concept of shear transformation zone (STZ) [174, 175], which emphasizes the affine part of localized stress-driven processes. Recently, Wang *et al.* found that cyclic mechanical loading can induce the nano-crystallization of metallic glasses well below the glass transition temperature [159], resulting from stress-driven accumulation of non-affine displacement of the atoms in the sample. The concept of shear diffusion transformation zones (SDTZs) was proposed by the authors to explain the experimental results and to emphasize the diffusive character of STZs. Our results lend support to the concept of SDTZ by showing that, even in amorphous granular packings, where there is no thermal-driven diffusion at all, if the accumulated local deviatoric strain is large enough (above a few percent strain), the non-affine displacement of a particle with respect to its neighbors crosses over to the diffusive limit. This suggests that SDTZ may be a key concept for a broad range of amorphous solids.

The analogy between local cumulative shear transformation strain in athermal amorphous solids and time in thermal systems for particle diffusion may be rationalized by a "space-time equivalence" argument, as follows. A finite temperature $k_{\mathrm{B}}T$ means temporally random momentum fluctuations, for crystals and non-crystals alike. Even in crystals, such random momentum fluctuations (due to collision of multiple phonons) can drive the random walker behavior of a particle, if these temporal fluctuations can be significant compared to the potential energy barrier. But in amorphous solids without spontaneous temporal fluctuations, there will be nonetheless still another source of randomness, which is the local spatial structure and structural response of the amorphous solid. This is indeed what motivated the "heterogeneously randomized STZ model" [176, 177]. In other words, even if two "Eshelby inclusions" at different locations of an amorphous solid transform by exactly the same transformation strain $\eta$, one reasonably would still expect drastically different internal particles arrangements and rearrangements inside these zones. This ultimately is because the local strain $\eta$ is just a coarse-graining variable, that represents a key aspect of the structural transformations of a kinetically frozen random cluster, but not all of its structural information. (This may not be true in simple crystals, where $\eta$ may entirely capture the entire structure.) Such structural mutations beyond transformation strain are reflected in $D^2_{\mathrm{min}}$. The fact that $D^2_{\mathrm{min}}$ will accumulate linearly with strain at steady state means the structural mutations from generation to generation [176, 177] are largely non-repeating and essentially unpredictable, if starting from a spatially random configuration at the beginning, even when the stress condition driving these transformations remains largely the same. Our experiment and simulation on compressing amorphous granular pillars can thus be seen as a "spatial random number generator" with the initial configuration as the "random number seed", in contrast to more well-known "temporal random number generator" algorithms; but both types of algorithms tend to give long-term uncorrelated increments for the random walker.

## 5.5 Simulation of Size-Dependent Pillar Deformation

Having achieved good agreement between experiment and simulation for the $N = 1000$ pillar, we now take advantage of the fact that our simulation can treat much larger systems than experiment, to study the size-dependent deformation behavior of the granular pillars by simulation. Three large-sized pillars, denoted by $N = 4000$, $N = 16000$ and $N = 64000$, are deformed by the top bar moving at the same deformation speed $v_c$. The aspect ratio of the pillars (2 to 1) is fixed to be the same value of the $N = 1000$ pillar. As the initial packing density of the particles in the pillar is also the same, the initial width of the pillars $W_0$ scales as $\sqrt{N}$.

We find the macroscopic shape evolution of the different-sized pillars is self-similar during deformation. At the same values of deformation strain $\varepsilon = \Delta H/H_0$, we extract the boundaries of the pillars, rescale them by the respective initial pillar width $W_0$, and plot them together in Fig. 5-9. The rescaled boundaries of the pillars are nearly identical to each other. This also implies that, the width of the top edge of a pillars $W$ divided by its original width $W_0$, is to a good approximation only a function of strain $\varepsilon$ but not the pillar size, namely $W/W_0 = \chi(\varepsilon)$, where the scaling function $\chi$ does not depend on the pillar width $W_0$.

We also find that, the average flow stress of the pillars increases linearly with

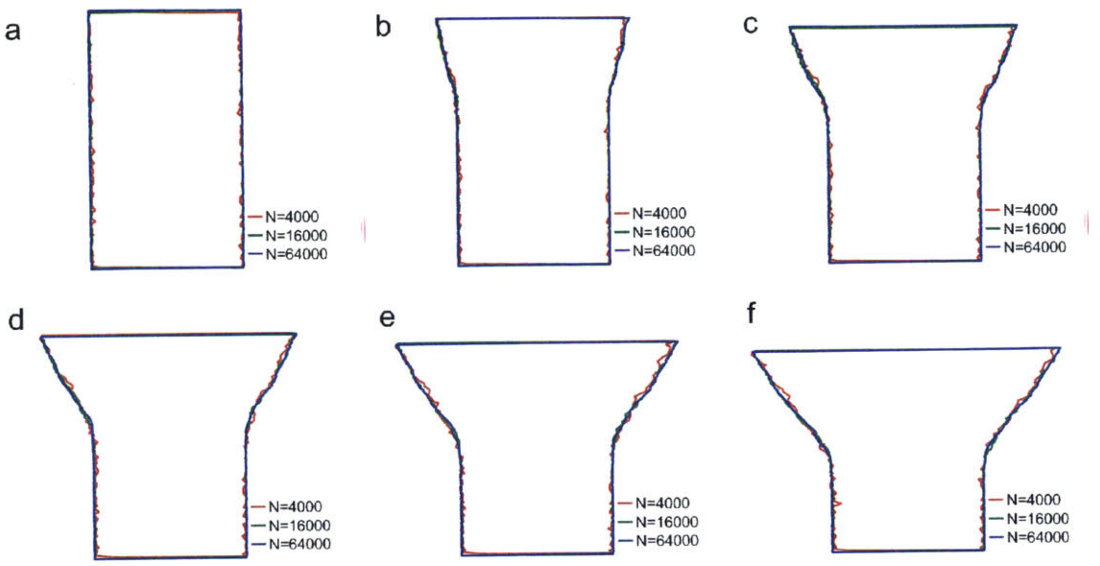

Figure 5-9: Self-similar evolution of pillar shapes during deformation of different-sized pillars. The boundaries of three pillars ($N = 4000$, $N = 16000$ and $N = 64000$) are rescaled and plotted together at the same strain value.

the initial pillar width $W_0$, as shown in Fig. 5-10(a-b). Mathematically, this can be expressed as $\langle\sigma\rangle \propto W_0$, where we define $\langle\sigma\rangle$ to be the average flow stress for strain $\varepsilon$ between 0.05 and 0.2. This scaling behavior for the flow stress indicates that, for the 2D disordered granular pillars, the behavior of "smaller is weaker" is exhibited. This is quite different from the deformation of free-standing metallic glass pillars, where "smaller is stronger" is the general trend [178, 179].

To understand the surprising size dependence of flow stress, we first look at the stress distribution in the pillars. In Fig. 5-5 we have shown that the grains in the interior region of the pillar experience larger inter-particle contact forces, resulting in larger local stress in the interior region of the pillar. The rate of increase for local stress as a function of distance to the lateral edges of the pillars is found to be very close for different-sized pillars. Such stress non-uniformity should also be reflected in the local contact pressure between the moving bar and the pillar. Indeed, we find that the contact pressure is also spatially rather non-uniform. Fig. 5-10c shows that, the local contact pressure increases almost linearly from near zero at the edge of pillar to saturated values around the center of contact interface. The maximum values of local

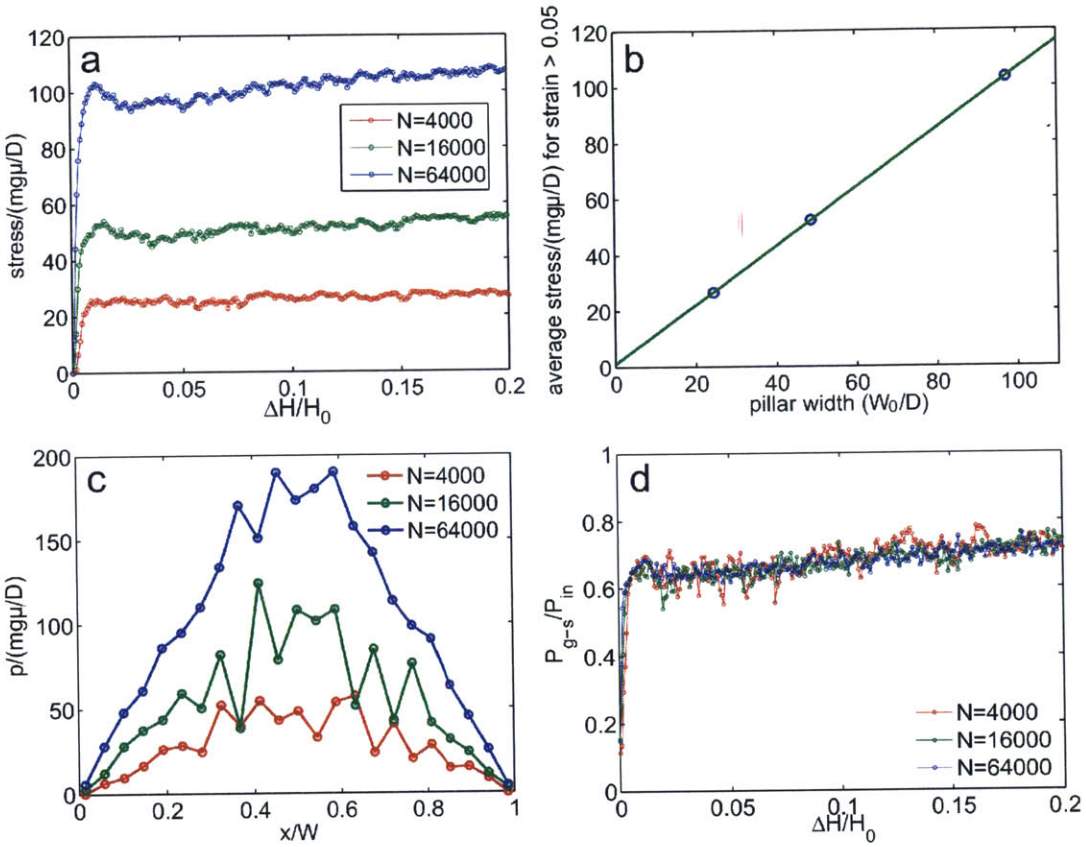

Figure 5-10: Size-dependent flow stress and dissipation of input power. (a) Stress strain curves for different sized pillars. (b) Linear scaling of average flow stress with respect to pillar width $W_0$. The average flow stress is computed for the range of strain between 0.05 and 0.2. (c) Local contact pressure $p$ between the moving bar and the pillars as a function of position $x$ along the contact interface, computed for different sized pillars at a representative value of deformation strain in the plastic flow regime. The position $x$ is scaled by the width of the pillar $W$ at the contact interface. (d) Fraction of input power dissipated by the grain-substrate friction as a function of deformation strain for different-sized pillars.

contact pressure scale roughly linearly with pillar width, consistent with the linear scaling of pillar flow stress.

Since the pillars are deformed quasistatically, most of the deformation work on the pillars will be dissipated during plastic flow. The flow stress is therefore closely related to the dissipation of energy in the systems. We hence study how the energy dissipation in the pillars changes with pillar size. As the granular particles in the pillars stand on a substrate, two major mechanisms of energy dissipation during plastic flow can be identified: one is due to the grain-substrate friction and the other can be attributed to the grain-grain friction. The total external power input by the moving bar into the pillar, denoted by $P_{\text{in}}$, can be calculated as

$$P_{\text{in}} = F_{\text{bar}} v_c = \sigma W v_c. \tag{5.20}$$

We have shown that, compared at the same deformation strain $\varepsilon$, both the flow stress $\sigma$ and pillar width $W$ are proportional to the initial pillar width $W_0$. Hence, the input power by the external force scales quadratically with $W_0$, namely $P_{\text{in}} \propto W_0^2$. As most of the input power will be dissipated in the plastic flow regime, the dissipated power should also scale with $W_0^2$. To study how the dissipated power is distributed between the substrate-induced friction and grain-grain friction, we compute the fraction of input power dissipated by the grain-substrate frictional force and study its size dependence. The amount of power dissipated by the grain-substrate friction force, denoted by $P_{\text{g-s}}$, can be calculated as

$$P_{\text{g-s}} = \sum_i m_i g \mu v_i, \tag{5.21}$$

where the particle mean velocity $v_i$ has the same definition as in Eq. 5.13, namely the average displacement of the particle $i$ within a small time interval $\Delta t$. The fraction of power dissipated by the substrate-induced friction, denoted by $\kappa$, is then given by $\kappa \equiv P_{\text{g-s}}/P_{\text{in}}$. We calculate the values of $\kappa$ for different sized pillars and plot them as a function of deformation strain in Fig. 5-10d. The result indicates that $\kappa$ is statistically independent of pillar size. This allows us to conclude that the amount of input power dissipated by grain-substrate friction, $P_{\text{g-s}} = \kappa P_{\text{in}}$, also scales quadratically with pillar size $W_0$, and hence scales linearly with the number of particles in the pillar $N$. This effectively means that the number of particles participating in the plastic flow scales linearly with the total number of particles in the pillar, which is consistent with the self-similar shape evolution of the pillars.

The calculated values of $\kappa$ in Fig. 5-10d indicate that the majority of deformation work is dissipated by the friction between the particles in the pillar and the substrate. Substrate friction therefore must play an important role in the linear increase of flow stress with respect to pillar width and the self-similar evolution of pillar shape, which have been shown to be consistent with each other. The granular pillars in our study are not truly two-dimensional due to the presence of grain-substrate friction. This setup is however necessary for stable plastic flow of the uniaxially deformed granular pillars without cohesive interparticle interaction. Without the grain-substrate friction, the deformation behavior of the granular pillars are expected to be quite different, and the size-dependent deformation behavior observed in this study (*i.e.* "smaller is weaker") may no longer hold.

If the macroscopic shape evolution of the pillars in our systems is self-similar, then how does the local yielding behavior vary with pillar size? We characterize the deformation-induced local structural change of the pillar by computing the deviatoric strain rate $J_2$ associated with each particle between two stages of deformation, using the same methodology described earlier in the article. We find that, within a small amount of pillar strain, particles with large values of $J_2$ organize into thin shear lines, which becomes more evident as pillar size increases, as shown in Fig. 5-11. These shear lines orient along the direction about 45 degree to the direction of uniaxial compression. Clearly, such shear lines form along the direction of maximum shear stress. The sharpest shear lines appear predominantly at the moving boundary between the deformed and undeformed region in the pillars, as we have mentioned earlier when discussing the combined experimental and simulation study of small-sized pillars. A close-up view of these shear lines in Fig. 5-11 indicates that the width of the shear lines does not change as pillar size increases, maintaining a value about twice the diameter of a grain. We emphasize that these shear lines are transient in time. As deformation goes on, new shear lines will form elsewhere in the pillar, while the particles in the shear lines formed earlier may not accumulate significant amount of shear strain continuously. Evidence of such transient shear bands in granular materials was previously reported in the discrete element simulations by Aharonov and Sparts [180] and Kuhn [181, 182]. Maloney and Lemaître [183], and Tanguy *et al.* [184]

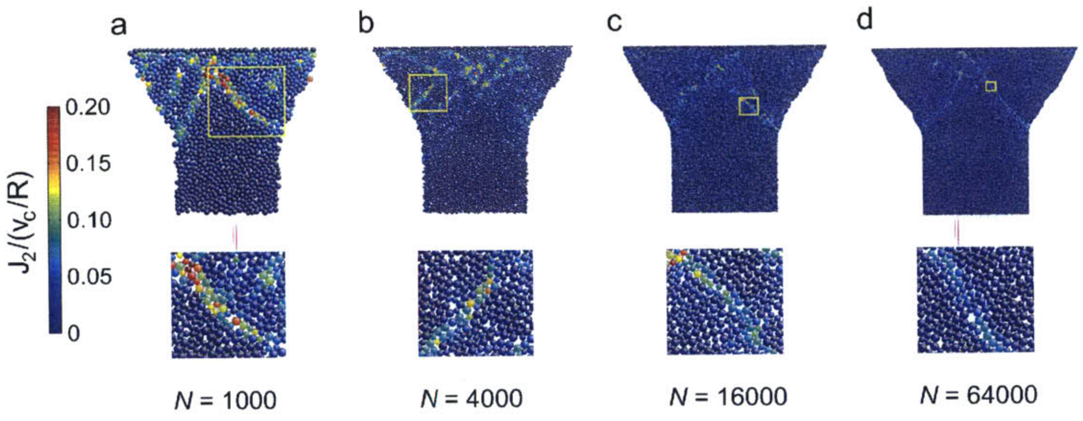

Figure 5-11: Deviatoric strain rate $J_2$ associated with each particle and zoom-in views of the transient shear lines in different-sized pillars. Four different-sized pillars are compared with each other, which contain 1000, 4000, 16000, 64000 grains respectively (from left to right). The regions in the pillars for zoom-in views are indicated by squares. For each pillar, the two configurations of pillars used for $J_2$ calculation are separated by time difference $\Delta t = 8/15\ R/v_c$.

observed transient lines of slip in their athermal, quasistatic simulation of 2D glasses of frictionless particles, and explained their formation in terms of elastic coupling and cascading of shear transformation zones. The results of our combined experiment (Fig. 5-5) and simulation of uniaxial, quasistatic deformation of 2D granular pillars clearly demonstrate the existence of such transient shear lines, which carry localized deformation in the granular pillars.

The size-independent width of the transient shear lines is surprising since the overall macroscopic shape of the pillar is self-similar in systems of different sizes. Despite the self-similarity at the macroscopic scale, the system is not self-similar in how it yields at the microscopic scale. Since the slip lines are independent of system size, there must be more of them in larger systems, which is indeed observed in our simulation. Why the system chooses to be self-similar at the macroscopic scale but not at the microscopic scale is an interesting point for future study.

## 5.6 Concluding Remarks

We have carried out combined experiments and simulations of the quasistatic, uniaxial deformation of 2D amorphous granular pillars on a substrate. The simulation model developed in this article achieves excellent quantitative match to the experiment. In particular, we find that, for the granular packings, the non-affine displacements of the particles exhibit exponential crossover from ballistic motion to diffusion-like growth behavior with respect to local deviatoric strains. This result is a generalization to inhomogeneous loading of earlier observations of stress-driven diffusion of particles in simulated 2D molecular glasses under simple shear or pure shear in the thermal, quasistatic limit [158, 184, 185, 186, 187, 188]. Because in our study the "time" variable for diffusion, the best-fit deviatoric strain in a neighborhood, is a local measure of deformation and shear transformation, we expect that the non-affine displacement should cross over from ballistic to diffusive behavior in amorphous solids under any loading conditions.

In metallic glass pillars, the apparent strength of the pillar and strain localization behavior depends on pillar diameter, manifesting so-called "size-dependent plasticity" behavior [177]. Often, "smaller is stronger" holds for metallic glasses [178, 179]. We have shown that for 2D granular pillars on a substrate, the frictional interaction between the granular particles and the substrate leads to the opposite size-dependent response, namely "smaller is weaker".

Finally, our combined experiment and simulation study clearly demonstrate that transient lines of slip form in quasistatically deformed amorphous granular pillars under uniaxial loading condition. These system-spanning shear lines carry localized shear transformations in 2D granular pillars, and their width shows no size dependence. Altogether, these results could have important implications for the plasticity and internal structural evolution of amorphous solids.

# Chapter 6

# Summary and Future Work

In this thesis, we have studied the engineering of the structure and properties of materials by high deviatoric strain or stress. The applied strain can be both elastic and inelastic, therefore two different approaches, elastic strain engineering (ESE) and inelastic strain engineering (ISE) can be distinguished. The focus of ESE is on tuning the functional properties of materials by elastic strain, while the focus of ISE is on controlling the microstructure of materials by generating inelastic strain via plastic deformation or strain-induced structural phase transformations.

For ESE, we have theoretically studied in Chapter 3 the electronic structure change of semiconductor crystals under slowly-varying inhomogeneous strain, and showed that bound states of electrons and holes can form in inhomogeneously strained semiconductors due to strain-dependent shift of valence and conduction band energy levels. We developed a new envelope function formalism with strain-parametrized expansion basis functions that has the potential to efficiently solve the electronic structure of slowly-varying inhomogeneously strained semiconductor crystals, which was demonstrated numerically using a one-dimensional model. Our results indicate that, if the locality principle of electronic structure [96, 97, 98] holds well in strain-deformed semiconductor crystals, then the envelope function formalism developed in Chapter 3 is an powerful approach that can be used to connect the local and global electronic structure of inhomogeneously strained crystals. This method provides hope that the phase-coherent electronic structure of inhomogeneously strained crystals, which at present is very difficult to study using *ab initio* approaches due to the large number of atoms typically involved in an inhomogeneously deformed system, can be solved in a "divide and conquer" manner. Namely, the problems is broken down into the solution of the electronic structure of homogeneously strained crystals by unit-cell level first-principles electronic structure calculations, and the solution of a set of coupled differential equations for the envelope functions. The second step, the solution of envelope function equations, will incorporate the relevant local electronic structure information obtained from the first step, and is a computationally easier problem due to the slowly-varying nature of the envelope functions.

While the work presented in Chapter 3 lays down the foundation of employing envelope function formalism with a strained-parametrized basis set to solve the electronic structure of slowly-varying inhomogeneously strained crystals, we acknowledge that, at present, the demonstration of the method remains at the level of a one-dimensional, simplified theoretical model. Therefore, an important part of future work is to apply the method to real material systems. This could be a challenging task due to the enlarged strain space and the more complicated electronic wavefunctions in higher dimensions. In Chapter 3, we have provided a flow chart to illustrate the implementation of our method in generic higher-dimension problems. Future work will demonstrate that the framework can be executed efficiently for realistic inhomogeneously-strained crystals. Benchmark of the method against current state-of-the-art electronic structure methods also needs to be carried out, to convincingly demonstrate the advantage or the unique capability of our method over other existing methods.

We emphasize that, ESE is a rich and vastly unexplored field [12], and many fundamental research problems remain. While there has been systematic theoretical work on the effects of elastic strain on the electronic properties of semiconductors [89], for many other properties, in particular the non-linear response properties of materials, the effects of strain have only been scarcely or phenomenologically explored. In particular, we note that higher order response of materials to external field could be more sensitive to applied strain than linear properties. This will be an important future research direction in ESE. Another important issue for ESE is that, while computing the strain-dependent properties of materials is relatively straightforward once an appropriate calculation tool is available, identifying the fundamental physics responsible for the strain-induced property change and expressing it as a low-dimensional descriptor ("material genome") [189] is considerably harder. This will be another important future direction for research in ESE.

Chapter 4 and Chapter 5 of the thesis focus on ISE, with an emphasis on the effect of inelastic deviatoric structure on the structure and dynamics of soft materials. Due to the relatively weak interaction between the constituent units, the microstructure of soft matter is in general more susceptible to mechanical loads than their hard materials counterparts. In Chapter 4 of this thesis, we have studied the mechanical response and deviatoric stress-driven sintering of self-assembled superlattices (supercrystals) of alkanethiol-passivated metallic nanocrystals. The alkanethiol molecules, which chemically adsorb on the surface of the nanocrystals, protect the metallic cores of the nanoparticles from sintering with each other. Our large-scale molecular dynamics simulations demonstrate, however, that the alkanethiol ligands can be purposely displaced if chemical potential gradient is set up in nanoparticle superlattices by external deviatoric stress, leading to controlled and ordered sintering of the nanocrystals. This process is fast and can occur at room temperature. Specifically, we found that, if the hydrostatic component of the external stress is above several hundred MPa, then applying a critical deviatoric stress along the nearest-neighbor direction of the superlattice the can convert gold nanoparticle superlattices into ordered thiol-passivated gold nanowire arrays. A moderate hydrostatic stress component is found to be necessary to elevate the yield stress of the nanoparticle superlattice to be higher than the critical deviatoric stress required for nanoparticle fusion. We have applied these insights to binary nanoparticle superlattices and demonstrate that for gold-silver (Au-Ag) binary nanoparticle superlattices, a hydrostatic stress component of order several hundred MPa combined with a critical deviatoric stress of the same order along the nearest-neighbor direction of the superlattice can induce the sintering of nanocrystals in the superlattices into ordered gold-silver multi-junction nanowire arrays. These results are important for possible future industrial-scale production of nanowire arrays and multi-junction nanowire arrays from nanoparticle superlattices.

In Chapter 5, we use two-dimensional amorphous granular pillars as model systems to study the uniaxial and quasi-static deformation induced plastic flow and internal structure evolution in disordered solids. Because the particles in the granular pillars are of macroscopic size, thermal motion is negligible for the granular particles and the system is effectively at zero vibrational temperature. The cylindrical granular particles stand upright on a substrate, which dissipates the kinetic energies in the granular pillars through frictional interaction between the particles and substrate. Our study thus probes the strain-response of a model disordered solid in the athermal (zero temperature) limit. We developed a simulation model that achieves excellent quantitative match with the parallel experimental study by our experimental collaborators. The combined experimental and simulation work demonstrates that, for the amorphous granular pillars under inhomogeneous load, the cumulative local deviatoric strains of the particles play the role of time in thermal systems, and drive the ballistic to diffusive motion crossover of the particle non-affine displacements with respect to their neighbors. Our result is consistent with a previous experimental study which showed that cyclic loading can induce the crystallization of a metallic glass at room temperature [159], which is well below the glass transition temperature of the metallic glass. At such temperature, thermal motion induced diffusion is extremely slow. However, diffusion is typically required for the crystallization of glasses. Hence, a concept of shear diffusion transformation zone (SDTZ) was proposed [159], which claims that in metallic glasses, cyclic loading induces local shear transformations that are accompanied with certain amount of particle diffusion. The temperature at which the study was carried out, while well-below the glass transition temperature the metallic glasses, was still non-zero. In contrast, in our combined experiment and simulation on the deformation of granular pillars, the system is strictly at the zero vibrational temperature. Therefore, our study provides a rigorous test of the concept of SDTZ, and convincingly demonstrates that, in disordered solids, deviatoric strain alone can induce the diffusive motion of particles without thermal motion. The results could have important implications for the deformation induced internal structure evolution of disordered solids.

For hard materials, such as metals and inorganic semiconductors, future work on ISE will focus on the strain induced phase transformation in nano-sized crystals, such as nanoparticles, nanowires and atomic layers. For soft materials, we envision that future work on ISE could occur in the direction of deviatoric strain induced phase transformation of complex-liquid mesophases that can sustain static shear stress, and in general the non-equilibrium behavior of soft matter under driven conditions.

# Bibliography

[1] J. Frenkel, "The theory of the elastic limit and the solidity of crystal bodies," *Z. Phys.*, vol. 37, pp. 572–609, 1926.

[2] E. Orowan, "Problems of plastic gliding," *Proc. Phys. Soc.*, vol. 52, no. 1, pp. 8–22, 1940.

[3] A. H. Cottrell, "Strong solids," *Proc. R. Soc. Lond. A.*, vol. 282, no. 1388, pp. 2–9, 1964.

[4] W. R. Tyson, "Theoretical strength of perfect crystals," *Philos. Mag.*, vol. 14, no. 131, pp. 925–936, 1966.

[5] F. Milstein, "Theoretical strength of a perfect crystal," *Phys. Rev. B*, vol. 3, pp. 1130–1141, 1971.

[6] N. H. Macmillan and A. Kelly, "The mechanical properties of perfect crystals. I. the ideal strength," *Proc. R. Soc. Lond. A.*, vol. 330, no. 1582, pp. 291–308, 1972.

[7] A. T. Paxton, P. Gumbsch, and M. Methfessel, "A quantum mechanical calculation of the theoretical strength of metals," *Philos. Mag. Lett.*, vol. 63, no. 5, pp. 267–274, 1991.

[8] J. Wang, J. Li, S. Yip, S. Phillpot, and D. Wolf, "Mechanical instabilities of homogeneous crystals," *Phys. Rev. B*, vol. 52, pp. 12627–12635, 1995.

[9] S. Ogata, J. Li, N. Hirosaki, Y. Shibutani, and S. Yip, "Ideal shear strain of metals and ceramics," *Phys. Rev. B*, vol. 70, p. 104104, 2004.

[10] J. Pokluda, M. Čern𝑦̌, P. Šandera, and M. Šob, "Calculations of theoretical strength: State of the art and history," *J. Comput. Aided Mater. Des.*, vol. 11, no. 1, pp. 1–28, 2004.

[11] T. Zhu and J. Li, "Ultra-strength materials," *Prog. Mater. Sci.*, vol. 55, pp. 710–757, 2010.

[12] J. Li, Z. Shan, and E. Ma, "Elastic strain engineering for unprecedented materials properties," *MRS Bull.*, vol. 39, no. 02, pp. 108–114, 2014.

[13] C. Lee, X. D. Wei, J. W. Kysar, and J. Hone, "Measurement of the elastic properties and intrinsic strength of monolayer graphene," *Science*, vol. 321, no. 5887, pp. 385–388, 2008.

[14] S. Bertolazzi, J. Brivio, and A. Kis, "Stretching and breaking of ultrathin $MoS_2$," *ACS Nano*, vol. 5, no. 12, pp. 9703–9709, 2011.

[15] R. S. Jacobsen, K. N. Andersen, P. I. Borel, J. Fage-Pedersen, L. H. Frandsen, O. Hansen, M. Kristensen, A. V. Lavrinenko, G. Moulin, H. Ou, *et al.*, "Strained silicon as a new electro-optic material," *Nature*, vol. 441, no. 7090, pp. 199–202, 2006.

[16] N. Healy, S. Mailis, N. M. Bulgakova, P. J. Sazio, T. D. Day, J. R. Sparks, H. Y. Cheng, J. V. Badding, and A. C. Peacock, "Extreme electronic bandgap modification in laser-crystallized silicon optical fibres," *Nature Mater.*, vol. 13, no. 12, pp. 1122–1127, 2014.

[17] J. J. Gilman, *Electronic Basis of the Strength of Materials.* Cambridge University Press, Cambridge, UK, 2003.

[18] A. Rochefort, P. Avouris, F. Lesage, and D. Salahub, "Electrical and mechanical properties of distorted carbon nanotubes," *Phys. Rev. B*, vol. 60, no. 19, p. 13824, 1999.

[19] E. Minot, Y. Yaish, V. Sazonova, J. Park, M. Brink, and P. McEuen, "Tuning carbon nanotube band gaps with strain," *Phys. Rev. Lett.*, vol. 90, no. 15, p. 156401, 2003.

[20] K. Ahn, T. Lookman, and A. Bishop, "Strain-induced metal–insulator phase coexistence in perovskite manganites," *Nature*, vol. 428, no. 6981, pp. 401–404, 2004.

[21] J. Cao, E. Ertekin, V. Srinivasan, W. Fan, S. Huang, H. Zheng, J. Yim, D. Khanal, D. Ogletree, J. Grossman, *et al.*, "Strain engineering and one-dimensional organization of metal–insulator domains in single-crystal vanadium dioxide beams," *Nature Nanotech.*, vol. 4, no. 11, pp. 732–737, 2009.

[22] C. Kisielowski, J. Krüger, S. Ruvimov, T. Suski, J. Ager III, E. Jones, Z. Liliental-Weber, M. Rubin, E. Weber, M. Bremser, *et al.*, "Strain-related phenomena in GaN thin films," *Phys. Rev. B*, vol. 54, no. 24, p. 17745, 1996.

[23] O. Stier, M. Grundmann, and D. Bimberg, "Electronic and optical properties of strained quantum dots modeled by 8-band $\mathbf{k} \cdot \mathbf{p}$ theory," *Phys. Rev. B*, vol. 59, no. 8, p. 5688, 1999.

[24] V. Pereira and A. Castro Neto, "Strain engineering of graphenes electronic structure," *Phys. Rev. Lett.*, vol. 103, no. 4, p. 46801, 2009.

[25] M. Fischetti, F. Gamiz, and W. Hansch, "On the enhanced electron mobility in strained-silicon inversion layers," *J. Appl. Phys.*, vol. 92, no. 12, pp. 7320–7324, 2002.

[26] T. Jungwirth, M. Abolfath, J. Sinova, J. Kucera, and A. MacDonald, "Boltzmann theory of engineered anisotropic magnetoresistance in (Ga, Mn) As," *Appl. Phys. Lett.*, vol. 81, no. 21, pp. 4029–4031, 2002.

[27] Y. Kato, R. Myers, A. Gossard, and D. Awschalom, "Coherent spin manipulation without magnetic fields in strained semiconductors," *Nature*, vol. 427, no. 6969, pp. 50–53, 2004.

[28] M. Csontos, G. Mihaly, B. Janko, T. Wojtowicz, X. Liu, and J. Furdyna, "Pressure-induced ferromagnetism in (In, Mn)Sb dilute magnetic semiconductor," *Nature Mater.*, vol. 4, no. 6, pp. 447–449, 2005.

[29] D. Mosca, F. Vidal, and V. Etgens, "Strain engineering of the magnetocaloric effect in MnAs epilayers," *Phys. Rev. Lett.*, vol. 101, no. 12, p. 125503, 2008.

[30] M. Aumer, S. LeBoeuf, S. Bedair, M. Smith, J. Lin, and H. Jiang, "Effects of tensile and compressive strain on the luminescence properties of AlInGaN/InGaN quantum well structures," *Appl. Phys. Lett.*, vol. 77, no. 6, pp. 821–823, 2000.

[31] E. Le Ru, P. Howe, T. Jones, and R. Murray, "Strain-engineered InAs/GaAs quantum dots for long-wavelength emission," *Phys. Rev. B*, vol. 67, no. 16, p. 165303, 2003.

[32] T. Koga, X. Sun, S. Cronin, and M. Dresselhaus, "Carrier pocket engineering applied to strained Si/Ge superlattices to design useful thermoelectric materials," *Appl. Phys. Lett.*, vol. 75, no. 16, pp. 2438–2440, 1999.

[33] M. Mavrikakis, B. Hammer, and J. Nørskov, "Effect of strain on the reactivity of metal surfaces," *Phys. Rev. Lett.*, vol. 81, no. 13, pp. 2819–2822, 1998.

[34] K. Yang, W. Setyawan, S. Wang, M. B. Nardelli, and S. Curtarolo, "A search model for topological insulators with high-throughput robustness descriptors," *Nature Mater.*, vol. 11, no. 7, pp. 614–619, 2012.

[35] P. G. de Gennes, "Soft matter," *Rev. Mod. Phys.*, vol. 64, pp. 645–648, 1992.

[36] T. A. Witten, "Insights from soft condensed matter," *Rev. Mod. Phys.*, vol. 71, pp. S367–S373, 1999.

[37] W. Li, X. Qian, and J. Li, "Envelope function method for electrons in slowly-varying inhomogeneously deformed crystals," *J. Phys. Condens. Matter*, vol. 26, no. 45, p. 455801, 2014.

[38] W. Li, H. Fan, and J. Li, "Deviatoric stress-driven fusion of nanoparticle superlattices," *Nano Lett.*, vol. 14, no. 9, pp. 4951–4958, 2014.

[39] L. D. Landau and E. M. Lifshitz, *Theory of Elasticity.* Pergamon Press, Oxford, New York, 1970.

[40] S. C. Hunter, *Mechanics of Continuous Media.* Halsted Press, New York, 2 ed., 1983.

[41] D. C. Wallace, *Thermodynamics of Crystals.* Wiley, New York, 1972.

[42] M. L. Falk and J. S. Langer, "Dynamics of viscoplastic deformation in amorphous solids," *Phys. Rev. E*, vol. 57, pp. 7192–7205, 1998.

[43] F. Shimizu, S. Ogata, and J. Li, "Theory of shear banding in metallic glasses and molecular dynamics calculations," *Mater. Trans.*, vol. 48, no. 11, pp. 2923–2927, 2007.

[44] J. Li, *Modeling Microstructural Effects of Deformation Resistance and Thermal Conductivity.* PhD thesis, Massachusetts Institute of Technology, 2000.

[45] D. Frenkel and B. Smit, *Understanding Molecular Simulation from Algorithms to Applications.* Academic Press: San Diego, 2002.

[46] N. C. Admal and E. B. Tadmor, "A unified interpretation of stress in molecular systems," *J. Elasticity*, vol. 100, no. 1-2, pp. 63–143, 2010.

[47] A. F. Voter, "Hyperdynamics: Accelerated molecular dynamics of infrequent events," *Phys. Rev. Lett.*, vol. 78, pp. 3908–3911, 1997.

[48] A. F. Voter, F. Montalenti, and T. C. Germann, "Extending the time scale in atomistic simulation of materials," *Annu. Rev. Mater. Res.*, vol. 32, no. 1, pp. 321–346, 2002.

[49] A. Laio and M. Parrinello, "Escaping free-energy minima," *Proc. Natl. Acad. Sci. U.S.A.*, vol. 99, no. 20, pp. 12562–12566, 2002.

[50] R. A. Miron and K. A. Fichthorn, "Accelerated molecular dynamics with the bond-boost method," *J. Chem. Phys.*, vol. 119, no. 12, pp. 6210–6216, 2003.

[51] S. Hara and J. Li, "Adaptive strain-boost hyperdynamics simulations of stress-driven atomic processes," *Phys. Rev. B*, vol. 82, p. 184114, 2010.

[52] A. Ishii, S. Ogata, H. Kimizuka, and J. Li, "Adaptive-boost molecular dynamics simulation of carbon diffusion in iron," *Phys. Rev. B*, vol. 85, p. 064303, 2012.

[53] J. Li, "Basic molecular dynamics," in *Handbook of Materials Modeling*, pp. 565–588, Springer, 2005.

[54] M. E. Tuckerman and G. J. Martyna, "Understanding modern molecular dynamics: Techniques and applications," *J. Phys. Chem. B*, vol. 104, no. 2, pp. 159–178, 2000.

[55] H. Goldstein, J. Safko, and C. Poole, *Classical Mechanics.* Addison-Wesley, 3rd ed., 2002.

[56] S. Nosé, "A molecular dynamics method for simulations in the canonical ensemble," *Mol. Phys.*, vol. 52, no. 2, pp. 255–268, 1984.

[57] W. G. Hoover, "Canonical dynamics: Equilibrium phase-space distributions," *Phys. Rev. A*, vol. 31, no. 3, p. 1695, 1985.

[58] S. Nosé, "A unified formulation of the constant temperature molecular dynamics methods," *J. Chem. Phys.*, vol. 81, no. 1, pp. 511–519, 1984.

[59] H. C. Andersen, "Molecular dynamics simulations at constant pressure and/or temperature," *J. Chem. Phys.*, vol. 72, no. 4, pp. 2384–2393, 1980.

[60] M. Parrinello and A. Rahman, "Crystal structure and pair potentials: A molecular-dynamics study," *Phys. Rev. Lett.*, vol. 45, no. 14, pp. 1196–1199, 1980.

[61] M. Parrinello and A. Rahman, "Polymorphic transitions in single crystals: A new molecular dynamics method," *J. Appl. Phys.*, vol. 52, no. 12, pp. 7182–7190, 1981.

[62] J. R. Ray and A. Rahman, "Statistical ensembles and molecular dynamics studies of anisotropic solids," *J. Chem. Phys.*, vol. 80, no. 9, pp. 4423–4428, 1984.

[63] G. J. Martyna, D. J. Tobias, and M. L. Klein, "Constant pressure molecular dynamics algorithms," *J. Chem. Phys.*, vol. 101, no. 5, pp. 4177–4189, 1994.

[64] W. Shinoda, M. Shiga, and M. Mikami, "Rapid estimation of elastic constants by molecular dynamics simulation under constant stress," *Phys. Rev. B*, vol. 69, no. 13, p. 134103, 2004.

[65] R. M. Wentzcovitch, "Invariant molecular-dynamics approach to structural phase transitions," *Phys. Rev. B*, vol. 44, pp. 2358–2361, 1991.

[66] S. Melchionna, G. Ciccotti, and B. Lee Holian, "Hoover NPT dynamics for systems varying in shape and size," *Mol. Phys.*, vol. 78, no. 3, pp. 533–544, 1993.

[67] D. J. Tobias, G. J. Martyna, and M. L. Klein, "Molecular dynamics simulations of a protein in the canonical ensemble," *J. Chem. Phys.*, vol. 97, no. 49, pp. 12959–12966, 1993.

[68] G. J. Martyna, M. L. Klein, and M. Tuckerman, "Nosé–Hoover chains: the canonical ensemble via continuous dynamics," *J. Chem. Phys.*, vol. 97, no. 4, pp. 2635–2643, 1992.

[69] K. S. Novoselov, D. Jiang, F. Schedin, T. J. Booth, V. V. Khotkevich, S. V. Morozov, and A. K. Geim, "Two-dimensional atomic crystals," *Proc. Natl. Acad. Sci. U. S. A.*, vol. 102, no. 30, pp. 10451–10453, 2005.

[70] F. Liu, P. M. Ming, and J. Li, "Ab initio calculation of ideal strength and phonon instability of graphene under tension," *Phys. Rev. B*, vol. 76, no. 6, p. 064120, 2007.

[71] J. Feng, X. F. Qian, C. W. Huang, and J. Li, "Strain-engineered artificial atom as a broad-spectrum solar energy funnel," *Nature Photon.*, vol. 6, no. 12, pp. 866–872, 2012.

[72] J. C. Slater and G. F. Koster, "Simplified lcao method for the periodic potential problem," *Phys. Rev.*, vol. 94, pp. 1498–1524, 1954.

[73] A. Di Carlo, "Microscopic theory of nanostructured semiconductor devices: beyond the envelope-function approximation," *Semicond. Sci. Technol.*, vol. 18, no. 1, pp. R1–R31, 2003.

[74] A. Zunger, "Electronic-structure theory of semiconductor quantum dots," *MRS Bull.*, vol. 23, pp. 35–42, 1998.

[75] A. Canning, L. W. Wang, A. Williamson, and A. Zunger, "Parallel empirical pseudopotential electronic structure calculations for million atom systems," *J. Comput. Phys.*, vol. 160, no. 1, pp. 29–41, 2000.

[76] L. W. Wang and A. Zunger, "Linear combination of bulk bands method for large-scale electronic structure calculations on strained nanostructures," *Phys. Rev. B*, vol. 59, no. 24, pp. 15806–15818, 1999.

[77] J. M. Luttinger and W. Kohn, "Motion of electrons and holes in pertubed periodic fields," *Phys. Rev.*, vol. 97, pp. 869–883, 1955.

[78] G. Bastard, "Superlattice band structure in the envelope-function approximation," *Phys. Rev. B*, vol. 24, no. 10, pp. 5693–5697, 1981.

[79] G. A. Baraff and D. Gershoni, "Eigenfunction-expansion method for solving the quantum-wire problem: Formulation," *Phys. Rev. B*, vol. 43, no. 5, pp. 4011–4022, 1991.

[80] D. Gershoni, C. H. Henry, and G. A. Baraff, "Calculating the optical properties of multidimensional heterostructures: Application to the modeling of quaternary quantum well lasers," *IEEE J. Quantum Electron.*, vol. 29, no. 9, pp. 2433–2450, 1993.

[81] M. G. Burt, "The justification for applying the effective-mass approximation to microstructures," *J. Phys.: Condens. Matter*, vol. 4, pp. 6651–6690, 1992.

[82] M. G. Burt, "Fundamentals of envelope function theory for electronic states and photonic modes in nanostructures," *J. Phys.: Condens. Matter*, vol. 11, no. 9, pp. R53–R83, 1999.

[83] L. W. Wang and A. Zunger, "Pseudopotential-based multiband $\mathbf{k}\cdot\mathbf{p}$ method for $\sim 250000$-atom nanostructure systems," *Phys. Rev. B*, vol. 54, pp. 11417–11435, 1996.

[84] E. O. Kane, "Band structure of indium antimonide," *J. Phys. Chem. Solids*, vol. 1, no. 4, pp. 249–261, 1957.

[85] O. Stier and D. Bimberg, "Modeling of strained quantum wires using eight-band $\mathbf{k}\cdot\mathbf{p}$ theory," *Phys. Rev. B*, vol. 55, no. 12, pp. 7726–7732, 1997.

[86] A. L. Efros and M. Rosen, "The electronic structure of semiconductor nanocrystals," *Annu. Rev. Mat. Sci.*, vol. 30, no. 1, pp. 475–521, 2000.

[87] J. Bardeen and W. Shockley, "Deformation potentials and mobilities in non-polar crystals," *Phys. Rev.*, vol. 80, no. 1, pp. 72–80, 1950.

[88] C. Herring and E. Vogt, "Transport and deformation-potential theory for many-valley semiconductors with anisotropic scattering," *Phys. Rev.*, vol. 101, pp. 944–961, 1956.

[89] G. L. Bir and G. E. Pikus, *Symmetry and Strain-Induced Effects in Semiconductors.* Wiley, New York, 1974. p. 295.

[90] Y. Zhang, "Motion of electrons in semiconductors under inhomogeneous strain with application to laterally confined quantum wells," *Phys. Rev. B*, vol. 49, no. 20, pp. 14352–14366, 1994.

[91] J. R. Chelikowsky and M. L. Cohen, "Nonlocal pseudopotential calculations for the electronic structure of eleven diamond and zinc-blende semiconductors," *Phys. Rev. B*, vol. 14, no. 2, pp. 556–582, 1976.

[92] L. W. Wang and A. Zunger, "Local-density-derived semiempirical pseudopotentials," *Phys. Rev. B*, vol. 51, no. 24, pp. 17398–17416, 1995.

[93] D. M. Wood and A. Zunger, "Successes and failures of the $\mathbf{k}\cdot\mathbf{p}$ method: A direct assessment for GaAs/AlAs quantum structures," *Phys. Rev. B*, vol. 53, no. 12, pp. 7949–7963, 1996.

[94] H. Fu, L. W. Wang, and A. Zunger, "Applicability of the $\mathbf{k}\cdot\mathbf{p}$ method to the electronic structure of quantum dots," *Phys. Rev. B*, vol. 57, no. 16, pp. 9971–9987, 1998.

[95] G. D. Whitfield, "Theory of electron-phonon interactions," *Phys. Rev.*, vol. 121, pp. 720–734, 1961.

[96] W. E and J. F. Lu, "Electronic structure of smoothly deformed crystals: Cauchy-born rule for the nonlinear tight-binding model," *Commun. Pure Appl. Math.*, vol. 63, no. 11, pp. 1432–1468, 2010.

[97] W. E and J. F. Lu, "The electronic structure of smoothly deformed crystals: Wannier functions and the cauchy-born rule," *Arch. Ration. Mech. Anal.*, vol. 199, no. 2, pp. 407–433, 2011.

[98] W. E and J. F. Lu, "The Kohn-Sham equation for deformed crystals," *Mem. Amer. Math. Soc.*, vol. 221, no. 1040, 2013.

[99] J. L. Ericksen, "On the Cauchy-Born rule," *Math. Mech. Solids*, vol. 13, no. 3-4, pp. 199–220, 2008.

[100] N. Marzari, A. A. Mostofi, J. R. Yates, I. Souza, and D. Vanderbilt, "Maximally localized Wannier functions: Theory and applications," *Rev. Mod. Phys.*, vol. 84, pp. 1419–1475, 2012.

[101] C. G. Van de Walle and R. M. Martin, ""Absolute" deformation potentials: Formulation and *ab initio* calculations for semiconductors," *Phys. Rev. Lett.*, vol. 62, pp. 2028–2031, 1989.

[102] D. V. Talapin, J. S. Lee, M. V. Kovalenko, and E. V. Shevchenko, "Prospects of colloidal nanocrystals for electronic and optoelectronic applications," *Chem. Rev.*, vol. 110, no. 1, pp. 389–458, 2010.

[103] E. V. Shevchenko, D. V. Talapin, N. A. Kotov, S. O'Brien, and C. B. Murray, "Structural diversity in binary nanoparticle superlattices," *Nature*, vol. 439, no. 7072, pp. 55–59, 2006.

[104] D. Lee, S. Jia, S. Banerjee, J. Bevk, I. P. Herman, and J. W. Kysar, "Viscoplastic and granular behavior in films of colloidal nanocrystals," *Phys. Rev. Lett.*, vol. 98, p. 026103, 2007.

[105] K. E. Mueggenburg, X.-M. Lin, R. H. Goldsmith, and H. M. Jaeger, "Elastic membranes of close-packed nanoparticle arrays," *Nature Mater.*, vol. 6, no. 9, pp. 656–660, 2007.

[106] E. Tam, P. Podsiadlo, E. Shevchenko, D. F. Ogletree, M. P. Delplancke-Ogletree, and P. D. Ashby, "Mechanical properties of face-centered cubic supercrystals of nanocrystals," *Nano Lett.*, vol. 10, no. 7, pp. 2363–2367, 2010.

[107] P. Podsiadlo, G. Krylova, B. Lee, K. Critchley, D. J. Gosztola, D. V. Talapin, P. D. Ashby, and E. V. Shevchenko, "The role of order, nanocrystal size, and capping ligands in the collective mechanical response of three-dimensional nanocrystal solids," *J. Am. Chem. Soc.*, vol. 132, no. 26, pp. 8953–8960, 2010.

[108] C. Yan, I. Arfaoui, N. Goubet, and M.-P. Pileni, "Soft supracrystals of Au nanocrystals with tunable mechanical properties," *Adv. Funct. Mater.*, vol. 23, no. 18, pp. 2315–2321, 2013.

[109] H. Wu, F. Bai, Z. Sun, R. E. Haddad, D. M. Boye, Z. Wang, and H. Fan, "Pressure-driven assembly of spherical nanoparticles and formation of 1D-nanostructure arrays," *Angew. Chem. Int. Edit.*, vol. 49, no. 45, pp. 8431–8434, 2010.

[110] H. Wu, F. Bai, Z. Sun, R. E. Haddad, D. M. Boye, Z. Wang, J. Y. Huang, and H. Fan, "Nanostructured gold architectures formed through high pressure-driven sintering of spherical nanoparticle arrays," *J. Am. Chem. Soc.*, vol. 132, no. 37, pp. 12826–12828, 2010.

[111] Z. Wang, C. Schliehe, T. Wang, Y. Nagaoka, Y. C. Cao, W. A. Bassett, H. Wu, H. Fan, and H. Weller, "Deviatoric stress driven formation of large single-crystal PbS nanosheet from nanoparticles and in situ monitoring of oriented attachment," *J. Am. Chem. Soc.*, vol. 133, no. 37, pp. 14484–14487, 2011.

[112] U. Landman and W. D. Luedtke, "Small is different: energetic, structural, thermal, and mechanical properties of passivated nanocluster assemblies," *Faraday Discuss.*, vol. 125, pp. 1–22, 2004.

[113] P. Schapotschnikow, R. Pool, and T. J. H. Vlugt, "Molecular simulations of interacting nanocrystals," *Nano Lett.*, vol. 8, no. 9, pp. 2930–2934, 2008.

[114] R. C. Lincoln, K. M. Koliwad, and P. B. Ghate, "Morse-potential evaluation of second-and third-order elastic constants of some cubic metals," *Phys. Rev.*, vol. 157, no. 3, pp. 463–466, 1967.

[115] L. A. Girifalco and V. G. Weizer, "Application of the Morse potential function to cubic metals," *Phys. Rev.*, vol. 114, no. 3, pp. 687–690, 1959.

[116] S. M. Foiles, M. I. Baskes, and M. S. Daw, "Embedded-atom-method functions for the fcc metals Cu, Ag, Au, Ni, Pd, Pt, and their alloys," *Phys. Rev. B*, vol. 33, pp. 7983–7991, 1986.

[117] W. Paul, D. Y. Yoon, and G. D. Smith, "An optimized united atom model for simulations of polymethylene melts," *J. Chem. Phys.*, vol. 103, no. 4, pp. 1702–1709, 1995.

[118] A. P. Kaushik and P. Clancy, "Explicit all-atom modeling of realistically sized ligand-capped nanocrystals," *J. Chem. Phys.*, vol. 136, p. 114702, 2012.

[119] N. L. Allinger, Y. H. Yuh, and J. H. Lii, "Molecular mechanics. The MM3 force field for hydrocarbons. 1," *J. Am. Chem. Soc.*, vol. 111, no. 23, pp. 8551–8566, 1989.

[120] H. Häkkinen, "The gold-sulfur interface at the nanoscale," *Nature Chem.*, vol. 4, no. 6, pp. 443–455, 2012.

[121] L. Z. Zhang, W. A. Goddard, and S. Y. Jiang, "Molecular simulation study of the c(4×2) superlattice structure of alkanethiol self-assembled monolayers on Au(111)," *J. Chem. Phys.*, vol. 117, pp. 7342–7349, 2002.

[122] W. Luedtke and U. Landman, "Structure, dynamics, and thermodynamics of passivated gold nanocrystallites and their assemblies," *J. Phys. Chem.*, vol. 100, no. 32, pp. 13323–13329, 1996.

[123] W. D. Luedtke and U. Landman, "Structure and thermodynamics of self-assembled monolayers on gold nanocrystallites," *J. Phys. Chem. B*, vol. 102, no. 34, pp. 6566–6572, 1998.

[124] P. K. Ghorai and S. C. Glotzer, "Molecular dynamics simulation study of self-assembled monolayers of alkanethiol surfactants on spherical gold nanoparticles," *J. Phys. Chem. C*, vol. 111, no. 43, pp. 15857–15862, 2007.

[125] K. M. Beardmore, J. D. Kress, N. Gronbech-Jensen, and A. R. Bishop, "Determination of the headgroup-gold (111) potential surface for alkanethiol self-assembled monolayers by *ab initio* calculation," *Chem. Phys. Lett.*, vol. 286, no. 1-2, pp. 40–45, 1998.

[126] C. L. Liu, J. M. Cohen, J. B. Adams, and A. F. Voter, "EAM study of surface self-diffusion of single adatoms of fcc metals Ni, Cu, Al, Ag, Au, Pd, and Pt," *Surf. Sci.*, vol. 253, no. 1, pp. 334–344, 1991.

[127] P. E. Sheehan and L. J. Whitman, "Thiol diffusion and the role of humidity in "Dip Pen Nanolithography"," *Phys. Rev. Lett.*, vol. 88, p. 156104, 2002.

[128] H. Sellers, A. Ulman, Y. Shnidman, and J. E. Eilers, "Structure and binding of alkanethiolates on gold and silver surfaces: implications for self-assembled monolayers," *J. Am. Chem. Soc.*, vol. 115, no. 21, pp. 9389–9401, 1993.

[129] W. Zhang, B. Gao, J. Yang, Z. Wu, V. Carravetta, and Y. Luo, "Electronic structure of [121] tetramantane-6-thiol on gold and silver surfaces," *J. Chem. Phys.*, vol. 130, no. 5, p. 054705, 2009.

[130] J. Hautman and M. L. Klein, "Simulation of a monolayer of alkyl thiol chains," *J. Chem. Phys.*, vol. 91, p. 4994, 1989.

[131] W. L. Jorgensen, J. D. Madura, and C. J. Swenson, "Optimized intermolecular potential functions for liquid hydrocarbons," *J. Am. Chem. Soc.*, vol. 106, no. 22, pp. 6638–6646, 1984.

[132] W. L. Jorgensen, D. S. Maxwell, and J. Tirado-Rives, "Development and testing of the OPLS all-atom force field on conformational energetics and properties of organic liquids," *J. Am. Chem. Soc.*, vol. 118, no. 45, pp. 11225–11236, 1996.

[133] M. E. Tuckerman, J. Alejandre, R. López-Rendón, A. L. Jochim, and G. J. Martyna, "A Liouville-operator derived measure-preserving integrator for molecular dynamics simulations in the isothermal–isobaric ensemble," *J. Phys. A-Math. Gen.*, vol. 39, no. 19, pp. 5629–5651, 2006.

[134] J. R. Ray, "Elastic constants and statistical ensembles in molecular dynamics," *Comput. Phys. Rep.*, vol. 8, pp. 111–151, 1988.

[135] M. Parrinello and A. Rahman, "Strain fluctuations and elastic constants," *J. Chem. Phys.*, vol. 76, pp. 2662–2666, 1982.

[136] J. R. Ray and A. Rahman, "Statistical ensembles and molecular dynamics studies of anisotropic solids. ii," *J. Chem. Phys.*, vol. 82, pp. 4243–4247, 1985.

[137] M. P. Allen and D. J. Tildesley, *Computer Simulation of Liquids.* Oxford Unviersity Press, 1989.

[138] P. Podsiadlo, B. Lee, V. B. Prakapenka, G. V. Krylova, R. D. Schaller, A. Demortiere, and E. V. Shevchenko, "High-pressure structural stability and elasticity of supercrystals self-assembled from nanocrystals," *Nano Lett.*, vol. 11, no. 2, pp. 579–588, 2011.

[139] A. E. Saunders and B. A. Korgel, "Observation of an AB phase in bidisperse nanocrystal superlattices," *ChemPhysChem*, vol. 6, no. 1, pp. 61–65, 2005.

[140] F. X. Redl, K. S. Cho, C. B. Murray, and S. O'Brien, "Three-dimensional binary superlattices of magnetic nanocrystals and semiconductor quantum dots," *Nature*, vol. 423, no. 6943, pp. 968–971, 2003.

[141] M. J. Murray and J. V. Sanders, "Close-packed structures of spheres of two different sizes ii. the packing densities of likely arrangements," *Philos. Mag. A*, vol. 42, no. 6, pp. 721–740, 1980.

[142] C. A. Schuh and A. C. Lund, "Atomistic basis for the plastic yield criterion of metallic glass," *Nature Mater.*, vol. 2, no. 7, pp. 449–452, 2003.

[143] L. Tian, J. Li, J. Sun, E. Ma, and Z.-W. Shan, "Visualizing size-dependent deformation mechanism transition in Sn," *Sci. Rep.*, vol. 3, p. 2113, 2013.

[144] J. Sun, L. He, Y.-C. Lo, T. Xu, H. Bi, L. Sun, Z. Zhang, S. X. Mao, and J. Li, "Liquid-like pseudoelasticity of sub-10-nm crystalline silver particles," *Nature Mater.*, vol. 13, no. 11, pp. 1007–1012, 2014.

[145] J. M. D. Lane and G. S. Grest, "Spontaneous asymmetry of coated spherical nanoparticles in solution and at liquid-vapor interfaces," *Phys. Rev. Lett.*, vol. 104, p. 235501, 2010.

[146] G. Y. Liu and M. B. Salmeron, "Reversible displacement of chemisorbed n-alkanethiol molecules on Au (111) surface: an atomic force microscopy study," *Langmuir*, vol. 10, no. 2, pp. 367–370, 1994.

[147] M. Salmeron, "Generation of defects in model lubricant monolayers and their contribution to energy dissipation in friction," *Tribol. Lett.*, vol. 10, pp. 69–79, 2001.

[148] C. Jarzynski, "Nonequilibrium equality for free energy differences," *Phys. Rev. Lett.*, vol. 78, pp. 2690–2693, 1997.

[149] Y. Lu, J. Y. Huang, C. Wang, S. Sun, and J. Lou, "Cold welding of ultrathin gold nanowires," *Nature Nanotech.*, vol. 5, no. 3, pp. 218–224, 2010.

[150] I. W. Chen and P. Morel, "Implications of transformation plasticity in $ZrO_2$-containing ceramics: 1, shear and dilation effects," *J. Am. Ceram. Soc.*, vol. 69, no. 3, pp. 181–189, 1986.

[151] A. Dong, J. Chen, P. M. Vora, J. M. Kikkawa, and C. B. Murray, "Binary nanocrystal superlattice membranes self-assembled at the liquid-air interface," *Nature*, vol. 466, no. 7305, pp. 474–477, 2010.

[152] D. J. Milliron, S. M. Hughes, Y. Cui, L. Manna, J. B. Li, L. W. Wang, and A. P. Alivisatos, "Colloidal nanocrystal heterostructures with linear and branched topology," *Nature*, vol. 430, no. 6996, pp. 190–195, 2004.

[153] J. Wallentin, N. Anttu, D. Asoli, M. Huffman, I. Åberg, M. H. Magnusson, G. Siefer, P. Fuss-Kailuweit, F. Dimroth, B. Witzigmann, H. Q. Xu, L. Samuelson, K. Deppert, and M. T. Borgstrom, "InP nanowire array solar cells achieving 13.8% efficiency by exceeding the ray optics limit," *Science*, vol. 339, no. 6123, pp. 1057–1060, 2013.

[154] A. L. Greer, Y. Cheng, and E. Ma, "Shear bands in metallic glasses," *Mater. Sci. Eng. R-Rep.*, vol. 74, no. 4, pp. 71–132, 2013.

[155] M. L. Falk and J. S. Langer, "Deformation and failure of amorphous, solidlike materials," *Annu. Rev. Condens. Matter Phys.*, vol. 2, no. 1, pp. 353–373, 2011.

[156] H. M. Jaeger, S. R. Nagel, and R. P. Behringer, "Granular solids, liquids, and gases," *Rev. Mod. Phys.*, vol. 68, pp. 1259–1273, 1996.

[157] P. de Gennes, "Granular matter: a tentative view," *Rev. Mod. Phys.*, vol. 71, no. 2, pp. S374–S382, 1999.

[158] I. K. Ono, C. S. O'Hern, D. J. Durian, S. A. Langer, A. J. Liu, and S. R. Nagel, "Effective temperatures of a driven system near jamming," *Phys. Rev. Lett.*, vol. 89, p. 095703, 2002.

[159] C.-C. Wang, Y.-W. Mao, Z.-W. Shan, M. Dao, J. Li, J. Sun, E. Ma, and S. Suresh, "Real-time, high-resolution study of nanocrystallization and fatigue cracking in a cyclically strained metallic glass," *Proc. Natl. Acad. Sci. U.S.A.*, vol. 110, no. 49, pp. 19725–19730, 2013.

[160] C. S. O'Hern, L. E. Silbert, A. J. Liu, and S. R. Nagel, "Jamming at zero temperature and zero applied stress: The epitome of disorder," *Phys. Rev. E*, vol. 68, p. 011306, 2003.

[161] K. L. Johnson, *Contact Mechanics.* Cambridge University Press, 1985.

[162] L. E. Silbert, D. Ertaş, G. S. Grest, T. C. Halsey, D. Levine, and S. J. Plimpton, "Granular flow down an inclined plane: Bagnold scaling and rheology," *Phys. Rev. E*, vol. 64, p. 051302, 2001.

[163] P. A. Cundall and O. D. L. Strack, "A discrete numerical model for granular assemblies," *Geotechnique*, vol. 29, no. 1, pp. 47–65, 1979.

[164] L. E. Silbert, G. S. Grest, and J. W. Landry, "Statistics of the contact network in frictional and frictionless granular packings," *Phys. Rev. E*, vol. 66, p. 061303, 2002.

[165] J. W. Landry, G. S. Grest, L. E. Silbert, and S. J. Plimpton, "Confined granular packings: Structure, stress, and forces," *Phys. Rev. E*, vol. 67, p. 041303, 2003.

[166] R. Brewster, G. S. Grest, J. W. Landry, and A. J. Levine, "Plug flow and the breakdown of bagnold scaling in cohesive granular flows," *Phys. Rev. E*, vol. 72, p. 061301, 2005.

[167] H. P. Zhang and H. A. Makse, "Jamming transition in emulsions and granular materials," *Phys. Rev. E*, vol. 72, p. 011301, 2005.

[168] C. H. Rycroft, G. S. Grest, J. W. Landry, and M. Z. Bazant, "Analysis of granular flow in a pebble-bed nuclear reactor," *Phys. Rev. E*, vol. 74, p. 021306, 2006.

[169] C. H. Rycroft, M. Z. Bazant, G. S. Grest, and J. W. Landry, "Dynamics of random packings in granular flow," *Phys. Rev. E*, vol. 73, p. 051306, 2006.

[170] K. Kamrin, C. H. Rycroft, and M. Z. Bazant, "The stochastic flow rule: a multiscale model for granular plasticity," *Model. Simul. Mater. Sci. Eng.*, vol. 15, no. 4, p. S449, 2007.

[171] C. H. Rycroft, A. V. Orpe, and A. Kudrolli, "Physical test of a particle simulation model in a sheared granular system," *Phys. Rev. E*, vol. 80, p. 031305, 2009.

[172] C. H. Rycroft, K. Kamrin, and M. Z. Bazant, "Assessing continuum postulates in simulations of granular flow," *J. Mech. Phys. Solids*, vol. 57, no. 5, pp. 828–839, 2009.

[173] P. M. Chaikin and T. C. Lubensky, *Principles of Condensed Matter Physics.* Cambridge University Press, 2000.

[174] A. S. Argon and H. Y. Kuo, "Plastic flow in a disordered bubble raft (an analog of a metallic glass)," *Mat. Sci. Eng.*, vol. 39, no. 1, pp. 101–109, 1979.

[175] A. S. Argon, "Plastic deformation in metallic glasses," *Acta Metall.*, vol. 27, no. 1, pp. 47–58, 1979.

[176] P. Zhao, J. Li, and Y. Wang, "Heterogeneously randomized STZ model of metallic glasses: Softening and extreme value statistics during deformation," *Int. J. Plasticity*, vol. 40, pp. 1–22, 2013.

[177] P. Zhao, J. Li, and Y. Wang, "Extended defects, ideal strength and actual strengths of finite-sized metallic glasses," *Acta Mater.*, vol. 73, pp. 149–166, 2014.

[178] C.-C. Wang, J. Ding, Y.-Q. Cheng, J.-C. Wan, L. Tian, J. Sun, Z.-W. Shan, J. Li, and E. Ma, "Sample size matters for $Al_{88}Fe_7Gd_{55}$ metallic glass: Smaller is stronger," *Acta Mater.*, vol. 60, no. 13, pp. 5370–5379, 2012.

[179] D. Jang and J. R. Greer, "Transition from a strong-yet-brittle to a stronger-and-ductile state by size reduction of metallic glasses," *Nature Mater.*, vol. 9, no. 3, pp. 215–219, 2010.

[180] E. Aharonov and D. Sparks, "Shear profiles and localization in simulations of granular materials," *Phys. Rev. E*, vol. 65, p. 051302, 2002.

[181] M. R. Kuhn, "Structured deformation in granular materials," *Mech. Mater.*, vol. 31, no. 6, pp. 407–429, 1999.

[182] M. R. Kuhn, "Heterogeneity and patterning in the quasi-static behavior of granular materials," *Granul. Matter*, vol. 4, no. 4, pp. 155–166, 2003.

[183] C. E. Maloney and A. Lemaître, "Amorphous systems in athermal, quasistatic shear," *Phys. Rev. E*, vol. 74, p. 016118, 2006.

[184] A. Tanguy, F. Leonforte, and J.-L. Barrat, "Plastic response of a 2D Lennard-Jones amorphous solid: Detailed analysis of the local rearrangements at very slow strain rate," *Eur. Phys. J. E*, vol. 20, no. 3, pp. 355–364, 2006.

[185] A. Lemaître and C. Caroli, "Plastic response of a two-dimensional amorphous solid to quasistatic shear: Transverse particle diffusion and phenomenology of dissipative events," *Phys. Rev. E*, vol. 76, p. 036104, 2007.

[186] C. E. Maloney and M. O. Robbins, "Evolution of displacements and strains in sheared amorphous solids," *J. Phys.: Condens. Matter*, vol. 20, no. 24, p. 244128, 2008.

[187] A. Lemaître and C. Caroli, "Rate-dependent avalanche size in athermally sheared amorphous solids," *Phys. Rev. Lett.*, vol. 103, p. 065501, 2009.

[188] K. Martens, L. Bocquet, and J.-L. Barrat, "Connecting diffusion and dynamical heterogeneities in actively deformed amorphous systems," *Phys. Rev. Lett.*, vol. 106, p. 156001, 2011.

[189] S. Curtarolo, G. L. W. Hart, M. B. Nardelli, N. Mingo, S. Sanvito, and O. Levy, "The high-throughput highway to computational materials design," *Nature Mater.*, vol. 12, no. 3, pp. 191–201, 2013.